The Interaction of Nanoparticles with Biomimetic Bilayers using Molecular Dynamics Simulations

Sang Young Noh

MOAC Doctoral Training Centre and the Department of Chemistry
University of Warwick

This dissertation is submitted for the degree of
Doctor of Philosophy

September 2018

DECLARATION

I hereby declare that except where specific reference is made to the work of others, the contents of this dissertation are original and have not been submitted in whole or in part for consideration for any other degree or qualification in this, or any other university. This dissertation is my own work and contains nothing which is the outcome of work done in collaboration with others, except as specified in the text and Acknowledgements.

Sang Young Noh

September 2018

ACKNOWLEDGEMENTS

I would first like to thank Dr Rebecca Notman and Professor Alison Rodger for helping me through some of the most troubling times of my life so far. The process of writing this thesis has been a turbulent one to say the least, and any help to get me through in those situations are always appreciated. I would also like to thank my parents, who I have always been appreciative of, and have helped me overcome very difficult times, and I think I always underestimate the effort they put in to make sure I am okay, which is a something I should be working on actively.

In the memory of P. M. Rodger.

ABSTRACT

The self-assembly of nanoparticles (NPs) and amphiphilic macromolecules offers a powerful route to generate functional soft materials with controllable structure and properties. Furthermore, synthetic model membranes can serve as a platform to investigate the passage of NPs across biological membranes (e.g. lung, skin and cell membranes) which will help to address issues of nanotoxicology and assist in the design of functionalised NPs for use in the diagnosis and treatment of disease. The problem is that the relationship between the physiochemical properties of NPs and their interaction with and transport across membranes remains poorly understood. To address this challenge we have investigated the mechanisms by which NPs of varying size and hydrophobicity interact with and cross biomimetic polymer membranes. We have developed a model NP-bilayer system which comprised a coarse-grained poly(ethylene)6-block-poly(ethylene oxide)2 ($C_{12}E_2$) bilayer in water and a generic NP of 1.0, 1.5 or 2.0 nm radii with hydrophilic, hydrophobic or intermediate character (nine different systems in total). In additon, we have carried out free energy studies on each of these trajectories and simulated two-component bilayers with hydrophobic nanoparticles. We show that the hydrophobic nanoparticle can induce a local ordering of amphiphilic structures, and show that it can act as a lineactant between the interfaces of the phase-separated domains. Throughout the study of the surfactant system, we have compared the two free energy methods - the *Umbrella Sampling* (US) method and *Steered Molecular Dynamics* (SMD) method with NP/bilayer systems, and compare their accuracy and efficiency.

TABLE OF CONTENTS

LIST OF FIGURES

List of Tables

CHAPTER 1

INTRODUCTION

1.1 Statement of Purpose

The mechanism of translocation of nanoscale objects has gathered considerable interest due to its potential as a targeted drug-delivery mechanism. Depending on the surface properties of the objects, the lifetime of the nanoparticle within surfactant and lipid membranes has been speculated to change, depending on the interaction with the attractive and repulsive parts of the surfactant/lipid. While there has been a great advancement in the understanding of these mechanisms, complicating factors remain - for example, the interaction of such objects with aggregates within the bilayer - such as domains and membrane proteins, remain challenging to study - due to the difficulty in observing the correct *in vivo* conditions in an experimental environment.

To alleviate this problem, the use of computer simulations have been increasingly utilised to gain valuable insight into the interaction of nanoscale objects in such biophysical systems. With a rigourously tested mathematical framework to work with, computer simulation methods have provided a greater insight into the translocation mechanisms through a bilayer, and the interaction between the heterogeneous components within a bilayer. The

study illustrated here investigates three main components of a bilayer system with nanoscale objects - the interaction profile through the bilayer normal, the interaction profile across the bilayer lateral with domain-like aggregates, and the methodologies for extracting the energetic profiles across the bilayer.

This Chapter represents the background to the study - we first discuss the properties of the surfactant/lipid bilayer. This is followed by an overview of molecular models available that have been utilised for molecular simulation. This is then continued by the analysis of the effect of various physiochemical surfaces on the interaction between nanoscale objects with bilayers. Then, we look at the current limitations that are associated with the interactions with extraneous factors within the homeostatic environment. Finally, the aims and objectives of this work is stated.

1.2 Background

1.2.1 Soft Matter

The study of physics at the nanoscale has been a topic of intense interest due to the staggering array of structural variety which can form, which vary in their shape, rigidity, and surface features. The inherent complexity of these nanoscale systems, stemming from the web of interactions involved in the manufacture and maintenance of structures such as micelles, vesicles, proteins and polymeric bilayers allow the wide range of phenomena seen in these *soft* structures. However, it is this very complexity that also constrains how to effectively analyse the root causes of the biophysical phenomena observed. Whilst it is difficult to simplistically define such systems under a single denomination, commonalities can be observed. The majority of the molecular interactions we encounter in such biophysical systems involve intermolecular and intramolecular forces - the former coming into prominence

in the aggregation of monomers, and the latter coming into effect when we encounter the change in the internal conformation of the molecule. Here, as the energetic extremes required for the formation and fracture of covalent and ionic bonds are not significant, the forces that dominate the systems involve long-range forces, geometric forces and interfacial forces between large collections of molecules - i.e. as a whole, the system is dominated by *soft* interactions - hence, in scientific literature, research in this field has been noted as works of *soft matter* (SM).

In practical terms, SM is defined by intermolecular interactions which are mediated by moderate strength (of order of kT, where k is the *Boltzmann* constant and T refers to the *temperature*, usually 298 K to depict room temperature), often bounded by the room temperature. We can identify key features that unify the vast range of structures and phenomena observed. These forces range from long-range forces such as coulombic and short range *Van Der Waals* (VdW) forces, which derives from the electron density and distribution within the functional groups of molecular aggregates. Complex entropic contributions from the hydrophobic and hydrophilic effects, as well as the hydrogen-bonding that is present in aqueous environments. Table 1.1 shows the functional form of common types of interactions. The combination of these forces results in the complex architecture in biology we seek to explore. Forces arising from dipoles, ion-dipole interactions, steric interactions also contribute significantly to the resulting structure.

1.2.2 Amphiphilic Bilayers

As the key building block of biological and biomimetic structures, an extensive effort has gone into identifying the key properties of lipid-type molecules. The key feature of an amphiphile concerns the presence of a hydrophilic ‘head’ and hydrophobic ‘tail’, which have equally important yet opposite characteristics. A purely hydrophobic compound, such as

Interaction type	Functional form
Coulombic	$\frac{Q_1 Q_2}{4\pi\varepsilon_0 r}$
Charge-dipole (fixed dipole)	$\frac{-Qu\cos\theta}{4\pi\varepsilon_0 r^2}$
Charge-dipole (free dipole)	$\frac{-Q^2u^2}{6(4\pi\varepsilon_0{}^2 kTr^4)}$
Dipole-dipole (fixed dipoles)	$\frac{-u_1u_2[2\cos\theta_1\cos\theta_2-\sin\theta_1\sin\theta_2\cos\eta]}{4\pi\varepsilon_0 r^3}$
Charge-nonpolar	$\frac{Q^2\alpha}{2(4\pi\varepsilon_0)^2 r^4}$
Nonpolar-nonpolar	$-\frac{3}{4}\frac{h\nu\alpha^2}{(4\pi\varepsilon)^2 r^6}$

Table 1.1 Common types of Interaction and their functional forms - here, the large variety of intermolecular potentials arise from the geometric factors and electron densities around the functional groups, rather than being being fundamental forces themselves. The comprehensive list is illustrated by Israelachvili [1].

long-chained hydrocarbon species, when in a mixture with water, can completely *phase-separate* to form layers of immiscible liquids, due to the attraction between hydrophobic species, and its repulsion to hydrophilic species. The molecular components of consideration that form such lipids/surfactants are those with both hydrophilic and hydrophobic components. Here, the hydrophilic component provides a favourable interaction site against the surrounding charged/aqueous environment, while the hydrophobic components aggregate *away* from the aqueous layer - with the addition of the hydrophilic headgroup, the overall hydrophobicity of each molecule is reduced, which reduces the unfavourable energetic cost of the species in contact with an aqueous environment. This is the key attribute that distinguishes amphiphilic species. This ability to aggregate at a finite N cluster of molecules is the primary character that distinguishes the amphiphilic molecule compared to a purely hydrophobic alkane chain. Figure 1.1 shows a small sample of the type of lipids commonly encountered.

In each lipid/surfactant example used in this work, the CH_3-[CH_2-CH_2]$_N$-X derivative lipid species can be freely changed with a variety of charged headgroups, saturated/unsaturated tailgroups, and can contain branched species as components which can affect the overall

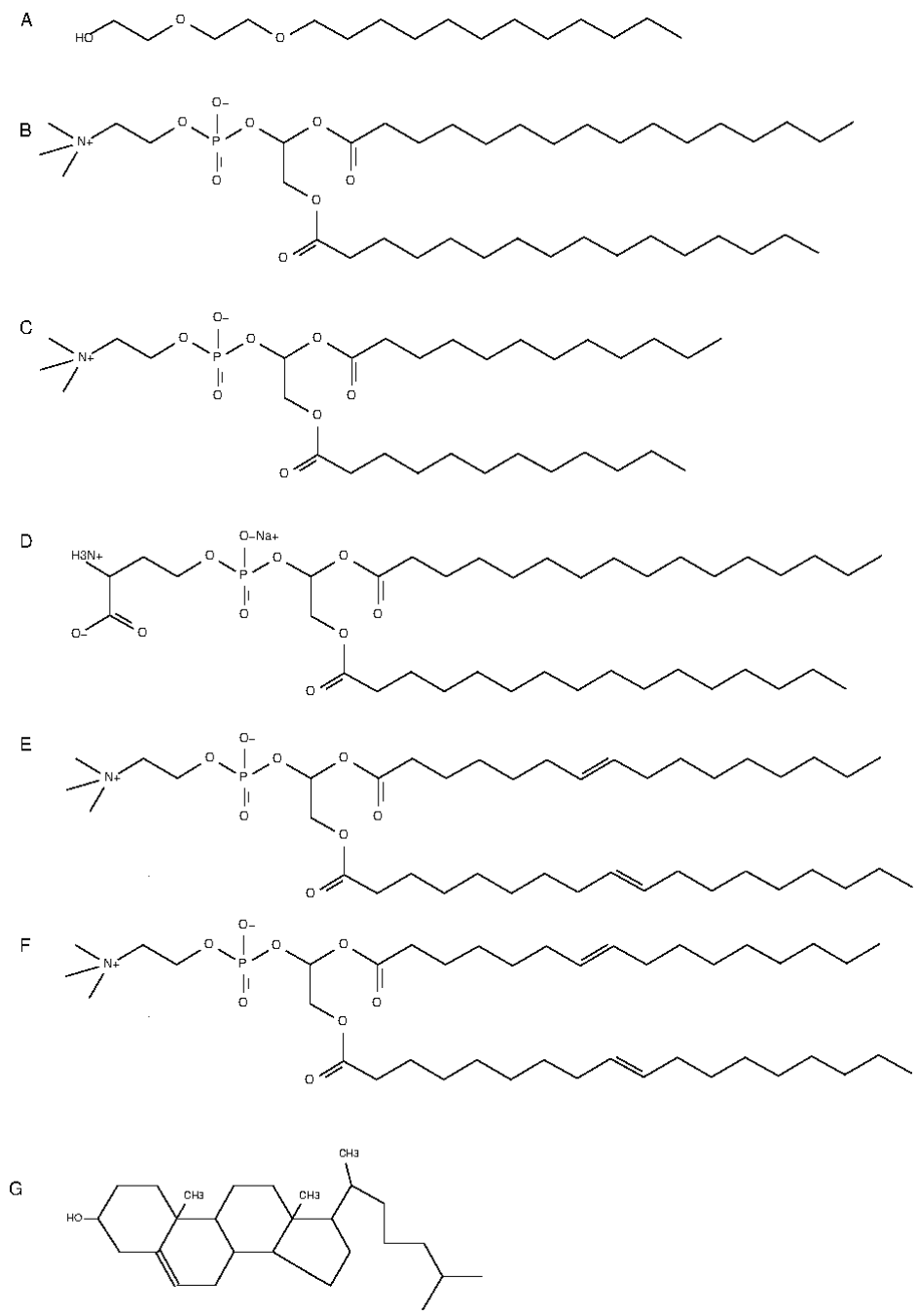

Fig. 1.1 A showcase of the diversity of lipids/surfactants. A shows a fatty acyl polyethylene glycol (PEG-PEO) type surfactants, while B shows an saturated phosphocholine (PC)-based lipid (1,2,dipalmitoyl-sn-glycero-3-phosphocholine, or DPPC), C shows the shorter PC based lipid (1,2-dilauroyl-sn-glycero-3-phosphocholine, or DLPC) with increased charge density in the headgroups, E shows the unsaturated type of lipids (1,2-dioleoyl-sn-glycero-3-phosphocholine, or DOPC). F shows the sterol (cholesterol) lipid types, which are characteristically shorter and more rigid.

fluidity and bulk hydrophobicity. For example, poly(ethylene)-block-poly(ethylene oxide) ($C_{12}E_2$) [2] which are electostatically neutral, can self-assemble to form micelles and membrane like vesicles. In nature, glycerolphospholipid based models have been identified as the basic template of such lipids, where modifications to its headgroup and tailgroup saturations can vary its hydrophobicity, shape and rigidity. Figure 1.1 shows a small subset of the multitude of structures such PC-based lipids can form. In general, the bilayer structure provides a stable controlled environment for complex functional macromolecules to assemble and function without being subjected to change in function due to fluctuations in temperature, concentration and pressure. What *distinguishes* the bilayer we observe in cellular environments compared to manufactured polymeric vesicles and their equivalents is the enormous variety of the species involved. A 3 or 4 component structure of PC-type lipids and its variations is highly common, with variations depending on the organelle. The cataloguing of the individual components and their specific effects in an organelle is a critical part of research of drug delivery mechanism pathways, nanotoxicity and related pharmaceutical research. The idea of modifying a large polymeric aggregation such as polymersomes, artificial vesicles used for encapsulating drugs, proteins and enzymes, has been explored in recent years, as a novel avenue of materials research. Since the advent of methodologies developed by Wainwright and Metropolis [3, 4] the potential for accurately simulating many-body systems has been considered the high goal of computer-driven simulations, and their methodologies have grown into two distinct branches of emulating the physics of many-body systems, known as *Monte-Carlo* (MC) and *molecular dynamics* (MD) techniques. The former relies on moving each molecular component based upon the most *likely* move based upon the Boltzmann factor, while the latter method relies upon an iterative time-evolution of Newton's equations of motion. With the advent of computational power becoming widely avaliable, and following the pattern of Moore's law [5] and parallel methodologies [6] to speed up the calculation of molecular interactions, the use of *molec-*

ular simulation techniques has become increasingly prevalent both as an auxiliary analysis method to further interpret the evidence presented with experimental methods, as well as a standalone methodology. In the past, the prohibitive convergence timescales of large, complex biophysical systems hindered it's use as a practical method to study scientific phenomena. While the scale of a fully described biomolecular system is still out of reach (due to the astronomical number of interactions that needs to be computed). It has now become possible to reach timescales where we can gain practical information that provide new insights.

As of today, an extensive range of surfactants, lipids, and protein components have been parameterised for *molecular mechanics* (MM), where the bond potential, angular potential, intermolecular and intramolecular potentials are given a highly detailed expression. Since the success of the CHARMM development project by Karplus *et al* [7–9] describing the diverse range of atomic structures involved in soft systems, numerous variations and alternative models have been developed. The main constraining factor of simulating complex biophysical systems has been the limitations in interpreting very large systems, which require very high computing technologies to simulate on timescales that are equivalent to biological phenomena. For example, a typical eukaryotic cell can have a number of atoms on the order of 10^{14} atoms [10], and the largest system in complete MM interpretation may reach scales of approximately 10^7 interacting atoms at lengths of 1 μs. This is clearly not on the timescales of when biomechanical processes occur. To compensate for this, methods for simplification of the molecular model has been sought. In general, the simplification to CG models allow a number of advantages when running molecular simulations. The methods involve simplifying the superfluous elements in an *all-atomic* (AA) simulation. In general, there are 4 main objectives to the CG-method - a reduced number of degrees of freedom (DOFs), reduced detail of the long-ranged interactions, faster dynamics and allowing for

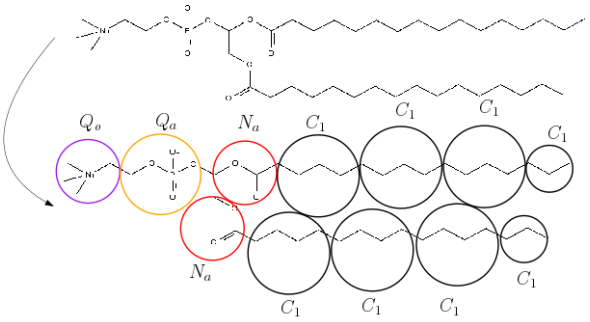

Fig. 1.2 The coarse-grain (CG) mapping of the DPPC lipid molecule, as mapped by the MARTINI-FF [15]. In general, MARTINI follows a four-to-one mapping of AA molecules to CG beads. In addition, the FF comes with utilities which allow the building of large vesicles and bilayers.

larger simulation time steps for the system. The schematic for such simplification is shown in Figure 1.2. By the CG procedure, multiple chain components can be approximate to a single bead, therefore speeding up the calculation of the equations of motion and convergence of physical properties. By adjusting the level of coarse-graining, a multitude of coarse-grained force fields (CG-FFs) have been computed and specialised for generalised and specialised systems. For example, the list of CG-FFs includes SDK, ELBA, MARTINI, Voth, AWSEM, CABS, OPEP, PRIMO, Rosetta, Scorpion and UNRES [11–22].

The primary objective with molecular simulations is to reproduce the experimental phenomena, and hence, elucidate the root phenomena behind the experimental result. Clearly, the key problem of every complex simulation is this - *How do we capture the accurate physics of a specific process of interest, within a reasonable timescale?*. Even with the computational resources available at present, it can be difficult to reach a timescale for a reaction of interest to be observed, and then one must account for the limitation of only having a brief snapshot in time of a system. Seemingly straightforward processes such as protein conformational changes and protein-ligand interactions can only be observed through forcing the system to bias towards an environment where these changes can occur in the allocated time. Collectively, the change of state in these processes follow a pathway which are conveniently

referred to as *reaction coordinates* (RC) and shall generally be referred to as such from this point on. Many independent research groups have tried [23–26] to develop the collection of methods known as *biased-sampling methods*, which collectively have attempted to try to sample these *high-energy* states that constitute the RC of interest. A number of options are available for measuring the free energy change of a complex RC.

A multitude of sampling methods to measure the free energy has been implemented and tested through the development of simulation techniques. Metadynamics [27], for example, follows the approach of adding unfavourable Gaussian potentials to previously mapped phase space, to ensure that the process maps new parts of the RC, from which the free energy landscape can be recovered from the sum of the Gaussian distributions. The most common method for calculating the free energy change, due to its relative simplicity of implementation, and intuitive familiarity, is the *umbrella sampling* (US) method. [24, 25, 28] This involves dividing the reaction coordinate into discrete bins, and a biasing potential (usually in the form of a Hooke's Law potential to restrain it onto a reaction coordinate of interest) is implemented to sample the rare-event trajectory incrementally. These new sampling bins are recombined and unbiased to produce the final free energy profile. This method has proven highly effective at producing the free energy profiles of many complex processes, such as ligand-docking simulations, protein conformational change and bilayer translocations of molecules [29]. An alternative methodology for mapping the free energy change through the reaction coordinate is using the *steered molecular dynamics* (SMD) method [30]. Here, the SMD method work by defining the RC and the component/molecule in question to be moved along it, and implementing a harmonic potential on it much in the same way as the US method. However, in contrast to the US method, the harmonic potential is steadily moved along from the starting point to the end point of the RC at a constant velocity. The force-time relation over this RC is computed and used to calculate the work

distribution along the RC. Using this method, one can map the reaction coordinate in quick succession, compared to the US method. To extract the free energy from the work distribution, Jarzynski [31] proposed a relation that equates the work (a path integral function that is *directionally dependent*) with the free energy change, where the exponential of work can be related to the exponential of the free energy. Due to the non-equilibrium nature of this equality, this suggests that the free energy can be calculated from the average of multiple fast-running simulations, which would obviously be a gain in efficiency compared to the discrete binning approach of the US method. This method, for example, has been highly effective at analysing the protein-ligand interactions [32–34], and the extraction of lipids from membranes [35, 36].

1.2.3 The Effect of Heterogeneous Components in Bilayers

One of the most intriguing phenomena seen with heterogeneous components in amphiphilic bilayers has been the formation of small aggregates through the demixing of components. The mechanism of such 'cross-linking' (the linking of particles either by well-defined ionic and covalent or long-range forces) can vary; Christian *et al* [37] managed to create spotted vesicles by inserting cationic ions in to synthetic polyanionic amphiphiles - the ions were observed to nucleate oppositely charged domains and induce phase separation on the vesicle surface. Analogous domain formations can be seen in biomembranes - kinks in the tailgroup structure (due to a higher proportion of unsaturated bonds) in the lipids induce the formation of lipid-ordered/lipid-disordered ($l_o l_d$) domains. The schematic of such a structure is shown in Figure 1.3. Numerous reviews and studies have debated the existence of such rafts within the membrane [38–42]. From this idea, the *lipid raft hypothesis* was introduced, and multiple experimentations have shown greater evidence for the existence of these structures. These rafts are thought to form a crucial part of how lipid proteins structure themselves around the cell membrane; the formation of such rafts is likely to control the flu-

idity of the membrane in the location of membrane-proteins, many of which are involved in key processes such as signal transduction which controls the mechanism behind cell stimuli; Helms *et al* [43] for example, suggested that an enlarged protein-protein interaction forms a coagulation of large lipid shells around a group of protein structures embedded within the membrane, which ultimately forms the lipid rafts. Another hypothesis suggested that within yeast cells, the rafts are the base for glycosylphosphatidylinositol(GPI)-anchored proteins from where protein sorting can occur in the endoplasmic reticulum. A molecular species that has been hypothesised to act as a controlling agent for domain maintenance is the cholesterol molecule (CHOL) [44–47]. Figure 1.3 shows an example of how rafts may support membrane protein structures. Within mixed DPPC/DUPC/CHOL bilayers, changing the concentration of cholesterol and sphingolipid (SPH) in lipid membranes have shown has a significant effect on formation of lipid rafts, where the rigid structure of CHOL stabilizes the saturated regions in the DPPC group, forming the lipid-ordered (l_o) regions of the bilayer around a large disordered l_o region. Recent experiments with complementary simulations have further supported the formation of these rafts; Nickels *et al* [48] carried out neutron scattering/neutron scattering length density experiments in unilamellar vesicles (UV) to determine the distinguishing factor of a lipid within raft-like structures and those in the 'sea' surrounding it - the study showed a distinctive bending moduli within the raft phase. This phenomena was reproduced by MD simulations of identical compositions, which suggested that the raft formation is controlled by the tilt, splay and intermediate 'line-active' lipids such as 1-palmitoyl-2-oleoyl-sn-glycero-3-phosphocholine (POPC) which acts to stabilize the high boundary energy costs in the raft/phase interface. This suggests that the formation of rafts may be a multipartite combination of effects from intermolecular forces between the heterogeneous lipid components, the effect of saturation by sterol and sphingolipid type molecules to support the lipid order, and the dual effects of protein and line-active lipids to regulate the size and rigidity of the raft.

Whatever the case, it is beyond doubt that the membrane proteins act as gatekeepers and channels on the boundaries of organelles which can control the flow of water/ions and maintain a favourable concentration gradient [49]. For example, receptor proteins such as G-proteins [50] help to regulate signals, whilst proteins such as P-glycoprotein [51, 52] has been specifically designed to indiscriminately keep material out of the membrane. Experimental work by McMahon *at al* [49] have shown that scaffolding proteins on the membrane surface partake in an active process of membrane curving, which is an essential process in organelle formation, division and general growth. Hence, if the function of these protein structures are dependent on the raft structures that support it, how the chemistry of the raft relates to the function of the protein embedded/associated with it may be essential.

While the structural effects of sterol-type heterogeneity can be drastic, it is also important to consider the change in lipid chemistry that the embedding of such structures can show. For example, CHOL can modify the liquid-gel phase of the lipid bilayer to form a multitude of structures - In simulations of sphingomyelin/dioleylphosphatidylcholine (SP/DOPC) mixed bilayers [53–56], it acts as an intermediate, fixing itself in-between the SP/DOPC layers. Simulations of dimyristoylphosphatidylcholine (DMPC)/CHOL have shown that a higher concentration of CHOL show a decrease in the permeability of ions in the bilayer [57]. The significance of composition becomes apparent when the cholesterol/phospholipid composition of cellular organelles are analysed - each organelle shown to have significantly different CHOL compositions, which further supports the hypothesis of embedded molecules acting to control the dynamic nature of lipid/amphiphilic bilayers [58]. Subtle effects are also involved with changes in headgroup structure; simulations with mixtures of DOPC/DPPE bilayers [59] have shown that with increasing PC concentration, the PC groups reduced the overall area of the bilayer and show increased hydration around the

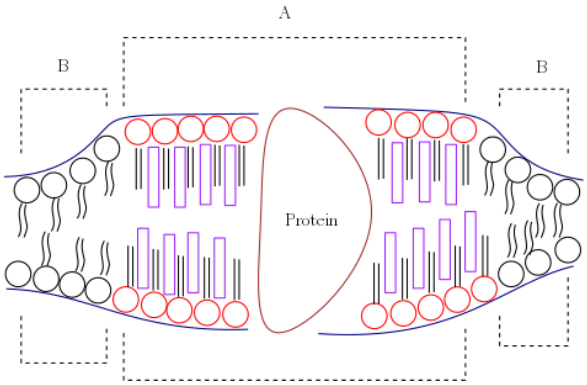

Fig. 1.3 Illustration of how a inhomogeneous bilayer may support lipid-support protein models inside the bilayer - the sterol type molecules (CHOL) supports the saturated components of the mixed bilayer, which increases the thickness and order, which form a liquid-ordered (l_o) component, while the surrounding component is composed of unsaturated lipids making up the liquid disordered (l_d) component

PC groups compared to a pure DPPC bilayer. Similarly, simulations of 1,2-distearoyl-sn-glycero-3-phosphocholine/1,2-dilauroyl-sn-glycero-3-phosphocholine (DSPC/DLPC) [60] systems show phase changes, where the liquid phase show patches of gel phase corresponding to the phase separation of the DLPC groups.

1.3 The Interaction of Biomimetic Membranes and Nanoscale Objects

Given the importance of phase change relating to the interactions of surfactants and external species, a systematic study into the effects of physiochemical properties, anisotropy and size with respect to the interaction of nanoscale objects with surfactant/lipids has come into focus. As a group, these nanoscale structures can be summarised as *nanoparticles* (NPs), and shall be referred to as such for the rest of this introduction for the sake of brevity. The variety of NPs may range from metallic, oxide, and quantum dot types to rigid polymer

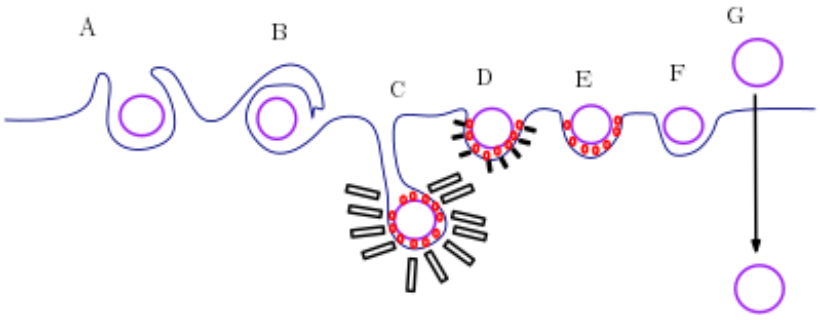

Fig. 1.4 The range of pathways available for NPs to enter the cellular cytoplasm. A and B show ATP (energy) driven endocytosis processes known as phagocytosis and macropinocytosis, whilst C, D and E show receptor-mediated internalization processes - Caveolin-dependent, Clathrin-dependent, and receptor-mediated processes respectively. F and G show a generic non-specific internalisation with the bilayer and direct translocation respectively.

aggregates, which may range from sizes of 1-1000 nm, and pathogenic vectors such as bacteria and viruses, which range in the 1000s of nm (in the case of bacteria) and 100's of nm (in the case of viruses) [61]. For example, carbon NPs (CNPs) can originate from diesel based soot in urban environments, and fine particulate matter in natural soot as well. A CNP of particular note is the fullerene structure, which consists of a hollow spherical allotrope. Its unique electronic and chemical properties have resulted in its widescale use in industry, including its potential as a source of nanotoxicity or a novel drug delivery mechanism -For example, clinical studies studying the effects of CNPs showed aggregation inside the lipid bilayer. Simulations with carbon NPs [62, 63] have shown that hydrophobic NPs can permeate through the membrane, and experiments have shown that accumulated NPs inside lipid membranes can increase nanotoxicity and subsequently cause cell death [64].

In addition to the direct effect of the NP geometry on the bilayer structure, its effect on the overall chemistry in a biosphere has also been an area of interest. For example, the enhanced production of *free radicals* (molecular species that are highly reactive due to a unpaired electron) has been observed in the presence of CNPs. Cellular components have natural defence mechanisms for combating excessive reactive oxidative species (ROS) (oxy-

gen based free radical components) such as superoxide dimutase in the mitochondria. As CNPs have been demonstrated to aggregate within the cellular environment, this provides a large surface area to mass ratio for the ROS to develop, which can result in an excess of ROS overcoming the natural defences of the cell. NPs of differing structures such as carbon nanotubes (CNTs) can increase this effect by increasing the rate of penetration through the bilayer membrane; the variance in diameters of CNTs have shown that smaller CNTs penetrate the membrane through simple diffusion mechanisms and larger ones go through endocytosis like mechanisms. This effect has been shown to be a reiterated phenonema with NPs of many different physiochemical properties; Iron oxide NPs (FeO-NPs), for example, has been shown to catalyse the production of hydroxyl radical groups [65] through inducing homogeneous and heterogeneous fusion processes on its surface. In another example, silver (Ag) hydrophobic NPs [66] have been shown to aggregate *en masse* and subsequently induce a local liquid phase. The effects of Ag-NPs can be numerous - studies have shown that the concentration of AgNPs are correlated with disruption in the cellular membrane, and the generation of oxidative stress due to generation of ROS [67], as with the CNP example. For instance, the interaction of 20-100 nm Ag-NPs demonstrated both placement inside the bilayer interior on the small scale whilst the larger NPs did not enter the bilayer at all. In both cases, however, the presence of ROS was detected which affected the function of mitochondria in the bilayer interior [68].

On the other hand, the effects of NPs may also be environmentally beneficial; studies have also assessed that the *cross-interaction* between copper oxide (CuO) NPs and CNTs can hinder the toxic effects of the CuO NPs on microbial denitrification [69] - an essential environmental process for fixing nitrogen into the environment. The evidence suggested that while CNT on its own does not affect the denitrification - the CuO-CNT interaction limits the NADH hindrance by the CuO NP, through the hindrance of the CuO uptake by the bac-

terial cellular membranes.

1.3.1 Modifications of NPs and its Effect on the NP-Bilayer Interactions

From the numerous clinical and environmental studies, it is clear that NPs of a wide range of physiochemical properties can damage and disrupt the cellular mechanisms at a molecular level. Hence, it is important to realise which geometric factors of the NP can affect the ease of entry through an amphiphilic bilayer. By changing the surface area to mass ratios, the free energy of transition into the bilayer can be modified - through such an approach, extensive efforts have been made to quantitatively catalogue the nanotoxicity and the interaction types with amphiphilic bilayers. Figure 1.4 shows the array of possible translocation mechanisms across the bilayer membrane. In general, larger micrometer sized particles may require energy-induced processes such as phagocytosis-type endocytosis [70, 71], which through an input of energy, distorts the membrane around the NP structure. Where there are amassed collections of fluids and particles, the membrane deforms more significantly through macropinocytosis [72]. In other cases, receptor-mediated translocations such as the clathrin-mediated endocytosis has been demonstrated as most often exploited by viruses [73, 74]. As the dimensions of the NPs are entirely comparable, it is clear that the surface properties of these NPs dictate the type of translocation it undergoes. *How do NP surface properties affect the translocation pathway?* Not only would such an answer elucidate idealised pathways for applications, but also the characteristics which decide the pathway of translocation may also eludicate the mechanisms of entry by bacterial and viral vectors, some of which have been shown to enter through non-endocytosis pathways, as shown in the case of the influenza virus, demonstrated by Sieczkarski *et al* [73].

To this end, simulation techniques have been used to identify the key geometric and surface properties which affect the pathway of translocation. For example, Yang and Ma [75] used mesoscale MD-like simulations to investigate NPs of various shapes, including ellipsoids, cylinders and cones. It was discovered that ellipsoidal NPs can change their orientation to maximise the contact area between the NP and the bilayer. The asymmetry that arises when interacting with the bilayer means that asymmetric endocytosis often occurs with non-spherical NPs. With MD simulations, it has been demonstrated that the spherocylindrical NPs have a greater rate of endocytosis which is due to the contact area effect, whereas the spherical cylinder only has half the surface area needed to cover along its length, whilst deforming the bilayer on contact with the same curvature magnitude [76], which demonstrates that depending on the anisotropy of the NP, one can change the mechanistic pathway of translocation. Dynamic structures may also help to design efficient drug delivery. For example, Loverde *et al* have managed to create spherical and flexible worm-like NPs using poly(ethyleneglycol)-poly(caprolactone) amphiphiles, which show potential as an agent for delivering Taxol [77], a standardized pharmaceutical used in pancreatic cancer treatments, and accurately predicted the size ranges of worm-like NPs from simulations - this has helped to elucidate that with worm-like structures, a higher 'payload' of Taxol molecules can be managed in comparison to the spherical structure.

Given the prominence of hydrophobic/hydrophilic forces present in SM systems, precisely defining the characteristics of hydrophobicity of a NP and its effect on the biomimetic bilayer is an area of continued debate and research. How the surface hydrophobicity affects the mechanism of entry into the cytoplasm has been a field of intensive study. In the case of hydrophobic NPs, it may act as an effective drug delivery mechanism by increasing the hydrophobicity of a highly soluble pharmaceutical drug, or remain in the interior of the

bilayer, causing a buildup and accumulation of aggregates of NPs. Here, again, molecular simulation studies have helped to identify many effects. Ramhalo *et al* [78] for example, demonstrated using the MARTINI FF [15] that a spherical, rigid NP embeds itself inside the tailgroup beads of the DPPC bilayer, without disrupting the gel phase of the bilayer, while the hydrophilic examples caused significant disruption in the gel phase. In contrast, smaller hydrophobic NPs were simulated by Pogodin *et al* [79], which demonstrated that small hydrophobic NPs aggregate inside the lipid bilayer, which may maximise the steric favorability of the NP-NP interactions and the NP-tailgroup interactions. This is shown in Figure 1.5. Whilst the idea that a hydrophobic NP may favour the hydrophobic tailgroups might be straightforward, its interaction with the heterogeneous components inside a bilayer has enticed more interest. Barnoud *et al* [80] demonstrated that hydrophobic species such as hexadecane, cyclodecane and fullerene type molecules [81, 82] can drive the reshaping of lipid rafts/domains. Interestingly, the purely aliphatic species has been shown to aggregate near the lipid domain interface, whilst the aromatic equivalents catalyzed domain formation through an increase of thickness of the l_d (unsaturated) regions and by acting as a pushing force against the CHOL, which increases the rate of formation of the l_o phase.

By increasing the hydrophilicity of the NP in question, one can increase the solubility and the interaction with the hydrophilic headgroups of the bilayer. For example, Ding and Ma designed a NP with a hydrophobic and hydrophilic face (Janus-NP,or J-NP) which was inserted into a model membrane [83], which showed that the J-NP initially adsorbs onto the bilayer surface on its hydrophilic face, and gradually the hydrophobic tailgroups of the bilayer engulf the hydrophobic face of the J-NP. In addition, the effect of differing anisotropies of the NP was investigated; elliptical J-NPs showed that four different types of interactions with the bilayer can be identified, with four different absorption/adsorptions depending on the interaction-orientation of the ellipsoid. While purely theoretical in char-

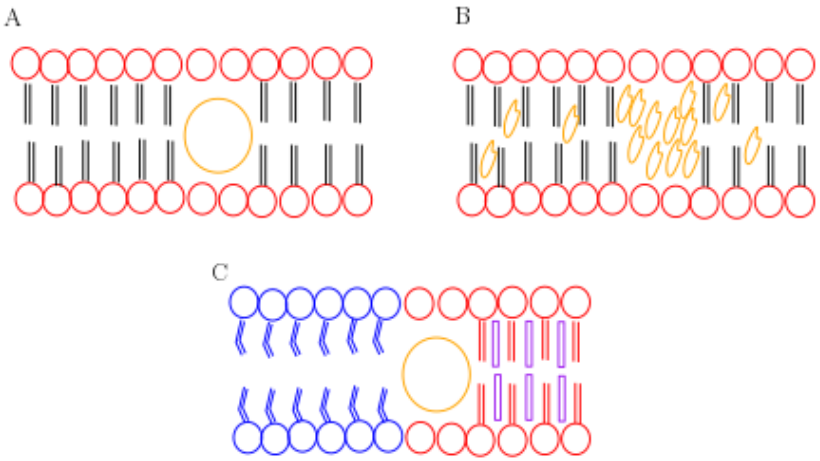

Fig. 1.5 Schematic showing the energetic well in the bilayer interior for hydrophobic NPs. A shows the preference of large rigid hydrophobic NPs inside the bilayer, while B shows the aggregation of smaller species of hydrophobic NPs. C shows the hydrophobic force acting as a line tension relaxant (i.e. reduced the energy on the raft domain interface), or in the case of aromatic compounds, as the driver of domain formation by pushing the sterol groups into the l_o region (red) [80].

acter, NPs of intermediate hydrophobicity have also have garnered much attention, in the search of a NP where its translocation mechanism can pass through the membrane without becoming trapped within the hydrophobic interior. For example, simulations which compare hydrophilic/hydrophobic NPs with DPPC bilayers were run by Gu *et al* [84]. They have suggested that semi-hydrophilic NPs prefer to be adsorbed on the bilayer surface interface between the hydrophilic headgroups and hydrophobic tailgroups. Expanded studies by Su *et al* [85] showed that while the intermediate NP distribution was indeed the highest at the headgroup/tailgroup interface, the lowering of the energetic barrier to the hydrophobic region allowed perturbations in the bilayer energetics to induce the direct translocation of the intermediate NP. As the ideal goal for NP applications is to strike the right balance between cellular uptake and cytoxicity, the implication that NPs of intermediate hydrophobicities may be able to directly penetrate through the bilayer fits this ideal, and requires further investigation.

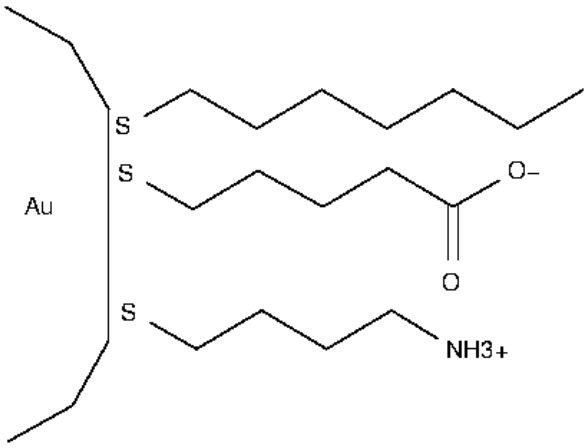

Fig. 1.6 The illustration of a LF-NP, with a coordinated alkyl chain (hydrophobic), and coordinated ammonium and carboylated chains, which are positively and negatively charged respectively (hydrophilic)

1.3.2 Functionalization of NP Surfaces

An additional catagory of NPs that has gathered intense interest are the surface-functionalized NPs, where the core rigid NP is functionalized with adsorbed ligands on the surface. Figure 1.6 shows an illustration of thiolated ligands functionalized in this manner. The combination of ligand properties and the core property allows for promising targeting mechanisms for NP-drug delivery. For example, targeted clinical treatments using iron oxide derivatives (Fe_3O_4 and Fe_2O_3) NPs with thiolated ligands can be taken advantage of by using the inherent superparamagnetic properties for hyperthermia/bimodal-therapy treatment of tumour cells [86, 87]. Another factor of interest is the controlled anisotropy of ligands on the surface; a patchy ligand surface has the advantage of inducing a specific type of mechanism with its interaction with the membrane - it is speculated that patchy surface functionalization may help to bypass the wrapping/endocytosis mechanisms [88, 89] and instead enter a membrane through direct penetration, which avoids the build-up of toxicity within the bilayer due to the hydrophobic characteristics of the NP. This shows that exploring the variations in the interactions between bilayers and NPs is an important aspect in the development of novel drug delivery methods - By direct penetration, drug delivery methods may be able to bypass

the regulatory mechanisms. The mechanisms of these types of NPs has been explored with molecular simulations techniques as well - since the demonstration by Glotzer [90] of a surface functionalized gold NPs, (LF-AuNPs), a series of simulation studies have elucidated additional details into the mechanism of translocation. Lin *et al* [91] for example, used the MARTINI force field [15] to simulate LF-AuNPs with cationic, anionic and hydrophobic ligands adsorbed on the Au surface, which demonstrated that the in DPPC/DPPE mixtures (DPPE is the charged equivalent of the DPPC, where the trimethylamine is replaced with a ammonium ion group, better exposing the charged groups), positively charged ligands coordinate with the negatively charged headgroups of the heterogeneous bilayer. The density of the positively charged ligands was speculated to control whether the LF-AuNP required a receptor-ligand coordination entry, or in the case of a very high density of positive ligands, bypass the endocylic mechanisms entirely. With the case of hydrophobic ligands, it was thought until recently that the hydrophobic ligands were positioned near the center of the bilayer, much in the same manner as a rigid hydrophobic NP. Recently however, Guo *et al* [92] demonstrated through optical fluorescence microscopy that this was dependent on the size of the NP - when the size of the NP allowed a sufficient curving of the bilayer, which allowed the hydrophobic ligands to pull lipid molecules away from the bilayer, effectively allowing a lipid exchange. Hence, this demonstrated that the reorganisation of the local lipid molecules by the functionalized NPs plays a major role in its translocation mechanism and coordinating/disruptive effects while inside the bilayer interior. Further simulations by Gkeka and Van Lehn [93, 94] demonstrated through MD simulations that with charge-active functionalized ligands, the NP may undergo a 'snorkelling' effect, where the surface ligands reorganize its orientation to the bilayer normal, where it maximises the contact between the hydrophilic and hydrophobic groups of the lipids and the ligands. This provides a mechanistic alternative for charged species to overcome the hydrophobic barriers that would normally prevent its movement near the tailgroup regions of the lipids. Despite

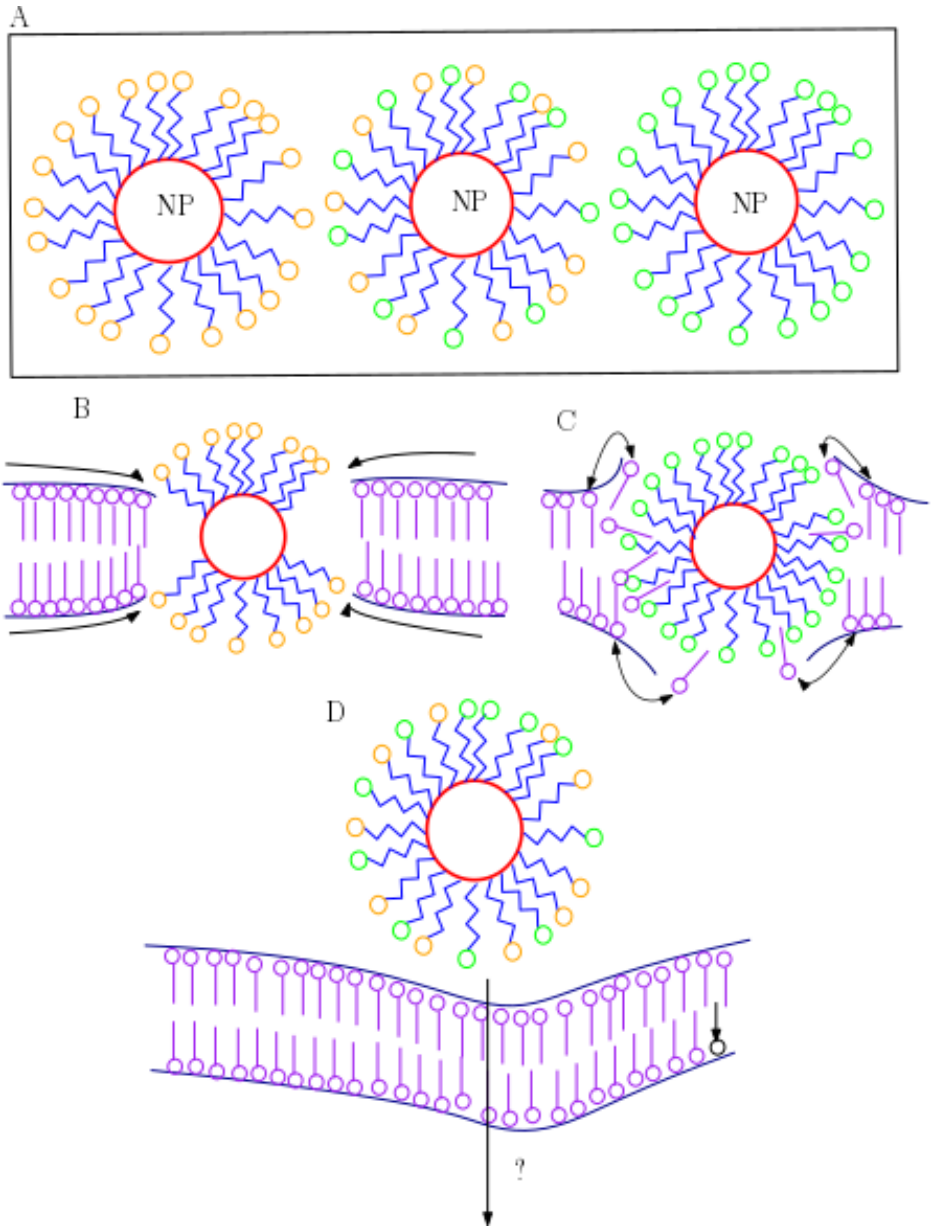

Fig. 1.7 Mechanisms associated with ligand-functionalized NPs. A shows the various types of LF-NPs that one can design - here, the yellow beads represent hydrophilic/charged components, and the green beads represent a generic hydrophobic component. B shows the snorkelling mechanism as suggested by Gekeka [93] and Van Lehn [94]. C shows the translocation mechanism for a hydrophobic LF-NP as stated by Guo *et al* [92], which states that the lipid exchange between the adsorbed ligands on the NP surface destabilises the bilayer, which induces pore formation and hence, the spontaneous translocation of the NP. D is the schematic for the mixed random-patchy surface for an 'intermediate' hydrophobicity - here, direct translocation may be the key mechanism but the consensus is unclear.

the in-numerous potential uses of all types of NPs, there are key limitations which hinder their clinical applications. One of the most outstanding issues have been the aggregation of protein-like aggregates before the targeted delivery of the NP fully occurs. This is known as the formation of the protein corona around the NP, a process known as *opsonization* [95]. The formation of a bonded network around the NP *in vivo* seems to be significant near protein-rich regions of an organism which may potentially coagulate on the surface of the NP; a prominent example of this is the formation of a protein corona around a NP - protein-rich environments such as blood can contain proteins such as albumins and globulins [96], which may form a soft-shell around the NP. This factor complicates the use of NPs for targeted therapy, as now one has to account for both the biocompatibility of a candidate NP and in addition, ensure its binding target remains consistent and unchanged due to the formations of the corona. Depending on the physiochemical properties of the NP, the nature of the corona formed differs - positively charged NPs prefer to adsorb albumin proteins [97] whilst negatively charged particles interact with proteins such as immunoglobins (IgG) [98]. The effect of the formation of the corona is shown in Figure 1.8. Studies by Salvati *et al* [99] with silica-COOH and pegylated NPs showed that transferrin proteins structures, highly abundant proteins in the mucous membrane, can effectively hinder the end groups of such ligands, which inhibited their targeting abilities. By pre-coating the ligand-functionalized NPs with proteins, progress has been made to lessen the impact of the formation of such protein coronas, but this requires further research [96].

1.4 Summary

In summary, the study of soft matter, especially the multitudes of structures that amphiphiles can form has gathered intense interest for potential applications and the potential for identifying the mechanisms behind the building blocks of cellular organisms itself. The systems of interest involve highly complex structures such as proteins, lipids, rigid lipid analogues

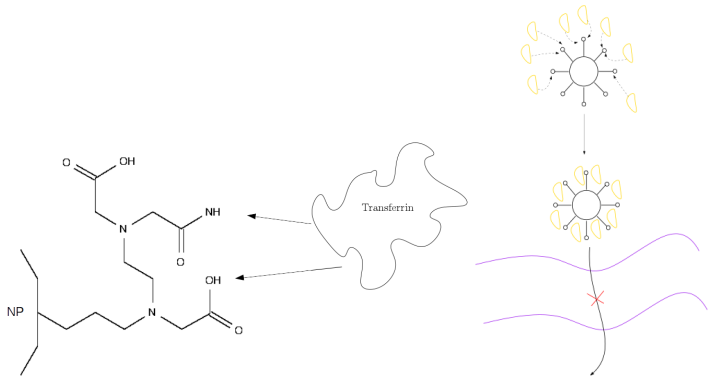

(a) (b)

Fig. 1.8 (a) shows the corona association mechanism of tranferrin upon silica-COOH NPs [99], while (b) shows the schematic of a LF-NP which may lose its selectivity across a bilayer by the accumulation of such proteins and corona on its ligands.

and must take into account the right environmental conditions such as pressure, temperature and pH. Given this complexity and delicacy of an *in vivo* system, experimental methods have limitations in the amount of information they can convey about biophysical systems, and hence, molecular simulation techniques have come into prominence to analyze such complex systems in a simulated *in vivo* environment. As discussed above, NPs can be a source of both toxicity and a novel mode of drug delivery when embedded in these amphiphilic membranes of various mixtures. NPs designed with anisotropic physiochemical surface properties can act as agents that induce local phase separation, ordering of lipid tails and induce porosity and defects for example. One of the key properties to consider has been the hydrophobicity of the NP, which controls both the mechanism of entry and the balance of cellular uptake and cytotoxicity.

1.5 Objectives and Aims

In this work, we have used MD simulations of biomimetic bilayers and specially designed NPs and analogues, to test the accuracy and efficiency of non-equilibrium free energy methods. We have also analyzed the NP/bilayer system in the normal and lateral plane of a

biomimetic bilayer; in the normal plane, we have characterised the physiochemical characteristic of a continuum model hydrophilic/mixed/hydrophobic NP with a non-ionic bilayer, and attempt to quantify the key characteristic that can be identified with the translocation of a NP with these properties. On the lateral plane, we have characterised the interaction of a hydrophobic NP of varying sizes with a induced raft-like formations in mixed bilayers.

In Chapter 2, the methodologies behind the simulation work is summarised - the review of the simulation algorithms and formulations used in MD is reviewed, and we introduce the methodologies behind *equilibrium* and *non-equilibrium* free energy biasing methods, specifically focusing on the US and SMD methods.

In Chapter 3, a comparison between the US and SMD methods is carried out, in a mixed resolution (with all-atomic (AA) and coarse grained (CG) components) system. We make critical assessments into their qualitative, quantitive and computational efficiency.

In Chapter 4, we focus on the bilayer normal as the plane of interest - the mechanisms of hydrophilic, hydrophobic and intermediate NPs is explored for R = 1.0, 1.5 and 2.0 nm NPs, with a non-ionic bilayer system.

In Chapter 5, the focus is changed to the bilayer lateral - the effect of hydrophobic NPs within domain-regions in a phase-separated bilayer is analysed. The effect of the NPs on the membrane domain as a function of size is analyzed.

CHAPTER 2

THEORY OF SIMULATIONS

2.1 Introduction

The use of simulation techniques has been aided greatly by the monumental increase in technological advancement and the development of advanced computing facilities and methodologies. Previously prohibitive simulations and large scale modelling of complex systems have become possible and the ultimate goal of molecular simulations techniques is to simulate the entirety of the molecular machinery that builds and maintains a living organism. While such a goal is still a daunting prospect, simulation techniques have been useful in understanding key processes often difficult to analyse by experimental techniques alone. In particular, the mathematical machinery of classical thermodynamics and statistical mechanics gives a powerful tool to relate molecular properties to relate relatively small simulation snapshots with macroscopic phenomena. The technique of *Molecular Dynamics* (MD) relates the total energy of the system derived from the Newtonian equations of motion to the thermodynamics properties. In this section, we attempt to give an overview of the concepts and ideas used for the simulation of molecular systems. Here, we give a brief discussion of the methodologies that have been tested in this work.

2.2 The Equations of Motion

The essence of MD is rooted in the iterative computation of the laws of motion, and hence, we discuss its basics before building up to the calculation of macroscopic properties we will be exploring in this body of work. The relationship of the *force* (F) applied to a body of *mass* (m) to it's *acceleration* (a) is well understood in terms of the relation:

$$F = ma \tag{2.1}$$

This is equivalent to the second time derivative of the position of the body, or the first time derivative of the *momenta* (p) of the body.

$$F = m\frac{d^2r}{dt^2} = \frac{dp}{dt} \tag{2.2}$$

From this expression of the force, the equations of motion for a body can be obtained as solutions to a second order differential equation. While Newton's original formulation can be applied to simple, minimal-body systems, the explicit vector form of the calculation procedure makes it unsuitable for many bodied systems. For example, for an N-body system of 10^{23} molecules, the force of each body can be formulated as:

$$F_i(r_1, r_2, ...r_N, \dot{r}_i) = \sum_{i \neq j} f_{ij}(r_i - r_j) + f^{(\text{ext})}(r_i, \dot{r}_i) \tag{2.3}$$

Where i represents the index of the molecules in the system, totaling to N molecules, and r represents the position of the ith molecule. The first term represents the forces intrinsic to a mechanical system, while the second term refers to the external input force from the system onto the particles. Different formulations of the equations of motion become convenient when expressing the positions and momementa in the system. To ease the calculation, we

introduce the *Hamiltonian* (H) formulation of classical mechanics:

$$\mathscr{H}(p,r) = \sum_{i}^{N} \frac{p_i^2}{2m_i} + \mathscr{U}(r_1....r_N) \tag{2.4}$$

The Hamiltonian formulation gives us a convenient way to obtain the positions and momenta; differentiating $\mathscr{H}$ with respect to the momenta and position gives the conservative force and momenta respectively:

$$\dot{r}_i = \left(\frac{\partial \mathscr{H}}{\partial p_i}\right) \tag{2.5}$$

$$\dot{p}_i = -\left(\frac{\partial \mathscr{H}}{\partial r_i}\right) \tag{2.6}$$

As the sum of the K and U, the Hamiltonian can be described in terms of a function of phase space variables which denote the total energy of the system:

$$\mathscr{H}(r,p) = E \tag{2.7}$$

From the time derivative of Hamiltonian i.e. from the chain rule, the generalised momenta and position terms can be exchanged for the derivatives of the Hamiltonian, which equates to zero - i.e. H is conserved over time:

$$\frac{d\mathscr{H}}{dt} = 0 \tag{2.8}$$

The preceding explanation shows how the motion of N bodies in a system can be tied to a single energy term, the Hamiltonian, which becomes very convenient when tying the N-body motions with the thermodynamic variables. Also, rather than working with a vector formulation of forces, the kinetic and potential energy terms can simply be summed into forming the Hamiltonian K and U components.

2.3 Relating Statistical Mechanical Concepts to Simulation Mechanics

Classical thermodynamics gives a robust system for deriving the *intensive* (ones that do not depend on the size of the system) and *extensive* (ones that are proportional to the size of the system) properties of a system from direct measurements from the system such as the temperature, pressure and concentration. We know the first law of thermodynamics as an expression of the conservation of energy:

$$E = Q + W \tag{2.9}$$

where the total energy of the system can be related to the heat (Q) absorbed and the work (W) done on the system. Hence, in a reversible (infinitely slow) process, we can denote the change in energy as the reversible change in heat and work:

$$dE = dQ_{\text{reversible}} + dW_{\text{reversible}} \tag{2.10}$$

The change in heat and work can be decomposed into its individual components; the change in heat is related to the change in entropy (S):

$$dS = \frac{dQ_{rv}}{T} \tag{2.11}$$

on the other hand, the work can be divided into terms of *mechanical work* and *chemical work*. The mechanical work depend on the change in volume and the pressure:

$$dW_{rv,\text{mechanical}} = -PdV \tag{2.12}$$

(Where the minus sign represents work done *against* the system). The chemical work term depends on the chemical potential and the change in the number of molecules in the system:

$$dW_{rv,\text{chemical}} = \mu dN \tag{2.13}$$

substituting all these terms into the expression for the change in energy, we obtain:

$$dE = TdS - PdV + \mu dN \tag{2.14}$$

the dS and dE term can be exchanged to obtain a part-wise term for the total change in entropy:

$$dS = \frac{1}{T}dE + \frac{P}{T}dV - \frac{\mu}{T}dN \tag{2.15}$$

as the entropy can be defined in terms of the number of molecules, volume of the system, and the total energy - i.e. the differential of S(N,V,E) can be written as:

$$dS = \frac{\partial S}{\partial E}_{N,V} dE + \frac{\partial S}{\partial V}_{N,E} dV + \frac{\partial S}{\partial E}_{V,E} dN \tag{2.16}$$

Here, it is useful to consider to idea of *ensembles*. As an example, N many-body system with identical volume, temperature, pressure and number of molecules, if evolved dynamically over an infinite amount of time, will result in the same conformations and system properties i.e. we will always get the same equilibrium properties. However, this infinite-interpretation can also be looked at as an average of a series of 'snapshots' of the system over a dynamical evolution, where each 'snapshot' is defined as the *microstate*, and hence, the average of the microstates can be defined as the *ensemble average*. Relating this idea back to our interpretation of the entropy, we can approximate the entropy with the averaged entropy of

the ensemble. The ensemble entropy can be expressed as:

$$S = k_B \log \Omega \tag{2.17}$$

Where Ω is the number of unique ways of arranging the microstates in the system, and k_B is Boltzmann's constant. By using the ensemble concept, we can eliminate the need to fine-tune a system at the *start* of a simulation, and rather, evolve the system over a sufficient period of time to equilibration to obtain ensemble averages. As the number and flux of microstates is conserved, at any given point in time, the macroscopic observable, A , can be computed through its microscopic equivalent phase space function, a:

$$A = \langle a \rangle = \int f(x,t)a(x)dx \tag{2.18}$$

which is the standard protocol for calculating a mean from a probability distribution. Equation 2.17, hence, gives us the first useful relation in linking to microscopic with macroscopic observables. While this interpretation is useful, it is still limited by the fact that the number of microstates we require to sample to gain a equilibrium macroscopic property may not be computationally viable for systems of very large numbers of molecules and complexity. However, by simulating a smaller system that is *representative* of the larger macroscopic system in mind, it is possible to obtain useful information from the system. From a practical point of view, the *time average* can be used as the approximation of this *ensemble average* of microstates. An observable at time t, a_t, for example, may be approximated by the time average by:

$$A_{\text{ensemble}} = \frac{1}{\mathscr{Z}} \sum_{i=1}^{\mathscr{Z}} A_i = \langle a_t \rangle \tag{2.19}$$

MD simulations, as demonstrated in this work, make exclusive use of the time average - in addition, compared to its sister technique, the *Monte Carlo* method, the dynamics of all the particles in the system are evolved at the same time, which allows us to gain both equi-

librium and dynamical information. Hence, to be comparable to a true ensemble average comparison, the time average must cover the majority of the sample space. The ensemble interpretation, so far, has been limited to exploring the microcanonical (i.e. an isolated system of a set volume, evolved by Hamiltonian mechanics). Such an ensemble only describes a system described by the state function S(N,V,E).

Within this study, we have simulated systems representative of those that are within the homeostatic environment of an organism. As most experiments in biophysical environments are concerned with conditions of constant temperature or constant pressure with changing numbers of particles, the Hamiltonian of the system must be amended to take these changes into account. For example, when the *volume* and *temperature* are set as constant, one can define the phase space distribution for the *canonical ensemble* (*NVT*). Here, the probability density of the ensemble can be defined as:

$$f(p^N, r^N) = \frac{\exp\left[-\frac{\mathscr{H}(p^N, r^N)}{k_B T}\right]}{\mathscr{Q}_{\mathrm{NVT}}} \tag{2.20}$$

where p^N is the momenta, r^N is the position, $\mathscr{H}(\mathrm{p}^N,\mathrm{r}^N)$ is the Hamiltonian of the system, and $\mathscr{Q}_{\mathrm{NVT}}$ is the partition function of the system. Here, the partition function acts as the normalizing factor for the probability distribution, but it also measures the number of microstates that is accessible in the ensemble. Hence, it is the complete thermodynamic description of the system, and is arguably the central property of statistical mechanics. This is especially so, as the partition function holds the crucial key for the free energy of the system. Within the NVT framework, it is related to the Helmholtz free energy (A) by:

$$A = -k_B T \ln \mathscr{Q}_{\mathrm{NVT}} \tag{2.21}$$

when the *pressure* and *temperature* are set constant, we can describe the *isobaric-isothermal* ensemble (*NPT*), which is closest to emulating a biophysical environment, and hence, the central ensemble to work with. The central property, the Gibbs free energy (G), is obtained from the Legendre transformation of A:

$$G(N,P,T) = A(N,V(P),T) - V(P)\frac{\partial A}{\partial V} \tag{2.22}$$

as P = -$\frac{\partial A}{\partial V}$, the fraction term is replaced and hence, we have a new expression for G:

$$G(N,P,T) = A(N,V,P(T)) - PV(P) \tag{2.23}$$

The corresponding probability distribution in the ensemble is given by:

$$f(p^N,r^N) = \frac{\exp\left[\frac{pV+\mathscr{H}(p^N,r^N)}{k_BT}\right]}{\mathscr{Q}_{\mathrm{NPT}}} \tag{2.24}$$

Where $\mathscr{Q}_{\mathrm{NPT}}$ is the partition function for the isobaric-isothermal distribution. Again, the partition function is used to compute G:

$$G = -k_BT\ln\mathscr{Q}_{\mathrm{NPT}} \tag{2.25}$$

In practical terms, both the NVT and NPT conditions are used for our simulations - the NVT simulations are used as testing and starting for the simulation, as the constant volume provides a controlled environment which can control the initial artefacts arising from unequal energetic distributions across the system, and for the system to 'settle'. To evaluate a realistic biophysical environment, this ensemble is switched to a NPT environment after the system has been assessed to have 'settled'.

2.4 MD - the Computing Procedure

To iterate the movements of molecular bodies in the system of interest, MD simulation uses a step-wise approach to evolving the positions and velocities of a system with a user-defined period of time. Each MD simulation requires the same protocol of preparation as practical experiments; the external parameters such as temperature, pressure and concentration, and a period of time must be allowed for the experiments to occur.

As stated before, the ensemble average observable of a system can relate the microscopic detail of the particles in the system with observable macroscopic properties. To approximate the ensemble average in a single simulation of particles under Hamilton's equations of motion, we define the time average of the trajectory:

$$\langle A \rangle_{\text{time}} = \lim_{t \to \infty} \frac{1}{\tau} \int_0^{\tau} A[r^N(t), p^N(t)]dt = \frac{1}{\mathscr{L}} \sum_{i=1}^{\mathscr{L}} A(p^N, r^N) \tag{2.26}$$

where t is the simulation time, $\mathscr{L}$ is the total number of timesteps and A(p^N, r^N) is the instantaneous value of A. The equations of motion for each molecule are solved through a discrete step-wise algorithm - here, there are two main concerns - the time convergence of the system, and how short we want to discretize the simulation timestep that computes and modifies the trajectory of the system according to the forces that are acting on it. The analytical timestep for calculating the motion is done as infrequently as possible due to the computational cost. The three primary algorithms for timestep iterations are the *Verlet* [100], *Leapfrog* [101], and the *Beeman* [102] algorithms. From these, the *Verlet* implementation has been utilised commonly due to its efficiency, and its moderate storage requirements. Here, we give a brief explanation of its implementation; the *Verlet* algorithm uses a second order taylor expansion of the position of a particle around δt. For the position propagation

over time:

$$r(t+\delta t) = r(t) + \delta t \dot{r}(t) + \frac{1}{2}\delta t^2 \ddot{r}(t) \tag{2.27}$$

the *Verlet* algorithm takes advantage of the fact that the first and second time derivative of the position is the velocity (v) and acceleration (a) respectively. Hence, the $\dot{r}(t)$ term can be substituted for the velocity v(t) and the $\ddot{r}(t)$ can be substituted for $\frac{F(t)}{m}$:

$$r(t+\delta t) = r(t) + \delta t v(t) + \frac{1}{2m_i}\delta t^2 F(t) \tag{2.28}$$

by summing the above term with the backwards propagation step, one can eliminate the velocity term to form a propagation algorithm that is independent of the velocity:

$$r(t+\delta t) = 2r(t) - r(t-\delta t) + \frac{\delta t^2}{m} F(t) \tag{2.29}$$

The Verlet algorithm provides a format for a position/momenta propagator which is easy to implement by code.

2.5 Molecular Mechanics - Building the Potential Term for the Hamiltonian

MD simulations treat each molecule in the system by dividing the molecular components into the intermolecular and intramolecular potentials. In general, the collection of terms for a series of molecular types is defined as a *force field* (FF). Figure ... shows the visual representation and the potential terms involved in the makeup of a molecular FF. The intramolecular FF terms are divided into the *covalent* and *non-covalent* terms. The covalent terms are divided into the *bond*, *angular* and *torsional* (or dihedral) terms, as shown with the restraint on the r (distance), θ (angular), and ϕ (torsion). The non-covalent intermolec-

ular terms are the *Coulombic* potential and the *Lennard-Jones* potential, which model the electostatic and Van Der Waals (VdW) interactions respectively. The LJ term for example, has a particular computational efficiency due only having to compute 2 terms explicitly. The parameters are η (the depth of the well) and σ (the distance at which the potential is zero) and the $\frac{\sigma}{r}^6$ only needs to be computed once, and squared. When assessing the Coulombic electrostatic terms, caution must be taken, as the system is simulated in a finite-size box that must be large enough to prevent potential simulation artefacts. The molecules in a simulation box will be affected physically by the boundaries of the box. To overcome this, *periodic boundary conditions* (PBC) replaces the boundary of the box with replicas of the box. The system is simulated in a finite-size box that must be large enough to prevent potential simulation artefacts. The molecules in a simulation box will be affected physically by the boundaries of the box. To overcome this, *periodic boundary conditions* replaces the boundary of the box with replicas of the box. Figure 2.3 illustrates this with a box of water molecules. As the Coulombic terms are inverse-squared terms and long-ranged, the effect of the PBC must make sure that the electrostatic potentials in one PBC box does not affect the physics i another box. Hence, the *Ewald particle mesh method* [103] was developed to divide the Coulombic terms into *short-range* and *long-range* terms - where the long-range terms are described in reciprocal space. While the implementations of FFs has been relatively successful, one of the main drawbacks of such a description of molecules comes from its computational efficiency - extraneous computations, such as the iterative step-wise motion of hydrocarbon C-H bonds and bulk alkyl chain regions are not interesting from the view of observing phenomena, but requires significant computational resources to process. This considerably limits the range of systems that may be explored by molecular simulations. Hence, to alleviate this issue, simplifying techniques were developed, to reduce the level of detail of computation required in uninteresting regions. To distinguish the levels of detail, the explicit atomic description is known as the *all-atomic* method, while the simpli-

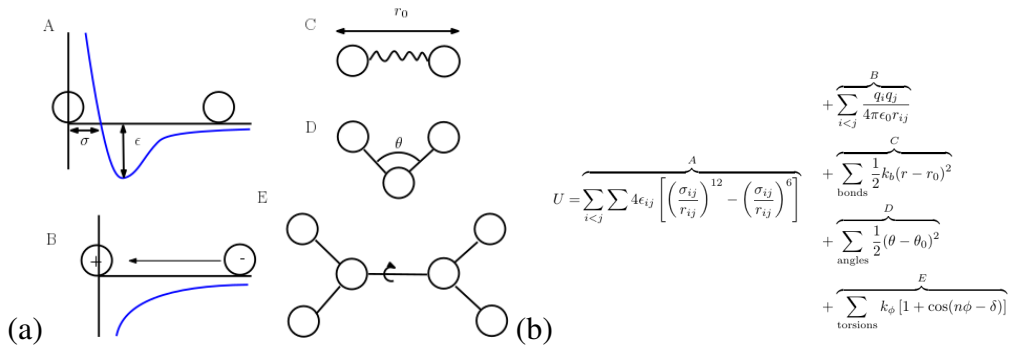

Fig. 2.1 (a) shows the schematic of the molecular mechanics (MM) components, with the corresponding functional form shown in (b) respectively.

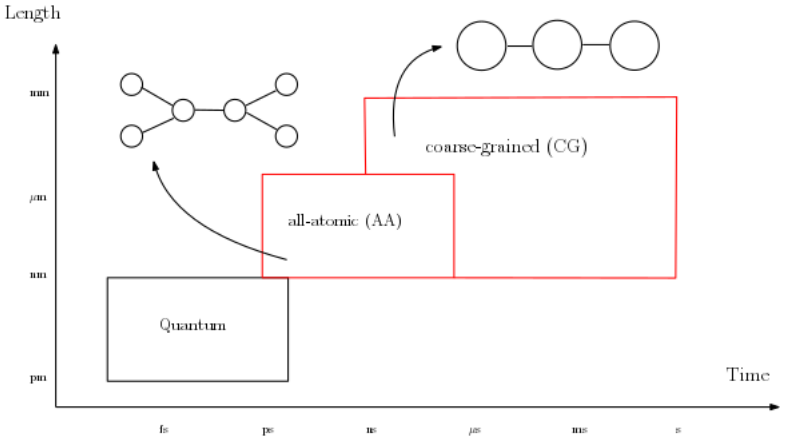

Fig. 2.2 The time scaling of simulation methods with its level of atomistic detail - with this work, we are primarily concerned with the interface between the all-atomic (AA) and the coarse-grained (CG) detail simulations, which are annotated in red.

fied models are known as *coarse-grained* models. An example of a coarse-graining (CG) method is the inverse boltzmann method [104], which follows an iterative procedure for reproducing the structural radial distribution around a group of AA detail molecules from the radial distribution function (g(r)):

$$V_{\mathrm{i+1}}^{\mathrm{CG}}(r) = V_{\mathrm{i}}^{\mathrm{CG}}(r) + k_B \ln\left[\frac{g_i(r)}{g_{\mathrm{ref}}(r)}\right] \tag{2.30}$$

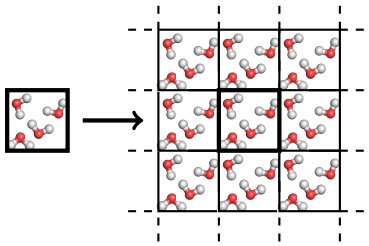

Fig. 2.3 The general outline for a periodic boundary condition, with water molecules inside each simulation box. The minimum image convention (MIC) must be taken into account when performing analysis of simulation results.

where the initial approximation of the $V_{\mathrm{i}}^{\mathrm{CG}}(r)$ is taken from the boltzmann inversion of the reference radial distribution function from AA simulations:

$$V_{\mathrm{PMF}} = k_B T \ln[g_{ref}(r)] \tag{2.31}$$

other methods include the force-matching (FM) method [105]. Figure 2.2 shows the relative place of AA and CG simulations on the scaling limits of simulation. Figure 2.2 shows the gain in computational time as a result of this CG procedure - we can see that CG methodologies extend the simulation timescales from scales of nanoseconds (ns) to near seconds.

In summary, we can summarize the process of setting up a MD simulation in the following steps:

- The positions and initial velocities (r, p) of the molecules are set.
- The atomic forces are calculated based on the potential model/force fields used (e.g. CHARMM, AMBER, GROMOS), which are incorporated into the potential energy term U of the Hamiltonian.
- Using the step-wise (typically *Verlet*) algorithm, the molecular motions are calculated.
- The coordinates of the molecules after the designated timestep is recorded, and set as the new point of change.

- The process is iterated until the designated end point.

- The final result is produced in a format (depending on the simulation package used).

2.6 Free Energy Calculations in Molecular Simulations

One of the most daring assumptions made in MD simulations is that it follows the ergodic theorem, where the system has been fully able to equipartition the energy around the entire system. While this assumption may be true on average, this assumption clearly breaks down near high-energy regions, where observation and intuition would indicate that an energy input is required for processes to overcome energetic barriers - for example, arising from unfavourable energy peaks arising from conformational mismatch of rotating dihedral angles of proteins, unfavourable regions of hydrophobic/hydrophilic interaction forming energetic barriers, and ligand docking reactions with protein structures. Hence, these high energy states in the system represent rarely sampled regions, and numerous sample biasing methods have been developed to reach these points in phase space. One of the major stumbling blocks with MD simulations is that it only samples the low energy configuration.

Unfortunately, the high energy barriers which are present in a system often represent the most mechanistically interesting - for example, the rotation of a molecule, the changing conformations in protein folding, and the translocation of molecules across a lipid bilayer. In all these example cases, the MD method fails to adequately sample these configurations in the computational time allocated. Hence, *biased-sampling* methods have been developed to adequately sample these coordinates. Here, we discuss the *umbrella sampling* (US) and the *steered molecular dynamics* (SMD) method, which have been used to extract the free energy change across these high energy regions.

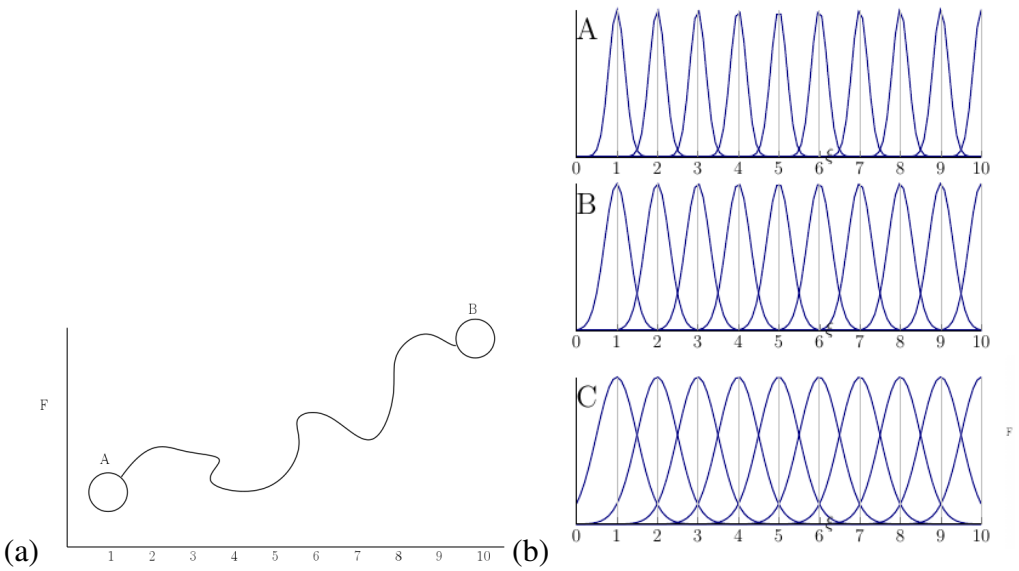

Fig. 2.4 (a) shows an illustration of the type of pathway which would require a bias-sampling method for an accurate free estimate, where A and B are the starting and ending points, and we see a highly irregular free energy surface in-between. (b) illustrates the care required in assuring the 'right' overlap between the US windows, where A shows an inadequate overlap, B shows the right amount of overlap, and C shows an excessive overlap between the US windows

2.6.1 Umbrella Sampling

The free energy change is an indicator of the thermodynamic stability of the system, and the magnitude and sign governs the direction of *spontaneous change*. Hence, obtaining the correct quantitive free energy change across a reaction path has been an important goal in the application of molecular simulation techniques, and one of the key advantages of simulation methods over experimental methodology, so that the full weight of mathematical machinery can be applied to a highly controlled experiment. Zwanzig [26] introduced the *thermodynamic perturbation method* (or the free energy perturbation, FEP), which introduces a 'ghost' state in-between the starting state and the desired end state. However, the artificial intermediate step that is required for the perturbation method is only valid when

the phase spaces for the starting state (A) and end state (B) are with sufficient phase space overlap. Also, high energy barriers and the difficulty of locating state B from A confounds this problem for large reaction coordinates (RCs). To surmount this problem, Torrie and Valleau [106] introduced the US method. This method introduces a bias potential to the H(r,p) which restrains the system at the required RC, ξ:

$$\mathscr{H}_{\text{Umbrella}}(r,p) = \mathscr{H}(r,p) + w_i(\xi) \tag{2.32}$$

where $w_i(\xi)$ is the weighting factor, and ξ is the reaction coordinate of interest:

$$\xi = R(r) = R(r_1, r_2 .... r_n) \tag{2.33}$$

The ΔG/A over the trajectory ξ is known as the *potential mean force* (PMF) (the average force over all the configurations of the molecules in the system acting on the reaction co-ordinate). The US method typically adds a *stiff spring potential* as the weighing factor:

$$w_i(\xi) = \frac{k}{2}(\xi - \xi_{\text{ref}})^2 \tag{2.34}$$

where k is the spring constant, and $\xi_{\text{reference}}$ refers to the reference point from which the particle can move around. By adjusting the spring constant, the molecule can be held closer/further from the RC. US requires a 'screenshot' method, where a weighting term must be defined for each r value sampled. In order to obtain accurate information about the free energy of the system, the raw data from individual 'screenshot'/bin must be unbiased and merged. Each window must be adequately be sampled to equilibrium i.e. where there is no change in the distribution as a function of time. The probability distribution function of the biased potential energy $\mathscr{H}'(r,p)$ (that has been biased with the bias potential $w(\xi)$)

is:

$$P'(\xi) = \frac{e^{\left(\frac{\mathscr{H}'(r,p)}{k_BT}\right)}\delta(f_\alpha(r_1,...,r_N)-\xi)d^Nr}{\int e^{\frac{\mathscr{H}'(r,p)}{k_BT}}d^Nr} \tag{2.35}$$

The unbiased probability distribution function is described by:

$$P(\xi) = \frac{e^{\left(\frac{\mathscr{H}(r,p)}{k_BT}\right)}\delta(f_\alpha(r_1,...,r_N)-\xi)d^Nr}{\int e^{\frac{-\mathscr{H}(r,p)}{k_BT}}d^Nr} \tag{2.36}$$

hence, by substituting expressions for the the biased and unbiased probability into equation 2.32 the distributions can be linked by the following equation:

$$P'(\xi) = e^{\left(\frac{w(\xi)}{k_BT}\right)}P(\xi)\langle e^{\left(\frac{-w_i(\xi)}{k_BT}\right)}\rangle^{-1} \tag{2.37}$$

Hence, each unbiased PMF for each window is:

$$G_i(\xi) = -k_BT\ln P'(\xi) - w_i(\xi) - k_BT\ln\langle e^{\frac{-w_i(\xi)}{k_BT}}\rangle \tag{2.38}$$

With a series of $G_i(\xi)$ values along the RC, we can measure the change in PMF as a function of the coordinates along RC, which is the free energy change along the RC. Hence, in practical terms, the free energy change and the PMF can be used as interchangeable terms. The -$k_BT\ln\langle e^{\frac{-w(\xi)}{k_BT}}\rangle$ term is known as the *free energy constant* in literature and is often separately defined as F. Hence, unbiased PMF for each window becomes:

$$G_i(\xi) = -k_BT\ln P(\xi) - w_i(\xi) + F_i \tag{2.39}$$

where the i in F_i denotes the biasing window in question. Hence, finding the F_i for each biasing window becomes key to unbiasing potential. F_i can be computed by:

$$e^{\left(\frac{-F_i}{k_BT}\right)} = \int P(\xi)e^{\left(\frac{-w_i(\xi)}{k_BT}\right)}d\xi = \int e^{\left(\frac{-w_i(\xi)-G_i(\xi)}{k_BT}\right)}d\xi \tag{2.40}$$

In the case of reweighting multiple biased sampling windows and 'attaching' them together, methods that do this include the *weighted histogram analysis method* (WHAM) [25, 28] and the *umbrella integration* (UI)[24]. The application of UI or WHAM needs to ensure the histogram bins have 'sufficient' overlap to obtain a PMF without holes/gaps corresponding to inadequate sampling. This is illustrated in Figure 2.4. Practically speaking, increasing the sheer number of windows along the RC does not necessarily improve the convergence rate. The choice of spring constant required for each bin often require multiple iterations of trial and error which requires wasted simulation and resource time.

2.6.2 Non-equilibrium Methodologies - Jarzynski Equality (JE)

As a more recent and a sister method to the US, which enhances the sampling in high energy states through equilibrium-like simulations assessed together, the *non-equilibrium* method follows the exact opposite approach, where the equilibrium free energy change values are extracted from simulations far away from equilibrium. A free energy change between state A and state B of a system is connected to the work done to produce that change by the work inequality:

$$W \geq \Delta F \tag{2.41}$$

where ΔF is the free energy change of the process, and W is the irreversible work. The inequality represents the contribution of the residual or *dissipative* work when the process is carried out in a non-equilibrium regime, while the equality is representative of when the process is carried out reversibly (extremely slowly). For example, if we want to change the conformation of a molecule from state A to state B, the work performed is interpreted as a time integral of the Hamiltonian:

$$W = \int_A^B dt \dot{\lambda} \frac{\partial \mathscr{H}}{\partial \lambda}(\xi, \lambda) \tag{2.42}$$

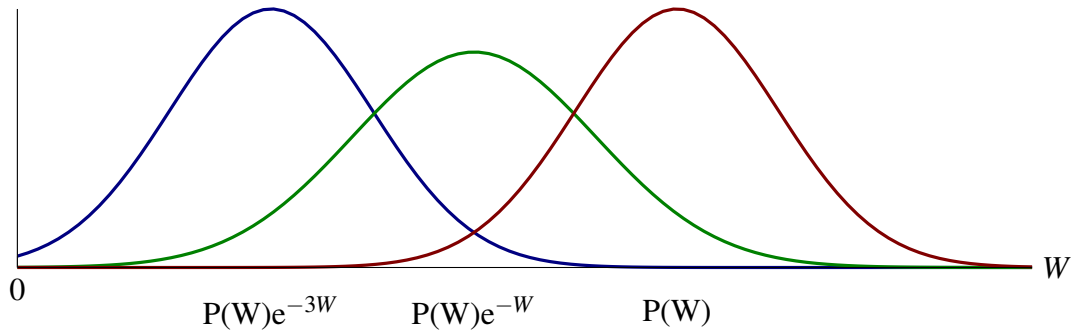

Fig. 2.5 The shift of the Gaussian work distribution with different Boltzmann factors. Even through a very simple multiplication with the exponential function, we can see a significant shift away from the true work distribution, P(W). Hence, modifications of the JE expression is necessary.

hence, unless a process is driven incredibly slowly, due to the work inequality, it can only give a marginal insight into the true free energy process. Jarzynski [31] however, showed that the average exponential work can be related to the exponential of the free energy change; this expression is modified so that it becomes an equality:

$$\langle e^{\frac{-W}{k_B T}} \rangle = e^{\frac{-\Delta F}{k_B T}} \tag{2.43}$$

This relation shows that the averaged work given over non-equilibrium reactions gives information about the free energy, which is *equilibrium* state information. This new equality represents the change in perspective from a macroscopic to a microscopic system; as the fluctuations within a system is statistical, it is correct to say that the work inequality is applicable with certainty to systems containing extremely large numbers of molecules. However, what the JE stated was that, with microscopic systems, the contribution from the *negative* work done on the system may contribute significantly to the work observed [107]. One of the main suggested advantages of the JE method is that the work extracted from very fast changes of system can extract the free energy, an equilibrium state function.

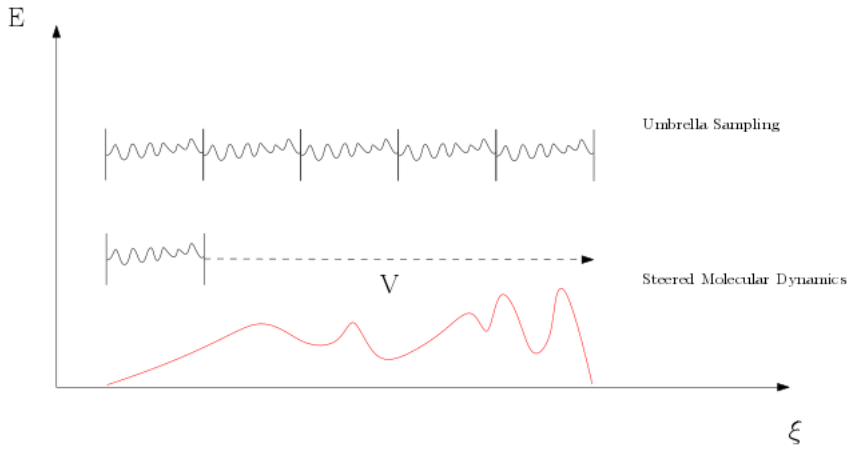

Fig. 2.6 The schematic of a US and a SMD simulation - the US approach requires multiple sampling bins to increase the sampling across high energy regions, while the SMD method shows a moving spring across the free energy surface. The surface in red shows a sample free energy surface that may be mapped by these methods

Extracting the Work in MD Simulations through the Steered Molecular Dynamics (SMD) Method

By multiplying the displacement of the molecular component with the force, a series of work values can be exhibited. One can now apply the JE to calculate the free energy change during the interval from starting state A at time τ_A to end state B at τ_B, by applying a guiding potential to obtain the appropriate work distribution. The guiding potential from A to B follows the form of a stiff spring potential, which has an identical form to that used in the US method:

$$w_i(\xi) = \frac{k}{2}(\xi - \xi_\lambda)^2 \tag{2.44}$$

For a *constant velocity* SMD simulation, the external parameter constraining ξ will have the form:

$$\xi_\lambda(t) = \xi_{\mathrm{SMD}}(0) + vt \tag{2.45}$$

The $\xi_{\mathrm{SMD}}(0)$ represents the point in phase space at the starting point of the RC. The velocity, v, is given analytically before the simulation is started. Hence, the overall form of the

Hamiltonian for the SMD trajectory becomes:

$$\mathscr{H}_{\mathrm{SMD}}(r,p) = \mathscr{H}(r,p) + w_i(\xi) \tag{2.46}$$

from this modified Hamiltonian, the PMF of the RC can be calculated from the stiff-spring approximation method, as shown by Schulten and Park [108], and further detail can be found in the referenced paper. The work done in each trajectory is calculated by a time integral of the Hamiltonian, as stated before:

$$W(t) = \int_0^\tau dt \left[\frac{\partial \mathscr{H}_{\mathrm{SMD}}(r,p)}{\partial t} \right] \tag{2.47}$$

thus, applying the JE to this, the free energy change can be calculated via the relation:

$$\Delta F = -\frac{1}{\beta} \log \langle exp[-\beta W(t)] \rangle \tag{2.48}$$

using these relations, to calculate the overall PMF, the spring constant (for the stiff spring potential is interpreted to be strong enough so that the molecule we are moving at constant velocity does not deviate far from the chosen RC, ξ. The PMF is related to the free energy change through the following relation:

$$\exp(-\beta F_\lambda) = \int d\xi exp \left[-\beta \Phi(\xi) - \frac{k}{2}(\xi - \xi_\lambda)^2 \right] \tag{2.49}$$

Where Φ represents the PMF. The assumption we take with this interpretation is that the spring constant is chosen so that the RC is identical to the work potential i.e. $\xi = \lambda$. We can approximate the $\Phi(\xi)$ term using a taylor expansion [108]. Hence, an expression for the free energy change can be rearranged for the $\Phi(\xi)$ (i.e. the PMF) of the trajectory.

$$\Phi(\lambda) = F_\lambda + \frac{1}{2k} \left(\frac{\partial F_\lambda}{\partial \lambda} \right)^2 - \frac{1}{2\beta k} \frac{\partial^2 F_\lambda}{\partial \lambda^2} + O(\frac{1}{k^2}) \tag{2.50}$$

As we know the term for the F_λ from the JE, this equation can then be used to calculate the PMF. There are some known issues with using the JE for calculating the PMF. One of the issues is that the exponential work term, $\langle e^{-\beta W} \rangle$, shifts away from the true work distribution - this is shown in Figure 2.5 which shows the significant shift of the exponential work distribution when we take β values of -1 and -3. Secondly, it is not certain that with a sufficiently high pulling force/velocity, the sampled distribution on the RC will be an equilibrium distribution. To overcome the first difficulty, Schulten *et al* [108] suggested a correction term of the JE free energy expression, using a truncated cumulant expression:

$$\ln \langle e^{-\beta W} \rangle = \beta \langle W(t) \rangle - \frac{\beta}{2} (\langle W(t)^2 \rangle - \langle W(t) \rangle^2) \tag{2.51}$$

this expression essentially shifts the work distribution back from where it would be after the exponential multiplication. However, even this is only in the case when the contribution from the dissipative work only shifts the work distribution near the tail regions of the actual work distribution Gaussian; if this is not the case, the sampled work would not be near the equilibrium region, which would question the practical use of the JE. This improved sampling interpretation was presented by Schulten *et al* [108]. Hence, one of the main focuses of this work is the convergence of the free energy profiles across a complex, high energy barrier of the JE-SMD technique, compared with the US technique. If we assume that the US does indeed, give the *true* free energy profile across a coordinate, *is it better to use a single slow simulation, or multiple fast simulations for SMD?* If the sampling time for the 'slow' method extends beyond the total sampling time for US sampling bins, then the entire purpose of using a non-equilibrium sampling method is redundant and hence, further investigation is required to revalidate the applicability of this kind of non-equilibrium methods.

2.7 Conclusion

In this Chapter, we have shown an overview of the MD technique as a method of simulating the real-time physics of a many-body system, and two branches of *bias-sampling* techniques which have been utilised to analyse the free energy change across high energy regions, known as *equilibrium* and *non-equilibrium* methods, of which we have reviewed the US and the JE-SMD method. One of the key goals in this work is to compare the free energy profiles produced between these methods for the RC across a model bilayer normal, a complex RC where we see multiple physiochemical characteristics, convergence properties and free energy barriers, and to establish the computational efficiency and quantitative accuracy of each method in comparison.

CHAPTER 3

THE COMPARISON OF UMBRELLA SAMPLING METHODS AND STEERED MOLECULAR DYNAMICS FOR COMPUTING FREE ENERGY PROFILES OF TOLUENE MOLECULES THROUGH LIPID BILAYERS

3.1 Introduction

The properties of lipid bilayers *in vivo* has been a subject of much interest due to the large variety of structures these can form. The factors that affect the macrostructure and stability of the bilayer are complex, involving the chemical composition of the head and tailgroups, headgroup area, tailgroup composition, and the hydrophilicity/hydrophobicity of the chemical moieties composing the bilayer. Given the complexity of the systems involved, experimental methods such as AFM and fluorescent microscopy have limitations on the level of elucidation possible, and often, the experimental preparation does not represent the *in vivo* situations, which means that it can only give partial insight into the system. Hence, *molecular simulation* techniques have become a powerful method for measuring properties when that is impractical in experimental conditions. As the system can be set and adjusted with fixed parameters (such as pressure, volume, chemical potential), it is possible to use the

tools of statistical mechanics to compute the state variables. In particular, the *free energy* (FE) of processes has become an essential property to compute.

Among the equilibrium sampling methods, the *umbrella sampling* (US) method has been ubiquitous in its use, due to its intuitive nature and relative simplicity of implementation. The weaknesses of the US method comes from its high computational cost - the high energy parts of the phase space needs to be sampled adequately with the right overlap between each sampling space, and the discrete sampling each bin of the reaction coordinate requires a large trial and error process to find parts that may require additional sampling bins. Alternatively, Jarzynski [31] demonstrated a revolutionary equality (known in the literature as *Jarzynski's equality* (JE)), which showed that, independent of the velocity of the process (hence, can be a non-equilibrium process), the *force-distance* curve along the reaction coordinate can be used to compute the work i.e. a path-dependent function can be used to compute the free energy of the process, an *equilibrium* state function.

The calculation of the free energy using JE based methods introduced *fast-switching* events as a possible efficient alternative to the US method. Should the validity of the equality be widely applicable, the advantage of the method compared to the US method is obvious - one would not need to sample so many discrete bins along the reaction coordinate, which would allow saving of computational resources and allow the calculation of a much greater range in reaction coordinates. By adapting a moving Hooke's Law potential, Schulten *et al* suggested using the *steered molecular dynamics* method [108] which can constrain the particle/molecule across the reaction coordinate and compute the work distribution which is required for the calculation of the FE (Hence, we abbreviate this practical implementation of JE as JE-SMD). Previous studies comparing the US and JE-SMD have established that the SMD method can give comparable results to the US method for an accurate estimate

of the free energy profiles, depending on the velocity chosen for the moving harmonic potential. However, evidence has also arisen which suggests that sampling issues arise when implementing the method for complex many body systems. Previous verifications of the JE involve relatively simple processes, such as the extension of a DNA residue [108] and the unfolding of RNA hairpins [109], which does not therefore, dismiss the possibility of error in the JE-SMD method when applied to many body systems. The trial systems which were used to verify the JE method used a Langevin dynamics parameter to mimic thermal fluctuations, and it's small size allowed the repeated simulations (of the order 10,000 runs and more) to be done with ease, which are situations not available in the vast majority of complex reaction coordinates, where the simulation costs relating to the level of atomic detail and size are the limiting factors for making a comparable number of simulations.

Kuyucak *et al* [110, 111] showed that the JE-SMD free energy measurements in comparably 'complex' systems, such as the flow of water molecules across a carbon nanotube and a gramicidin A/bilayer channel, suggested that there was a greater inconsistency in the JE-SMD method in comparison with the US method in the gramicidin example, when there are stronger fluctuations in the surrounding system, there is a greater discrepancy of the free energy change compared to the US method. However, in each of these cases, the reaction coordinate consisted of a pathway that consists of a rigid, channel-like structure through the bilayer, rather than interacting with the undulating elements of the lipid groups themselves: A comparative study of the JE-SMD method with the US simulation with a solute and a *dynamic, unconstrained* bilayer system has, to this author's knowledge, not been attempted and tested for use. If the JE-SMD method proves to give identical free energy profiles with a reduced number of sampling simulations in comparison to the US method, this would suggest that the JE-SMD method acts as a superior alternative method to the US method. Bench-marking and comparing the US and JE-SMD free energy methods in a

sample membrane-like environment, therefore, is the purpose of this work. To measure the accuracy of free energy methods in bilayer translocation simulations, we have used sample systems with well-known chemical moieties - we have simulated a small hydrophobic molecule type (toluene) to compare and contrast the SMD method with known literature, and to assess the sensitivity of the free energy profile on the velocity of the moving harmonic potential, and to measure the degree of error that may be present between the JE-SMD and the US simulations.

3.2 Simulated Systems

3.2.1 Forcefield Parameters

Each simulation was run with the LAMMPS molecular dynamics package [112]. The *ELBA* biomolecule *mixed resolution* coarse-grained and all-atomic (CG-AA) compatible MD-forcefield was provided from the research group of Mario Orsi and Jonathan Essex [13, 113]. The AA-CG compatibility of ELBA allows an arsenal of explicit FF potentials to be used in combination with the CG-lipid forcefield; the interatomic potentials of the GAFF (*General Amber Force Field*) [114] can be combined with the CG potentials of the lipid molecules. Hence, the model allows inter-compatibility with the traditional AMBER force field (consistent AM1-BCC charge models with identical VdW parameters) which gives it wide applicability to known libraries of small molecules. The *ELBA* FF parameters have been described in detail in the literature [13], so a brief description of the forcefield will be described here. The ELBA model non-bonded cut-off potentials are explicitly treated via

the modified LJ equation:

$$U_{ij}^{LJ} = 4\varepsilon C_1 \left[\left(\frac{\sigma}{r_{ij}}\right)^{12} - \left(\frac{\sigma}{r_{ij}}\right)^{6} \right] + \left[6\left(\frac{\sigma}{r_c}\right)^{12} - 3\left(\frac{\sigma}{r_c}\right)^{6} \right] \left(\frac{r_{ij}}{r_c}\right)^{2} - 7\left(\frac{\sigma}{r_c}\right)^{12} + 4\left(\frac{\sigma}{r_c}\right)^{6} \tag{3.1}$$

where ε and σ are standard LJ parameters, r is the distance between particles, and r_c is the cutoff distance. C_1 represents the parameter for the CG-AA interaction, chosen empirically as 0.5 [115]. A novel addition compared to the CG-MD models such as Shinoda-Devane-Klein (SDK) and MARTINI [11, 15] is the inclusion of dipole moments in the lipid headgroups and the water molecules [13]. The dipole moments computed via the relation:

$$U_{ij}^{\mu\mu} = \frac{1}{4\pi\varepsilon_0} \left[\frac{\mu_i \cdot \mu_j}{r_{ij}^3} - \frac{3(\mu_i \cdot r_{ij})(\mu_j \cdot r_{ij})}{r_{ij}^5} \right] s_{ij} \tag{3.2}$$

where ε_0 is the permitivity of free space, μ_i and μ_j are the dipole moment vectors of sites i and j, r_{ij} is the distance vector magnitude between sites i and j. s_{ij} is the 'switching' function acting between the switching radius r_s, and cutoff radius r_c:

$$s_{ij} = \begin{cases} 1, & \text{if } r_{ij} \leq 0 \\ \frac{(r_c - r_{ij})^2 (r_c + 2r_{ij} - 3r_s)}{(r_c - r_s)^3}, & \text{if } r_s \leq r_{ij} < r_c \end{cases}$$

hence, the total interaction energy (the LJ and dipole) between particles can be written as:

$$U_{ij} = U_{ij}^{LJ} + U_{ij}^{\mu\mu} \tag{3.4}$$

where U_{ij}^{LJ} and $U_{ij}^{\mu\mu}$ are equations 3.1 and 3.2 respectively. Interactions between the coulombic charge and the dipoles are modelled via the equation:

$$U_{ij}^{Q\mu} = \frac{Q_i}{4\pi\varepsilon_0 r_{ij}^3} \left[1 - 3\left(\frac{r_{ij}}{r_c}\right)^{2} + 2\left(\frac{r_{ij}}{r_c}\right)^{3} \right] \mu_j \cdot \mathbf{r}_{ij} \tag{3.5}$$

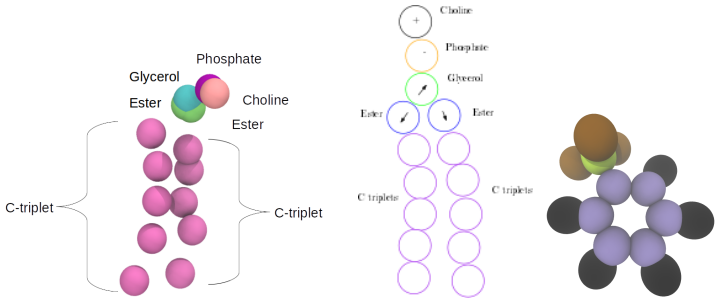

(a) (b) (c)

Fig. 3.1 Schematic of the DPPC molecule and the toluene molecule, shown in (a) and (b) respectively. The DPPC molecule is composed of CG beads, while the toluene molecule is built from the AA GAFF forcefield [114].

where **r** is the distance vector between dipole and monopole, r is the magnitude of the distance vector, Q_i is the charge of the atomistic particle, and **p** is the dipole vector of the CG bead. where ε_0 is the permitivity of space, $\mathbf{r}_{ij}$ is the interparticle distance vector, r_{ij} is the magnitude of $\mathbf{r}_{ij}$ and r_c is the cutoff radius. Weighting coefficients for the LJ and coulombic interaction parameters are briefly described here. The scaling parameter for the AA-CG LJ interaction C_{LJ} is implemented through the *shifted-force* potential:

$$E_{VdW} = 4C_{LJ}\varepsilon\left(\left[\frac{\sigma^{12}}{r^{12}} - \frac{\sigma^{6}}{r^{6}}\right] + \left[6\frac{\sigma^{12}}{r^{12}} - 3\frac{\sigma^{6}}{r^{6}}\right] - \left[7\frac{\sigma^{12}}{r^{12}} - 4\frac{\sigma^{6}}{r^{6}}\right]\right) \tag{3.6}$$

When modelling the test molecules, the toluene molecule was constructed via the GAFF amber forcefield, using the *ambertools* and *antechamber* programs [116]. The scaling parameter used for the AA-CG LJ interactions (equations 3.1 and 3.5) was used to model the interaction between the CG components of the lipids to the AA-components of the toluene and the lipid molecules.

3.3 Simulation Parameters

Each bilayer system was initally run on an *NVT* run with the Langevin thermostat for 100 ns. A production simulation run with the Berendson barostat and Langevin thermostat (i.e.

a *NPT* equivalent) for 1 μs to ensure that the system has been equilibrated, in addition to simulating a zero-surface tension (γ) simulation. The ELBA-CG-AA hybrid model offers an intriguing possibility of new insights, with AA-level detail coupled with CG-level simulation scales. The compatibility of it's CG-FF with the wealth of forcefields available for example, the AMBER14/GAFF forcefield, makes it a promising target for further studies with molecules without having to parameterise new forcefield models. The rRESPA (reversible-**Re**ference **S**ystem **P**rogator **A**lgorithm) was used to divide the total timestep to compute the AA and CG components on a different timescales. Outer level timesteps updated the CG-CG interactions (i.e. between the ELBA-beads) while the AA-CG and AA-AA interaction were updated in the inner level. Figure 3.1 shows the schematic of the DPPC molecule used for this simulation.

3.3.1 Free Energy Calculations

Umbrella Sampling

For the US simulations, the reaction coordinate was divided in 1.0 Å intervals from the center of the bilayer to the headgroup region of the leaflet. The bias potential for each umbrella window was set to 2.5 kcal mol^{-1}, increased to 5.0 kcal mol^{-1} for 2 Å above and below the headgroup region in the z coordinate (this follows closely the US procedure followed by Genheden *et al* [115]). The benchmarking US simulation for the toluene molecule was also undertaken under similar conditions - the toluene was tethered at 1 intervals apart ranging from 0 Å(bilayer centre) to 30 Å(above the headgroup region). In total, 30 umbrella windows were equilibrated with an initial run of 10 ns, and production runs for toluene coordinates for *weighted histogram analysis method* (WHAM) [25, 28, 117] analysis were run for 30 ns for each bin.

The Weighted Histogram Analysis Method - WHAM

Here, we give a brief description of US and *weighted histogram analysis method* (WHAM) method, which is used to unbias the discrete sampling potentials across the reaction coordinate. From this, we can express the unbiased free energy change as a function of the biased distribution:

$$G(\xi) = -k_B T \ln P'(\xi) - w_i(\xi) + F_i \tag{3.7}$$

where $G(\xi)$ represents the true free energy (Gibbs), $P'(\xi)$ represents the biased probability distribution of coordinates, from the implementation of the harmonic biasing potential, $w_i(\xi)$ represents the umbrella potential we implement along the reaction coordinate to ensure the solute samples the right coordinate space, and F is a undetermined constant (or free energy constant), used for combining the umbrella simulations together to produce the final free energy profile. $U'(\xi)$ is represented in this case by Hooke's Law potential - i.e. a harmonic biasing potential, which is implemented at every along the z coordinate, ranging from the center of the bilayer to the aqueous phase.

The WHAM equations seek to recombine the biased potentials through the following iterative equations to establish the best estimate of the $P(\xi)$; the unbiased probability distribution is initially computed through the equation:

$$P(\xi) = \frac{\sum_{i=1}^{N_{\text{windows}}} n_i(\xi)}{\sum_{i=1}^{N_{\text{windows}}} N_i \exp\left(F_i - U_{\text{bias},i}(\xi)/k_B T\right)} \tag{3.8}$$

where N_{windows} refers to the total number of bins used to divide the reaction coordinate (for a total of 30 simulations along a path of length 30 Å), U_{bias} represents the biased spring potential at each bin, and $P(\xi)$ represents the unbiased probability distribution. With an initial guess of the values used to combine the histograms at each bin, we approximate a better estimate of the P(ξ). Here, as we are looking at the translocation of the toluene

molecule through the bilayer, we can write ξ as z - hence, this approximated $P(z)$ is then combined with the following equation to estimate a better F_i value: :

$$F_i = -k_B T \ln \left[\sum_{\text{windows}} P(z) \exp\left[-U_{\text{bias},i}(z)/k_B T\right] \right] \tag{3.9}$$

where i represents the index of bins representing each umbrella bin. This iterative process is repeated until no change is detected in the *P(z)* and *F* values - i.e. when the iterations become self-consistent. As we want to compare the accuracy *and* efficiency of the US and JE-SMD method, we can estimate the approximate time taken for the PMF of the US to converge; if each umbrella bin along the reaction coordinate is run for 30 ns, then we can approximate that over 30 bins, that the total simulation time required for a well-sampled free energy profile is 900 ns, which will be used as the benchmark to compare the total simulation time required compared with the JE-SMD methods.

Jarzynski Equality

The Jarzynski equality (JE) is defined as:

$$e^{-\beta \Delta G(z)} = \langle e^{-\beta W(z)} \rangle \tag{3.10}$$

where β is the Boltzmann factor, ΔG(z) the free energy at the given z coordinate, and W is the work. What is intriguing with this equality is that W is a path-dependent property, whereas ΔG is a state function - an equilibrium property. Hence, this value equates a non-equilibrium property to a equilibrium property. Inherent issues regarding the practical use of JE is the inherent *bias* related to insufficient sampling and the magnitude of the average dissipated work. A direct interpretation of the JE to map a free energy profile can be

interpreted from the following equation:

$$\Delta G_{\mathrm{J}} = \frac{1}{\beta} \ln \left[\frac{1}{N} \sum_{i}^{N} e^{\beta W_i(z)} \right] \tag{3.11}$$

Where N is number of work profiles along the reaction coordinate to average over. However, as the use of the JE for free energy calculations may suffer from a significant amount of bias (i.e. the difference between the expected value of the free energy and its estimate, ΔG - ΔG_{J}) due to the insufficient sampling along the reaction coordinate. The second order cumulant expansion term for the JE was used to correct this bias due to this sampling problem [108]:

$$\Delta G_{\mathrm{cumulant}} = \langle W(z) \rangle - \frac{N}{N-1} \frac{\beta}{2} (\langle W(z)^2 \rangle - \langle W(z) \rangle^2) \tag{3.12}$$

where the $(\langle W(z)^2 \rangle - \langle W(z) \rangle^2)$ term is the variance of the work along the reaction coordinate (where the angular brackets represent the averaged value over N trajectories), and the $\langle W(z) \rangle$ term is the averaged work - this modified JE term for the free energy difference is valid on the condition that the work distribution along the reaction coordinate is *Gaussian*, as this enables the elimination of cumulants higher than that of second order of the JE to equal 0. When using this estimator to compute the free energy, another factor to consider is the distribution of the dissipation work, where the dissipated work is defined as the difference between the averaged work and the true free energy difference at the reaction coordinate - the magnitude of the dissipated work dictates the width of the Gaussian probability distribution. The dissipation work may be estimated by:

$$W(z)_{\mathrm{dissipation}} = \frac{1}{2} \beta \sigma^2_{W(z)} \tag{3.13}$$

where $\sigma^2_{W(z)}$ represents the variance of the work. The probability of observing a trajectory with negative dissipation work [118] can be described as:

$$P(W(z)_{\text{dissipation}} < 0) = \frac{1}{2}[1 - \text{erf}(\sqrt{\langle W(z)_{\text{dissipation}}\rangle/2})] \tag{3.14}$$

where $\langle \text{W(z)}_{\text{dissipation}} \rangle$ represents the averaged dissipation work along the trajectory. The equation implies that with a larger $\text{W}_{\text{dissipation}}$, the probability of observing a negative dissipation work event sharply decreases. Hence, an increased magnitude of dissipated work corresponds to a lower probability of observing negative work events, and is undesired. An alternate method for taking into account the bias of insufficient sampling was suggested by Gore *et al* [118] proposed correction to reduce the sampling bias. The JE sampling bias is defined as:

$$B_J = \frac{\langle W(z)_{\text{dissipation}}\rangle}{N^{\alpha_b}} \tag{3.15}$$

where $\alpha_b = \frac{\ln[\beta C_b \langle W_{\text{dissipation}}\rangle]}{\ln[C_b(e^{2\beta\langle W_{\text{dissipation}}\rangle}-1)]}$, and C_b is a fitted parameter that determines the boundary of the small N - large N regime. We have utilized C_b = 15, as tested by Gore [118]. From this, we can estimate a bias-corrected Jarzynski estimator:

$$\Delta G_{\text{bias}} = \Delta G_{\text{J}} - B_J \tag{3.16}$$

When computing average work along the reaction coordinate, we followed a block-averaging procedure, where every value in an Å interval along the reaction coordinate was binned and averaged, and the variance within each bin was sampled using the mean value of each bin. We computed several terms to assess the validity of the JE for the elucidation for an accurate free energy profile. We computed the ΔG_{J} term, $\Delta G_{\text{cumulant}}$, ΔG_{bias}, and the σ^2_w. The simulation procedure to compute the work distribution across the reaction coordinate was implemented as follows; after 1 μs of equilibration, the toluene molecule was inserted and held at 30 from the bilayer normal. The system was further equilibrated for 1 ns to ensure

that the bilayer remained unaffected by the toluene molecule at that distance. For the SMD method, four velocities were assigned - at *constant velocities* of 8×10^{-6} fs^{-1} (*faster*), 5×10^{-6} fs^{-1} (*fast*), and 8×10^{-7} fs^{-1} (*slow*) and 5×10^{-7} fs^{-1} (*slower*). These velocities have been checked with previous studies and deliberately slowed to systematically analyse the effect of velocity - for example, Schulten *et al* used velocities of 0.1 Å ns^{-1} (0.0001 Å fs^{-1}) , 10 Å ns^{-1} (0.01 Å fs^{-1}), 100 Å ns^{-1} (0.1 Å fs^{-1}) when validating the JE-SMD method through stretching deca-alanine simulations [108]. In other examples, Kucuyak *et al* [110, 111] used velocites ranging from 1.25 to 10 Å ns^{-1} (Hence, 1.25×10^{-6} Å fs^{-1} to 10.0×10^{-6} Å fs^{-1}), which are directly comparable to the velocities used with our simulations. Given this, we can conclude that the velocities we have chosen are reasonable to test the JE-SMD method. The 'faster' and 'fast' velocities can be defined as the 'fast-growth' regime, while '*slow*' and '*slower*' velocities can be recognised as the 'slow-growth' regime. The biasing potential (Hooks potential) to anchor the toluene molecule to the reaction coordinate used a force constant of 25 kcal mol^{-1}. The work values were collated over 20 repetitions of the pulling simulation. To analyse the effect of using increased sampling blocks, we measured the ΔG_{J}, $\Delta G_{\mathrm{cumulant}}$, ΔG_{bias} terms and the σ_w^2 term over of N = 10, 15 and 20 simulation runs.

3.3.2 Measuring the Convergence at increments of the Potential Energy Surface

To gain a practical measure of the sampling environment through the reaction coordinate (i.e. the bilayer normal), we have measured the pairwise interaction forces between the toluene and the lipid environment - specifically, we divided the interaction between the headgroup and tailgroup interactions, as these have distinct anisotropies and chemical moieties. By analysing the difference between the interaction forces observed between the JE-SMD velocities and the US snapshots, we can get an indication of the effect of velocity

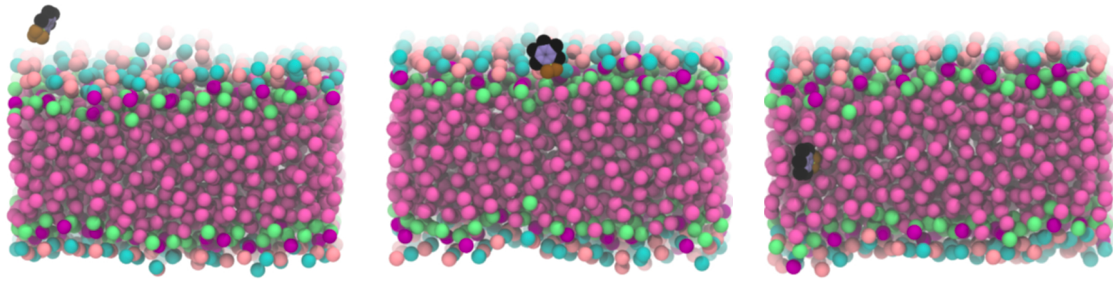

(a) (b) (c)

Fig. 3.2 Trajectory snapshots for the JE-SMD/US simulations for the toluene/DPPC.

upon the sampling of the intermolecular forces - whether it diverges or converges towards the US sample with a slower velocity.

Index	Method	Solute Type	N	v (Å fs^{-1})	k (kcal mol^{-1} Å)	t (ns)
1	JE-SMD	toluene	20	8 x 10^{-6}	25	100
2	JE-SMD	toluene	20	5 x 10^{-6}	25	120
3	JE-SMD	toluene	20	8 x 10^{-7}	25	720
4	JE-SMD	toluene	20	5 x 10^{-7}	25	1200
5	US	toluene	30	-	25/50	900

Table 3.1 List of simulations run in this study - including all velocities of the JE-SMD simulations, and the US simulations used as the benchmark/control to compare against. v represents the velocity of the JE-SMD simulations, k represents the spring constant used for restraining the toluene molecule to the reaction coordinate, while t represents the total simulations time required.

3.4 Results

3.4.1 Toluene Simulations - JE-SMD/US comparison

Table 3.2 shows the collated data and growth regions for each velocity of the JE-SMD implementation. The benchmark US simulation (Figure 3.10(a)) shows free energy change of -5.5 kcal mol^{-1} (corresponding to 23.012 kJ mol^{-1}, which is comparable to the BERGER

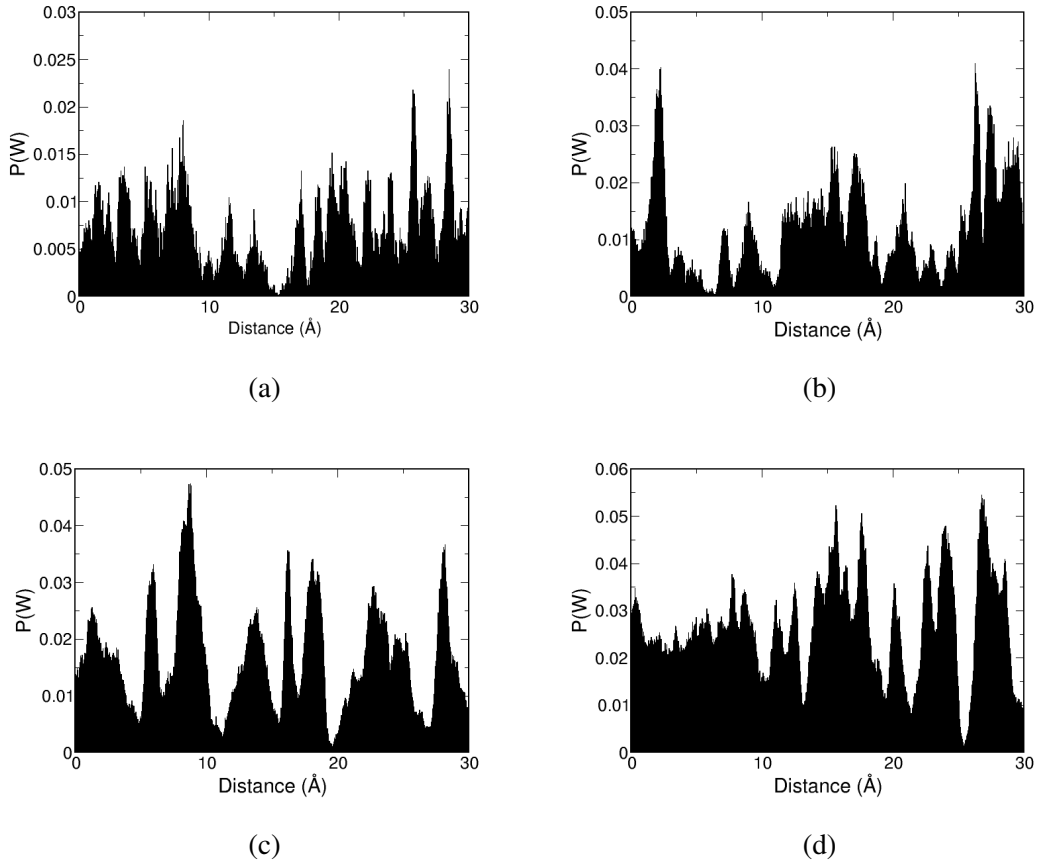

Fig. 3.3 Probability distribution of the work (W(z)) along the reaction coordinate of the toluene for the JE-SMD simulations, where (a), (b), (c) and (d) show the work distributions for the v = 8×10^{-6} fs^{-1}, 5×10^{-6} fs^{-1}, 8×10^{-7} fs^{-1} and 5×10^{-7} fs^{-1} (corresponding to the *faster*, *fast*, *slow* and *slower* velocities respectively).

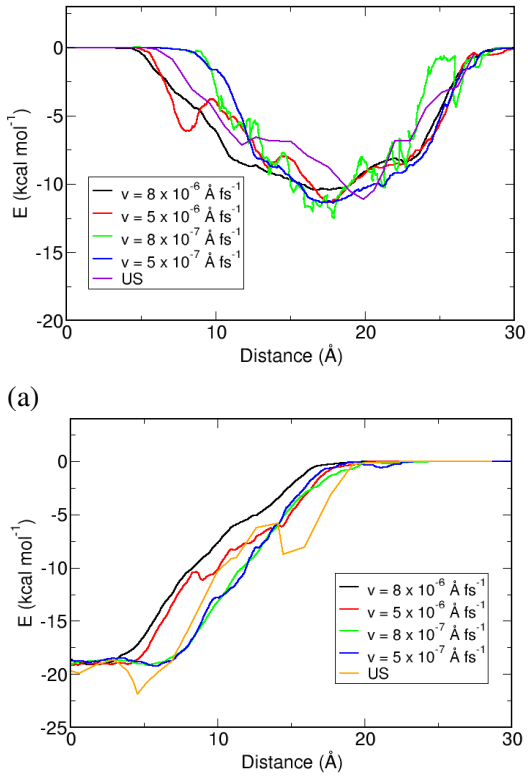

Fig. 3.4 The total interaction energy between the toluene and the DPPC headgroups (phosphate, glycerol, choline) and the DPPC tailgroups (C-triplets) shown in (a) and (b) respectively. The force interaction was measured for each velocity of the JE-SMD simulations and the equivalent US simulations.

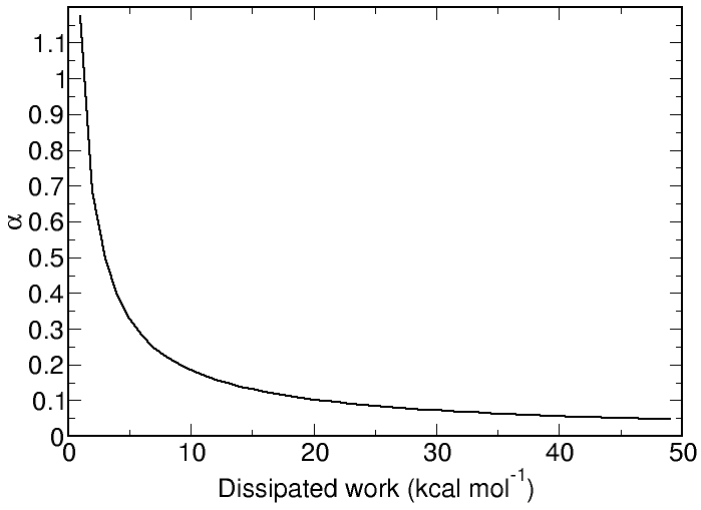

Fig. 3.5 The plot for $\alpha_b = \frac{\ln[\beta C_b \langle W(z)_{\text{dissipation}} \rangle]}{\ln[C_b(e^{2\beta \langle W(z)_{\text{dissipation}} \rangle} - 1)]}$, for dissipation work between 0 - 50 kcal mol^{-1}. Interpreting the $\frac{\beta}{2}\sigma_w^2$ as the dissipation work, the α_b was selected when computing the $\Delta G(z)_{\text{bias}}$ from the JE-SMD simulations

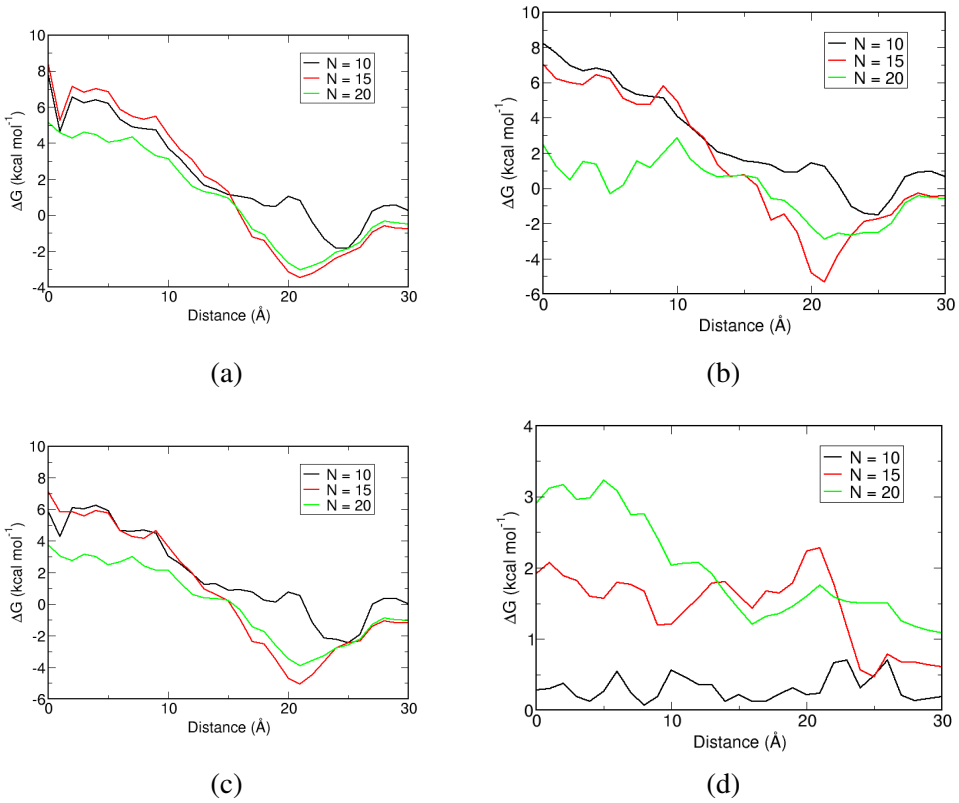

Fig. 3.6 The free energy profiles computed from the v = 8 $\times$ 10^{-6} fs^{-1} (*faster*) JE-SMD simulations. (a) shows the ΔG_{J}, (b) shows the $\Delta G_{\mathrm{cumulant}}$, (c) shows the ΔG_{bias} while (d) shows the $\langle W(z)^2 \rangle - \langle W(z) \rangle^2$ respectively. The convergence of JE-SMD simulation profiles was shown from N = 10, 15 and 20 simulations respectively.

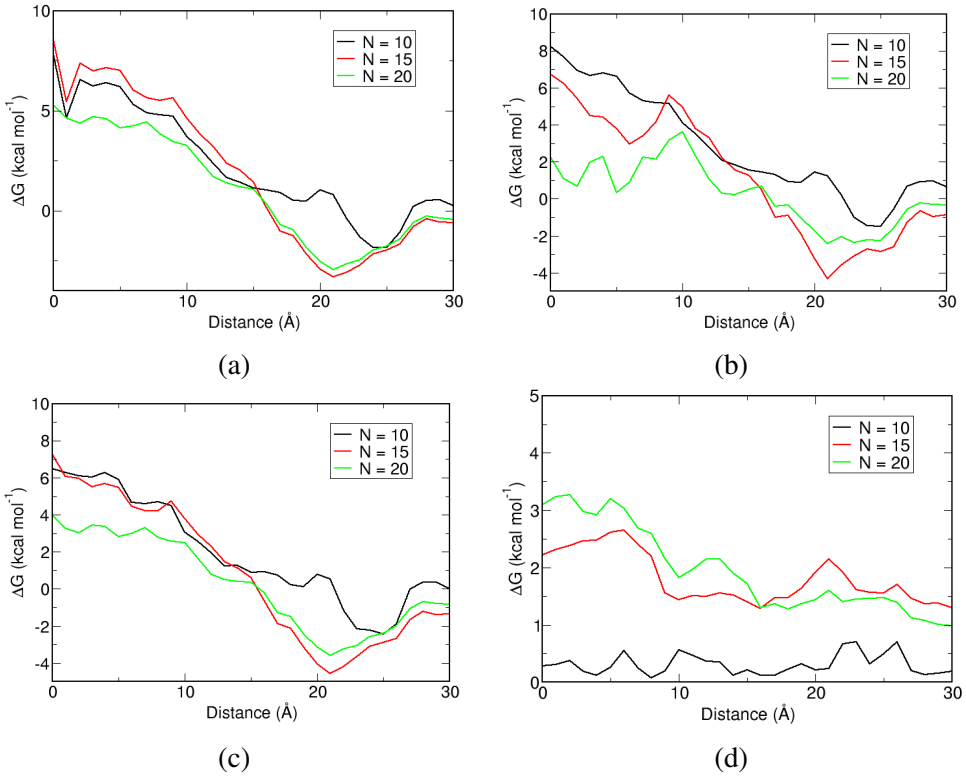

Fig. 3.7 The free energy profiles computed from the v = 5 $\times$ 10^{-6} fs^{-1} (*fast*) JE-SMD simulations. (a) shows the ΔG_{J}, (b) shows the $\Delta G_{\mathrm{cumulant}}$, (c) shows the ΔG_{bias} while (d) shows the $\langle W(z)^2\rangle - \langle W(z)\rangle^2$ respectively. The convergence of JE-SMD simulation profiles was shown from N = 10, 15 and 20 simulations respectively.

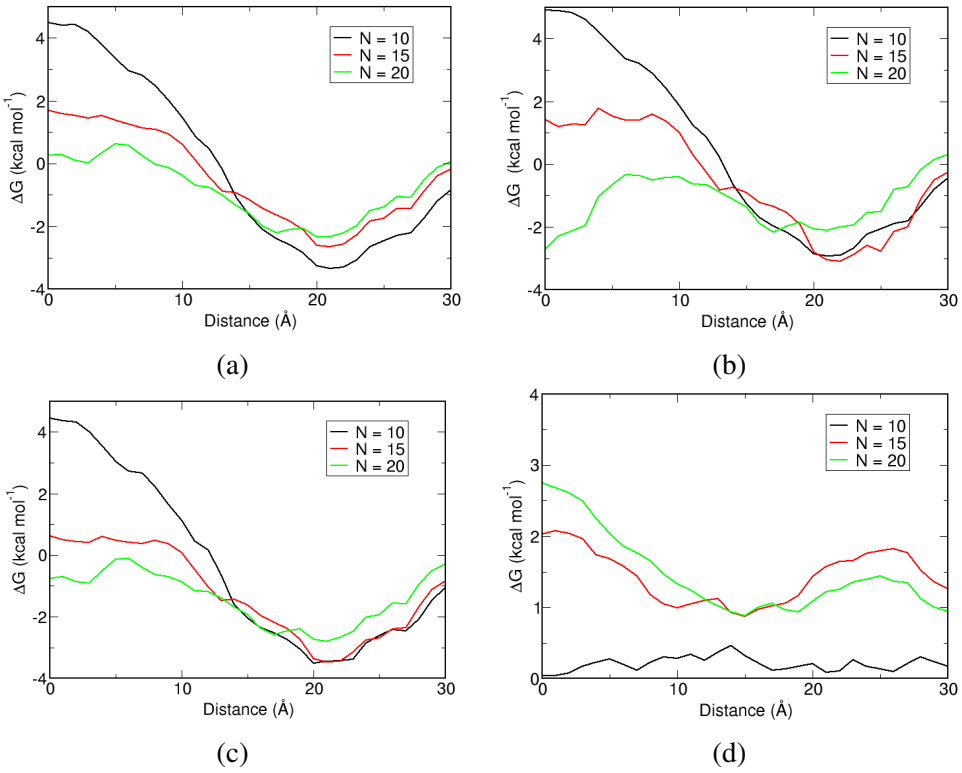

Fig. 3.8 The free energy profiles computed from the v = 8 $\times$ 10^{-7} fs^{-1} (*slow*) JE-SMD simulations. (a) shows the ΔG_{J}, (b) shows the $\Delta G_{\mathrm{cumulant}}$, (c) shows the ΔG_{bias} while (d) shows the $\langle W(z)^2\rangle - \langle W(z)\rangle^2$ respectively. The convergence of JE-SMD simulation profiles was shown from N = 10, 15 and 20 simulations respectively.

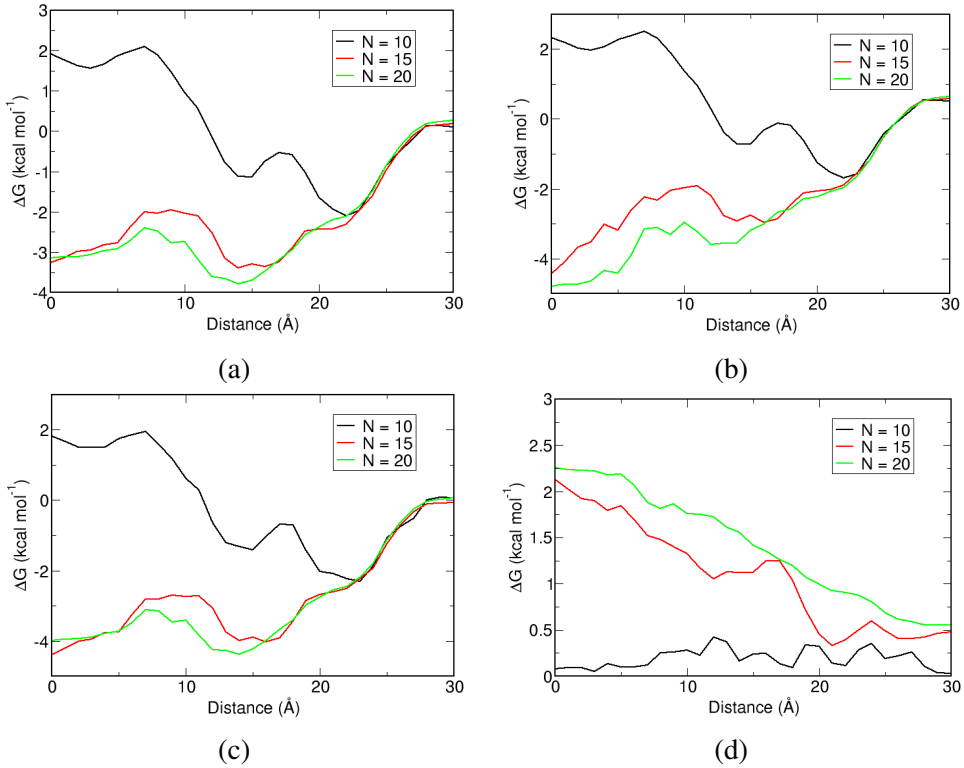

Fig. 3.9 The free energy profiles computed from the v = 5 $\times$ 10^{-7} fs^{-1} (*slower*) JE-SMD simulations. (a) shows the ΔG_{J}, (b) shows the $\Delta G_{\mathrm{cumulant}}$, (c) shows the ΔG_{bias} while (d) shows the $\langle W(z)^2\rangle - \langle W(z)\rangle^2$ respectively. The convergence of JE-SMD simulation profiles was shown from N = 10, 15 and 20 simulations respectively.

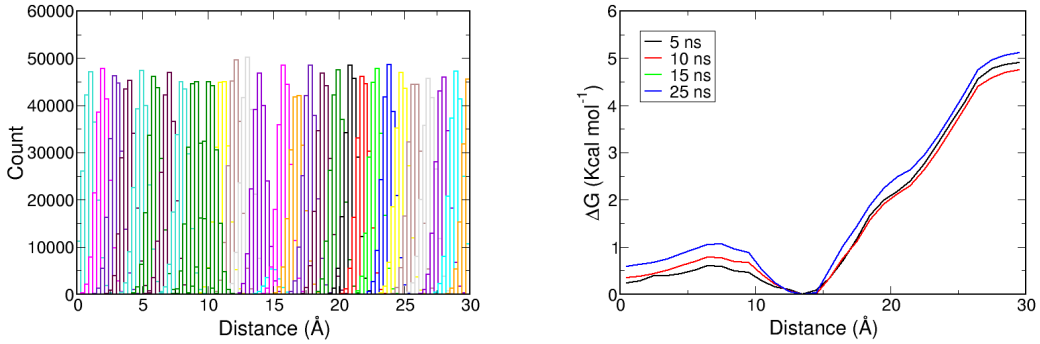

Fig. 3.10 The free energy profile extracted from the series of US simulations for the toluene molecule. (a) shows the probability distribution overlap between the constrained simulations along the reaction coordinate, while (b) shows the free energy profile convergence over 30 ns, illustrating the convergence profiles at 5, 10, 15 and 25 ns. From the overlap between the 15 and 25 ns, we can conclude that the US profile as converged.

AA and MARTINI CG forcefield values (-12.5 - -20.92 kJ mol^{-1}) [119–121]. Here, the key features to compare with the JE-SMD results is the energy trough near trough near z = 15 Å, and the quantitative consistency with the change. Figures 3.9, 3.8, 3.7, 3.6 shows the ΔG_{J}, $\Delta G_{\mathrm{cumulant}}$, ΔG_{bias} and $\langle W(z)^2\rangle - \langle W(z)\rangle^2$ for each velocity of the JE-SMD simulations. Figure 3.5 shows the α_b plot used for computing the ΔG_{bias} values. Each JE-SMD plot was shown as to show to convergence with averaging over larger numbers of SMD simulations. For the v = 8 $\times$ 10^{-7} fs^{-1} (faster) simulations, we see an overall change of 4 - 8 kcal mol^{-1}, 2 - 8 kcal mol^{-1} and 4 - 7 kcal mol^{-1} for the ΔG_{J}, $\Delta G_{\mathrm{cumulant}}$ and ΔG_{bias} values respectively. The $\langle W(z)^2\rangle - \langle W(z)\rangle^2$ show values of 0.2 - 3 kcal mol^{-1}. Similar results are seen with the v = 5 $\times$ 10^{-7} fs^{-1} ($faster$) simulations, which show very similar patterns with increasing N simulations - it is clear that the JE-SMD simulations in the 'fast-growth' regime ($faster$ and $fast$ velocities), none of the JE interpretations reproduce the US results effectively, and that there is minimal effect on the free energy profile upon increasing the N number of simulations.

Interpreting the 'slow-growth' regime simulations, the v = 8 $\times$ 10^{-7} fs^{-1} JE-SMD simulations, we see a overall improvement in the PMF profiles - we see an overall change of 0 - 4 kcal mol^{-1}, -2.5 - 5 kcal mol^{-1} and -1 -4.5 kcal mol^{-1} for the ΔG_{J}, $\Delta G_{\mathrm{cumulant}}$ and ΔG_{bias}, while we see a range of 0 - 2.8 kcal mol^{-1} for the $\langle W(z)^2\rangle - \langle W(z)\rangle^2$ values. There is a clear emergence of features of the free energy profile between 0 - 7.5 Å with the $\Delta G_{\mathrm{cumulant}}$ and ΔG_{bias}, which represents a marginal improvement. We observe a significant improvement in the feature representation in the free energy profile with increasing sampling. As the range of $\langle W(z)^2\rangle - \langle W(z)\rangle^2$ is not significantly different from the 'fast-growth' regime, it is apparent that it is the insufficient sampling of the phase space is the reason for the discrepancy from the US results. For the *slower* regime, at velocities of v = 5 $\times$ 10^{-7} fs^{-1}, we see the closest consistency with the US profile - at N = 10 simulations, there are still

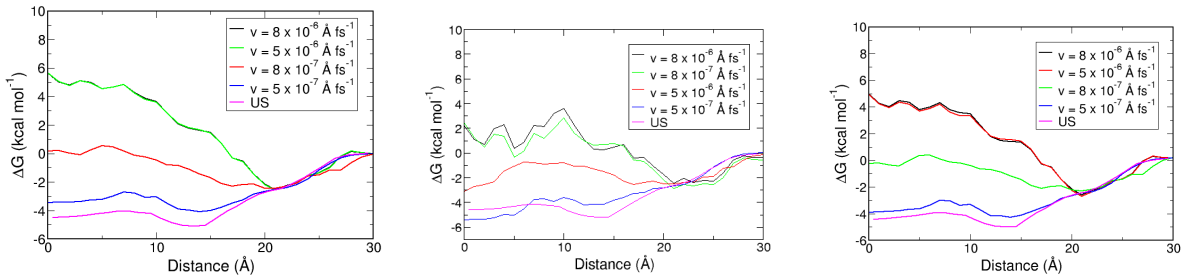

(a) (b) (c)

Fig. 3.11 The collated free energy profile JE-SMD simulations, as shown by the v = 8 $\times$ 10^{-6} fs^{-1}, 5 $\times$ 10^{-6} fs^{-1}, 8 $\times$ 10^{-7} fs^{-1}, 5 $\times$ 10^{-7} fs^{-1} (corresponding to the *faster*, *fast*, *slow*, and *slower* velocities respectively) JE-SMD simulations, with the US result as the benchmark profile. (a) shows the ΔG_{J} interpretation, (b) shows the $\Delta G_{\mathrm{cumulant}}$ interpretation, and (c) shows the ΔG_{bias} interpretations of the JE respectively. Each JE-SMD simulation profile was taken from averaged values from N = 20 simulations.

clear convergence issues of the free energy profile, as we observe a free energy change of approximately 2.0 kcal mol^{-1} - however, even within these profiles, we see the key features that are consistent with the US profile - the trough at 10 - 20 Å and 0 - 7 Å. This problem is reduced by averaging over larger number of samples (N = 15, 20), where we see a overall free energy change of -4.0 kcal mol^{-1} for the ΔG_{J}, $\Delta G_{\mathrm{cumulant}}$ and ΔG_{bias} profiles. Here, it is clear that the ΔG_{J} and ΔG_{bias} shows the clearest consistency with the US results, while the $\Delta G_{\mathrm{cumulant}}$ profile slightly overcorrects the free energy region near the 0 - 7 Å region.

3.5 Discussion

From the work distributions along the reaction coordinate of the reaction coordinate (Figure 3.3), we have shown that the distribution follows a series of Gaussian-like profiles, which would seem to the condition for which the cumulant approximation of the JE-SMD method be applicable. In the JE-SMD validation by Schulten [108], they reported the dissipation work to be between 1.9 to 4.3 kcal mol^{-1} (3.1 k_BT - 7.1 k_BT) - where a smaller estimate corresponded to a PMF profile that was closer in convergence with the corresponding US example. With our toluene simulations, we observe dissipation work values in the range of

FE Method	v (Å fs^{-1})	ΔG (kcal mol^{-1})	B_J	α_b	type
ΔG_J	8×10^{-6}	5.0	2.5	0.5	fast-growth
ΔG_J	5×10^{-6}	5.0	2.5	0.5	fast-growth
ΔG_J	8×10^{-7}	0.1	2.5	0.5	slow-growth
ΔG_J	5×10^{-7}	-3.0	2.5	0.5	slow-growth
$\Delta G_{cumulant}$	8×10^{-6}	2.0	2.5	0.5	fast-growth
$\Delta G_{cumulant}$	5×10^{-6}	2.0	2.5	0.5	fast-growth
$\Delta G_{cumulant}$	8×10^{-7}	-2.5	2.5	0.5	slow-growth
$\Delta G_{cumulant}$	5×10^{-7}	-4.5	2.5	0.5	slow-growth
ΔG_{bias}	8×10^{-6}	4.0	2.5	0.5	fast-growth
ΔG_{bias}	5×10^{-6}	4.0	2.5	0.5	fast-growth
ΔG_{bias}	8×10^{-7}	-0.9	2.5	0.5	slow-growth
ΔG_{bias}	5×10^{-7}	-4.0	2.5	0.5	slow-growth
US	-	-4.5	-	-	-

Table 3.2 Data for the overall change in ΔG for each JE-SMD simulation, with the bias (B_J) and fitted parameter (α_b) utilised to compute ΔG_{bias} at each velocity respectively.

0 - 3 kcal mol^{-1}, which indicates that we are working within a quasi-equilibrium region in each JE-SMD profiles. Other bilayer comparison studies of the JE-SMD and US methods by Kuyucak *et al* [110, 111], even a small inclusion of coulombic interactions can affect efficient sampling with both fast and slow simulations. Previous work by Warshel *et al* [122] has shown in protein ligand binding studies the problems regarding the high convergence time of electrostatic interactions, showing that the convergence of a simple gramacidin A channel takes of the order of μs. In our example, the toluene molecule was explicitly chosen as a non-ionic, hydrophobic molecule which would circumvent the sampling issues related to the coulombic potentials.

The final comparison between the JE-SMD and US results are indicated in Figure 3.11, which indicates a significant sampling problem in the JE-SMD simulations at velocities of v = 8×10^{-6} Å fs^{-1}, 5×10^{-6} Å fs^{-1} and 8×10^{-7} Å fs^{-1}, which correspond to the '*faster*', '*fast*' and '*slow*' simulations respectively; in the '*faster*' and 'fast' case, the regions of 0 - 20 Å fails to capture the overall shape or magnitude entirely, while for the 'slow' case,

the region of 23 - 30 Å, the shape has relatively converged, and while we do see an overall lowering of the PMF in the region of 0 - 20 Å, it still fails to capture essential properties of the US simulation such as the trough in the 10 - 15 Å region of the reaction coordinate. It is only with the 5×10^{-7} Å fs^{-1} (‘*slower*’) JE-SMD samples that we see a pattern of consistency with the US result - the overall change of -6 kcal mol^{-1} is comparable to the -4.4 kcal mol^{-1} we see with the US result, and although sampling issues remain, as indicated by the shallow trough present in the 10 - 15 Å region, it is clear that it follows the shape of the US free energy profile. The trend we seem to see with a JE-SMD simulation is that with a *slower* velocity (i.e. being closer to the equilibrium regime), the free energy profile for the JE-SMD shows marginal improvements in its profile, and the magnitude of change becomes smaller (i.e. approaches the US). In conclusion, Schulten *et al* [108] has commented that the JE is valid for processes at any speed, and while this may be true in theory, even at velocities where it becomes practical compared to the US method, the bias due to the under sampling of rare-trajectories makes the JE-SMD method impractical to use unless when used for the simplest systems.

3.6 Conclusion

We have used a sample toluene/bilayer system to establish the validity of JE-SMD method with the US method; we have divided the JE-SMD experiments into two regimes of velocities - a ‘fast-switching’ regime where the total number of simulations are computational more efficient compared to the US method, and a ‘slow-switching’ regime where total simulation time is comparable or exceeds the total simulation time in sum of the US sampling bins. The PMF profile from the US simulations confirmed that the FF model we have used with this simulation can be trusted to produce consistent PMF data with known literature,

and hence is valid to use as a benchmark to compare the JE-SMD simulations.

To measure the efficiency and accuracy of the JE-SMD method to one that is comparable to the US method, we implemented three interpretations of the JE - the raw JE interpreter, ΔG_J, the cumulant second-order interpreter $\Delta G_{cumulant}$ which corrects the sampling bias, and ΔG_{bias}, which is an alternate method for taking into account high sampling bias. Within the scope of a simple bilayer/toluene simulation, we failed to see a convergence towards US results in the 'fast-switching' regime, with all interpretations of the JE-SMD, while in the 'slow-switching' regime, results varied; while we observed significant improvements in terms of the appearance of peaks and troughs in the free energy profile, the JE-SMD did not fully converge towards the US result at even the slowest velocities, and each bias corrected interpretations of the JE-SMD did not significantly alleviate the sampling problem. From looking at step-wise convergence (adding a set number of simulations for the JE-SMD interpreters), we saw significant improvements in the quantitative profile of the free energy profile in the 'slow-switching' regime, while at 'fast-switching' regimes, this had marginal effects.

Hence, based on the evidence from this study, it is clear that the primary factor in improving the JE-SMD profile its vicinity to a quasi-equilibrium region - slower sampling allows for this, but at the rate which this energetic region is reached, the computational cost and number of simulations required becomes prohibitive, and hence, noncompetitive when compared to the US method - In the 'slow-switching' regime, we have already allocated a longer total simulation time compared to the US simulations, which again indicates that the the JE-SMD method needs modification if it is to be practically utilised. As this bilayer system was designed to be as simple as possible, it is clear that this sampling issue can only be exacerbated when implemented towards highly inhomogeneous reaction co-

ordinates where intermolecular forces of high convergence such as coulombic forces take prominence. Hence, while it is clear that the JE-SMD method provides a path towards an efficient alternative to free energy sampling, issues remain in its interpretation, and further work is required to correctly account for significant bias of the region. This result also calls into question many of the previous results that used velocities that are magnitudes higher than those used in this simulation study, and hence, calls for a comphrensive review.

CHAPTER 4

INTERACTION OF VARIABLE HYDROPHOBIC NANOPARTICLES WITH NON-IONIC BILAYERS

4.1 Abstract

The mechanism of transit of a nanoparticle (NP) through a biomimetic bilayer is highly dependent on the composition and property of the NP. Here, we analyse three key properties of a NP - the effect of size, hydrophobicity and the PMF change upon the reaction coordinate where the NP translocates through the bilayer. Through a continuum model of a NP based on a Hamaker style model, we have created NP of tunable properties. The effect of hydrophilic, hydrophobic, and intermediate properties of the NP is analysed against a biomimetic bilayer - we show that this model can illustrate three distinct properties - where the hydrophilic type shows rupture of the bilayer, the hydrophobic type showing a entrapment of the NP around the hydrophobic tailgroups of the bilayer, and the intermediate type showing a distinct, direct translocation type mechanism. Increasing the NP size shows different effects for each type of NP, and hence, may provide insight into the design of NPs with these types of mechanisms involved.

4.2 Introduction

4.2.1 The Role of Biomimetic Vesicles in Simulations

The self-assembly of nanoparticles (NPs) and amphiphilic macromolecules offers a powerful route to generate functional soft materials with controllable structure and properties. At the most basic level, polymeric vesicles are liquid-containing sacs and have a compartmentalised enclosed volume shiel ded from the outside liquid environment by a bilayer commonly composed of amphiphilic molecules. The tendency of surfactants to aggregate into large vesicular structures allows polymeric amphiphiles to be used as a model to emulate properties of more complex biomembranes.

As a result, numerous studies with representations of complex bilayers have been attempted - biomembranes contain numerous heterogeneous components and factors such as the presence of membrane proteins, varying rigidity of the lipids and varying charge density near the headgroups, to name a few [123]. These factors control the curvature, diffusive properties and mechanisms of translocation through a bilayer. Given the need to allow selective permeation of molecular species, the additional mechanisms biolipid systems have evolved involve complex mechanisms which allow passive and active diffusion, controlled by a concentration gradient or an energy-input driven process respectively. Despite the complexity of the systems involved, recent successes in particle delivery, such as the development of inhalable insulin [124], amongst others, has highlighted the possibilities of NPs as novel agents in clinical applications. Difficulties remain, however, in determining which component-by-component interactions are responsible for phenomena ranging from the direct translocation of a NP to the rupture of the bilayer. Questions remain with regards to the mechanism of how foreign particles can interact near the bilayer interior - what properties imply the mechanism of transit? Passive translocation processes for example, do not require an external

energy input, which would dictate that the surface functionalization of the NP primarily dictates the mechanism of membrane translocation [125].

The purpose of this work is to provide an overview of the mechanism of transit of a NP with respect to it's surface composition. To address this challenge, we have investigated the mechanisms by which NPs of varying size and hydrophobicity interact with and cross biomimetic polymer membranes. To this end, we have simulated a polyoxyethylene-glycol (PEG-PEO) surfactant bilayer; this surfactant provides a large variety of phase transitions depending on the temperature, concentration and on structural properties, and computationally intensive coulombic potentials are not taken into account, which alleviates the MD computation. We have developed nonspecific model NP-bilayer systems which comprised a coarse-grained *poly(ethylene)6-block-poly(ethylene oxide)2* ($C_{12}E_2$) bilayer in water and a generic NP of 1.0, 1.5 or 2.0 nm radius (R) with hydrophilic, hydrophobic or intermediate character (Hence, nine different systems to analyse in total). Similar continuum style models, targeting the efficiency through the use of generic parameters have been studied before using DMD/LME simulations of hydrophilic models [126]. However, using similar continuum models to tune the hydrophobicity has not been attempted before. We show that by adjusting this continuum model of a NP, we can reproduce many of the properties of hydrophilic/hydrophobic NPs and also show that NPs of intermediate hydrophobicity can undergo a direct translocation.

From our simulations, we have identified three distinct, size-dependent mechanisms - where the hydrophilic NP forms a pore like deformation of varying sizes, depending on the radius of the NP. For the intermediate character type, we show that this NP models a direct penetration through the bilayer, with minimal disruption in the bilayer, coupled with a flattened free energy profile. With the hydrophobic NP type, we show that the hydrophobic groups within

the bilayer wraps around the NP to maximise the hydrophobic interactions its hydrophobic components.

4.3 Simulation Methodology

4.3.1 Coarse-grained Model

In this work, we use the Shinoda-DeVane-Klein (SDK) CG model [127, 128]. The model has been parameterized against thermodynamic properties (densities, interfacial tensions, transfer free energies) and has been applied successfully by itself or as a model to study a range of soft matter systems [12, 129, 130], and recently extended to include representations of amino acid residues and rigid molecules such as cholesterol. A brief description of their coarse-graining approach follows here - within this model 3-5 heavy atoms are represented by a single interaction site or "bead" (one water bead represents three water molecules). The system in this study consisted of a single NP, a non-ionic surfactant bilayer consisting of 2000 poly(oxyethylene) (denoted $C_{12}E_2$) surfactant molecules and 57312 water beads. The surfactant molecule was described using four CG bead types: OA (-CH_2OH) and EO (-CH_2OCH_2-) which represent the hydrophilic head group and CM (-$CH_2CH_2CH_2$-) and CT2 ($CH_3CH_2CH_2$-), which represent the hydrophobic tail groups. A schematic of the atomistic to CG mapping is given in Figure 4.1.

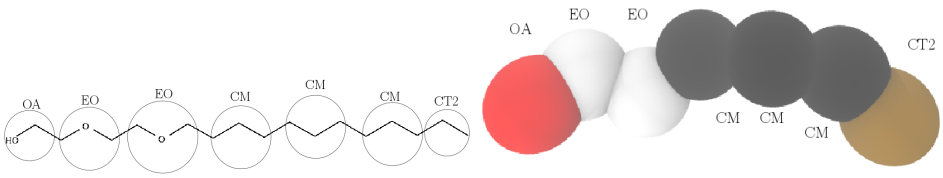

Fig. 4.1 Coarse-grained mapping of the surfactant $C_{12}E_2$ used in this study. The EO and OA groups constitute the hydrophilic headgroups, while the CM and CT2 beads represent the hydrophobic tailgroups.

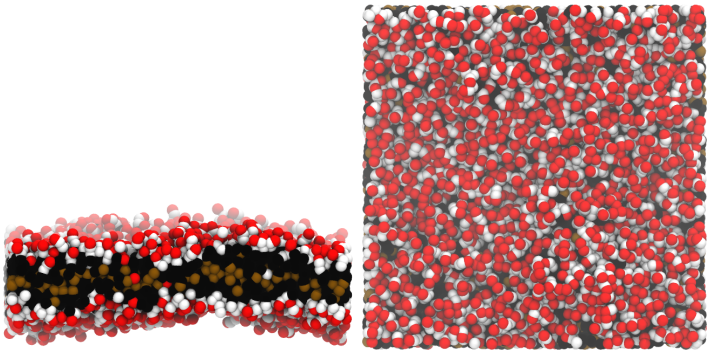

Fig. 4.2 The side and top views of the polymeric bilayer we will be using for this simulation. The dimensions of the expanded bilayer (a) are 16 × 16 nm^2, while the thickness of the bilayer is approximately 36 Å.

The non-bonded interactions between the surfactant molecules and between the surfactant molecules and water were described using the Lennard-Jones-like formulae

$$U_{LJ12-4}(r) = \frac{3\sqrt{3}\varepsilon}{2}\left[\left(\frac{\sigma}{r}\right)^{12} - \left(\frac{\sigma}{r}\right)^{4}\right] \tag{4.1a}$$

$$U_{LJ9-6}(r) = \frac{27\varepsilon}{4}\left[\left(\frac{\sigma}{r}\right)^{9} - \left(\frac{\sigma}{r}\right)^{6}\right] \tag{4.1b}$$

where ε is the well depth (the numerical factors in the prefactor are chosen such that the minimum value of the potential is $-\varepsilon$) and $U(\sigma) = 0$, following a standard Lennard-Jones model. The first (LJ_{12-4}) form is only used for interactions involving water (W) beads. The intra-molecular interactions were described using a molecular mechanics force field:

$$U_{\text{bond}} = k_\ell(\ell - \ell_0)^2 \tag{4.2a}$$

$$U_{\text{angle}} = k_\theta(\theta - \theta_0)^2 \tag{4.2b}$$

where k_ℓ and k_θ are the bond stretching and bending force constants and ℓ_0 and θ_0 are the equilibrium bond lengths and angles respectively. Parameters for both the bonded and non-bonded interactions are taken from parameters published by Shinoda *et al* [131] and are tabulated in Appendix 1 for completeness. Rather than explicitly model the NP as a rigid

collection of interaction sites, the particles are modelled as spheres composed of uniformly distributed interaction sites i.e. the particle was treated as a surface-to-molecule potential, which is the approach taken by Chiu *et al*, which itself is based upon Hamaker's model for modelling the non-bonding potential of surfaces [132, 133]. Using Hamaker's model allows us to concentrate on the bulk property of the NP rather than its individual constituents, and since we are primarily interested in the effect of the surface properties of the NP, it fits this study. To represent the hydrophilic and hydrophobic NPs, the interaction sites were taken to be of type W and CT2 respectively. The interactions between the NP and CG beads were derived from integrating the interaction potential between a CG bead and an interaction site within the NP over the particle's volume. Assuming that the interaction between a CG bead and single interaction site can be described through the modified LJ functions above (Equations 5.1a and 5.1b) the interaction between a NP and a CG bead may be written as:

$$U_{NP}^{12-4}(r,R) = \left(\frac{2\sqrt{3}\pi\rho\varepsilon\sigma^{12}R^3}{15}\right)\left(\frac{5R^6+45R^4r^2+63R^2r^4+15r^6}{(r^2-R^2)^9}\right) - \frac{3\pi\rho\varepsilon\sigma^4R}{r^2-R^2} + \frac{3\sqrt{3}\pi\rho\varepsilon\sigma^4}{2r}\ln\left[\frac{r-R}{r+R}\right] \tag{4.3a}$$

$$U_{NP}^{9-6}(r,R) = 9\pi\rho\varepsilon\sigma^9R^3\frac{3R^4+42R^2r^4+35r^4}{35r(r^2-R^2)^6} - \frac{9\pi\rho\varepsilon\sigma^6R^3}{r^2-R^2} \tag{4.3b}$$

where ρ is the density of the NP and R is the NP radius. The density of the NP was taken to be 1.0 kg m^{-3} (based on the density of water). Full derivations of these formulae are given in Appendix 1. The parameters ε and σ are the Van der Waals parameters for the W (hydrophilic) or CM (hydrophobic) CG beads. As well as purely hydrophilic and hydrophobic NPs we also consider a NP of intermediate hydrophobicity; in that case the interaction potential between the NP and solvent bead is taken as a simple interpolation of the hydrophilic

and hydrophobic potentials:

$$NP_{\text{property}} = \begin{cases} U_{NP}^{\text{hydrophile}}(r) = (x)U_{NP}^{\text{phile}}(r) + (1-x)U_{NP}^{\text{phobe}} & : x = 1 \\ U_{NP}^{\text{hydrophobe}}(r) = (x)U_{NP}^{\text{phile}}(r) + (1-x)U_{NP}^{\text{phobe}} & : x = 0 \\ U_{NP}^{\text{intermediate}}(r) = (x)U_{NP}^{\text{phile}}(r) + (1-x)U_{NP}^{\text{phobe}} & : x = 0.5 \end{cases}$$

where $0 \leq x \leq 1$. Plots of the interaction potentials of each NP are provided in Appendix A. Three R values were used for creating the NPs - $R = 1.0$, 1.5 and 2.0 nm. The 1.0 nm radius NP represents a NP that is comparable to the tailgroup (CM and CT2) length of the amphiphile, while the 2.0 nm radius NP represents a NP with a width that is comparable to the thickness of the bilayer. The schematic for each type of NP is shown in Figure 4.3.

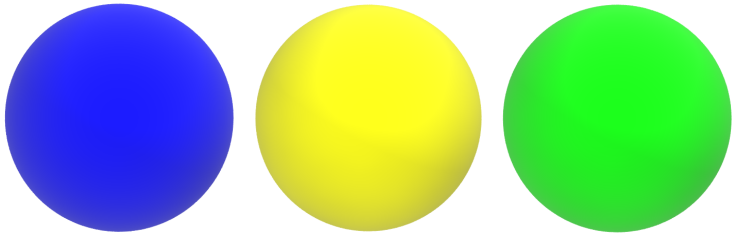

(a) hydrophile (b) hydrophobe (c) intermediate

Fig. 4.3 Color Schematic for each NP. For each NP type, we designed three radii (R) types, of R = 1.0, 1.5 and 2.0 nm.

Initial Configuration of the Bilayer

All simulations were performed using the LAMMPS molecular dynamics package [112]. To generate the initial configuration of the bilayer, 3500 CG-beads of the $C_{12}E_2$ were used to arrange a bilayer in a simulation box ranging from dimensions 80 Å $\times$ 80 Å $\times$ 200 Å with the rest of the box being filled with 14328 water beads. This system was equilibrated using a *NVT* ensemble for 1 ns simulation time with increasing timesteps to ensure the overlaps between molecules were resolved and to ensure the system did not fluctuate substantially.

To reduce the likelihood of finite size effects, the simulation box was replicated once in each of the x and y directions, meaning that the simulation box was expanded from 80Å $\times$ 80 Å $\times$ 200 Å to 160 Å $\times$ 160Å $\times$ 200Å. 14000 CG beads of the $C_{12}E_2$ were used to construct the larger bilayer, which equals to 2000 molecules. This new system was also subjected to 1 ns of *NVT* equilibration in the same manner as the smaller bilayer. To insert the NP, the water beads were removed, the simulation box dimension in the direction normal to the bilayer (z-direction) was set to 200 Å and the NP was inserted into the system 100 Å above the centre of mass of the bilayer followed by re-solvation.

Simulation Setup for NPT Production Runs

The system was simulated in the *NPT*-ensemble, with temperature and pressure set to 303 K and 1 atm respectively. The temperature and pressure were controlled using a Nosé-Hoover thermostat and barostat[134–136], both with relaxation times of 0.2 ps. The equations of motion were integrated using the rRESPA multiple-timestep algorithm [137] with a 2.0 fs inner (bonded) and 10.0 fs (non-bonded) outer timesteps. Non-bonded interactions were truncated at $r_{\text{cut}} = 15$ Å. Periodic Boundary Conditions (PBCs) were set in the x and y directions. A production run of 200 ns was run to ensure that the surfactant bilayer had reached consistency in it's properties with past experimental and simulation results.

4.4 Free Energy Calculations

In order to get a complete picture of NP translocation energetics, we have implemented the *umbrella sampling method* (US).

4.4.1 Umbrella Sampling (US)

The free energy change of the NP translocation was calculated using the umbrella sampling (US) technique - the theory behind US has been covered in chapter 2. A spring constant of $k = 25.0$ kcal mol^{-1} was used to anchor the NP along the bilayer normal from 0 Å to 30 Å in 1 Å intervals, resulting in 30 windows for each nanoparticle. The coordinate distributions of each window was checked for overlap. The *weighted-histogram analysis method* (WHAM) program developed by Grossfield [117] was used to extract the final PMF of the trajectory.

4.5 Profiling the Dynamics of the Bilayer by Pulling the NPs through the Bilayer Normal

To analyse the dynamical effects of the bilayer with the NP translocation, and to aid in the understanding of the characteristics of the free energy profile across the bilayer normal, we used the *steered molecular dynamics* method (SMD) to pull the NP through the bilayer. To simulate the NP going through the bilayer, the NP was moved from it's initial configuration at z = 50 Å above the bilayer COM towards z = -50 Å with *constant velocity* simulations (for the sake of brevity, analyses are shown between 30 (above the bilayer headgroups) to 0 (center of the bilayer) Å range). To restrain the NP around the reaction coordinate, a stiff spring potential with $k = 25$ kcal mol^{-1} Å was set. Every pulling simulations for each NP from z = 30 Å to z = -30 Å was computed for the velocity at 5×10^{-7} Å fs^{-1}.

Index	NP type	R (nm)	System	N
1	hydrophile	1.0	US	30
2	hydrophile	1.5	US	30
3	hydrophile	2.0	US	30
4	hydrophobe	1.0	US	30
5	hydrophobe	1.5	US	30
6	hydrophobe	2.0	US	30
7	intermediate	1.0	US	30
8	intermediate	1.5	US	30
9	intermediate	2.0	US	30

Table 4.1 The list of US simulations undertaken in this work. The pulling simulations have not been included in this, as it is used as a supplementary information analysis but not representing the main PMF through the bilayer for each NP

Index	NP type	R (nm)	Velocity (Å fs^{-1})
1	hydrophile	1.0	5.0×10^{-7}
2	hydrophile	1.5	5.0×10^{-7}
3	hydrophile	2.0	5.0×10^{-7}
4	hydrophobe	1.0	5.0×10^{-7}
5	hydrophobe	1.5	5.0×10^{-7}
6	hydrophobe	2.0	5.0×10^{-7}
7	intermediate	1.0	5.0×10^{-7}
8	intermediate	1.5	5.0×10^{-7}
9	intermediate	2.0	5.0×10^{-7}

Table 4.2 The list of pulling simulations undertaken in this work.

4.5.1 Diffusion Coefficients

To demonstrate that the surfactant was well mixed prior to testing with the NPs, the surfactant simulation box was dynamically computed for 77 ns before inserting the NPs. For this prior 'mixing' simulation, we measured and calculated the 2D mean squared displacement (*MSD*), which is simply the numerical representation of the distance between molecular components squared. The *MSD* is defined as:

$$\mathrm{MSD} = \langle [r(t_0 + t) - r(t_0)]^2 \rangle \tag{4.5}$$

where the angular brackets represent the average. From this, the diffusion coefficient (D) can be calculated as the convergence of the following relation between the MSD and D:

$$D = \frac{MSD}{2dt} \tag{4.6}$$

where d is the dimensionality of the system, and t is the simulation time. By rearranging the equation, we can extract the value of D by the relation:

$$2dDt = MSD \tag{4.7}$$

Which shows that the gradient of the MSD plot can be used to extract the value of D. If D is observed to converge in the initial simulation run, then we can conclude that the system has been well mixed, and hence we can undertake the NP analysis simulations.

4.5.2 Calculating the Flux for the NP-Bilayer Simulations

As a form of semipermeable membrane, evidence has shown that the fluidity of the membrane is linked to the water flux in the bilayer. For example, the inclusion of cholesterol within aliphatic chains tightens the packing between the lipid tailgroups, which produces a reduced water flux across the membrane [138]. Here, we are interested in the effect on the translocation/flux of water of the presence of NPs with differing hydrophobicities, to ascertain the difference in mechanism in a quantitative manner. The procedure of calculating the flow of water is as follows. The plane of the bilayer normal was set as the surface at which an event of flux occurs upon crossing - all water beads passing this point were counted as a component of flux. The flux can be related to the diffusion coefficient of the water arising from the concentration gradient between the bulk water phases and in the surfactant. Fick's law dictates:

$$D = \frac{J\Delta x}{A\Delta C} \tag{4.8}$$

where J is the unidirectional flux of water, A is the area of the bilayer, ΔC is the water concentration change over the distance Δx. Here, we define the Δx as the distance between the lateral plane bilayer at the center (z = 0 Å) and the region of the headgroups of the surfactant (z = 1.8 Å). As we know the total area of the bilayer, the concentration of water in the bulk water and the interior of the surfactant bilayer and the number of water crossings, division of the flux by the surface area of the bilayer gives us an estimate of the flux involved for each NP. This methodology was implemented for the pulling simulations - this series of experiments is illustrated in table 4.2. To measure the flux for the equivalent simulations, the flux was measured at 3 points - at the points where the US bin is at $z = 0$.

4.6 Results

We have divided up the results to two sections - an analysis section to demonstrate that local properties of the $C_{12}E_2$ bilayer have been adequately equilibrated, and the latter section discussing the individual mechanisms of the NPs and their effects upon the bilayer.

4.6.1 Analysis

MSD and Diffusion Coefficient Measurements

Figure 4.5 shows the measured 2D *MSD* values over 77 ns. To estimate the diffusion coefficient (D), a straight line was fitted to the linear regime of the *MSD* versus time graph between 20 ns and 77 ns. From equation 4.7, the value of D was determined to be 2.209×10^{-6} cm^2 s^{-1} (2.209×10^{-10} m^2 s^{-1}). Reported values of the diffusion coefficient [139] were 3×10^{-10} m^2 s^{-1}, which is very close to the value measured from this work. Hence, as the diffusion coefficient of the surfactant was in agreement with the atomistic simulations seen in reference [139], we summised that the system was equilibrated and ready for NP simulations.

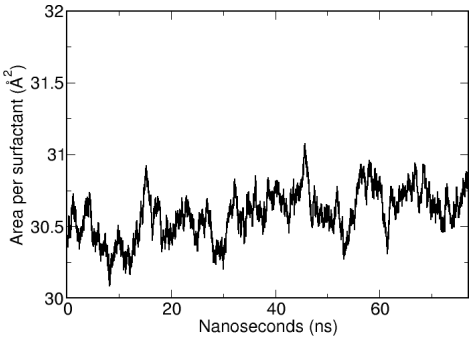

Fig. 4.4 The time evolution in the area per surfactant. The initial testing run was run for 77 ns under an *NPT* ensemble.

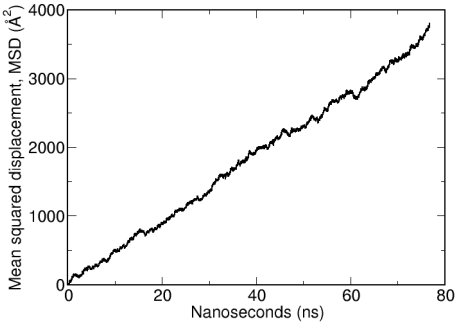

Fig. 4.5 The MSD over the 77 ns equilibration run.

Area per Surfactant and Density Profiles

Experimental values for the area per surfactant approximate to 30 - 30.5 Å^2 per molecule. Figure 4.4 shows the area per surfactant over the first 77 ns of equilibrium simulations. The area fluctuates around 30 Å^2, which is consistent with reported experimental and simulation values [2, 140] of near 34 Å^2. The density profile of the surfactant (Figure 4.6) shows that the average thickness of each surfactant leaflet is approximately 17-18 Å, which amounts to a total thickness of 36 Å. This is approximated from the bilayer centre to the peak of the EO bead, as illustrated in Figure 4.6. This thickness is consistent with those shown in previous simulation and experimental data [2, 139–141].

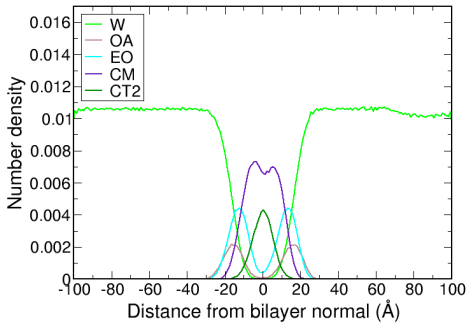

Fig. 4.6 The density profile of each CG beads in the bilayer. The EO and OA beads represents those within the headgroup region of the surfactant, while the CM and CT2 beads represent those composing the hydrophobic tailgroups. W represents the bulk water above and below the bilayer on the bilayer normal.

4.6.2 Mechanisms of NP Transit - Hydrophilic NPs - Pulling Simulations

The bilayer center is located at $z = 0$ Å, with the coordinates of the top and bottom of the box being $z = 100$ Å and $z = -100$ Å respectively. For the pulling simulations of hydrophilic NPs (Figure 4.7) we see a consistent mechanism of the NP interacting favourably with the hydrophilic headgroups. This is most prevalent in the cases of R = 1.0 and 1.5 nm. In the case of R = 2.0 nm NP, we see the destabilisation of the bilayer, accommodated by the formation of a pore on the approach of the NP towards the bilayer.

4.6.3 Mechanisms of NP Transit - Intermediate NPs - Pulling Simulations

Figure 4.8 show the pulling transit of the intermediate NPs for the R = 1.0. 1.5 and 2.0 nm pulling simulations. From a qualitative point of view, we do not see a significant difference in the transit mechanism between the intermediate and hydrophilic examples; the R = 1.0 and 1.5 nm examples show membrane curvature induced by coupling between the NP surface and the headgroups, while in the case of R = 2.0 nm, again, we see the destabilisation of

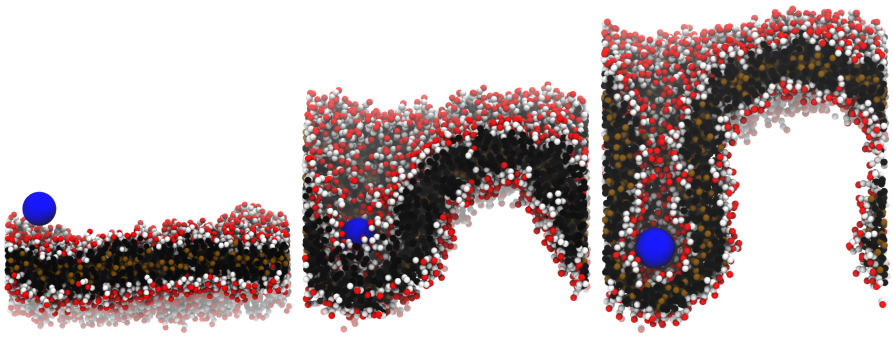

(a) R = 1.0 nm

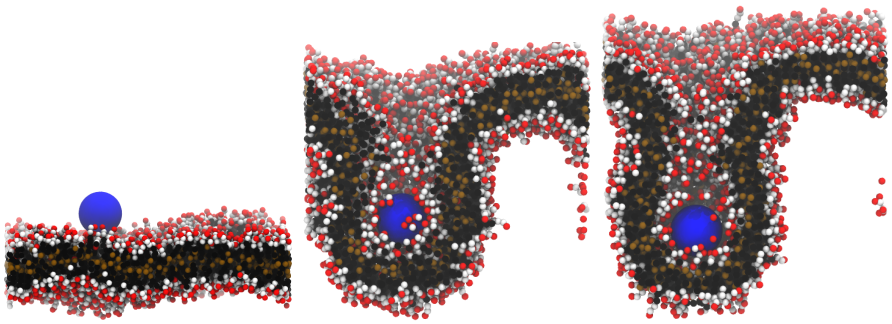

(b) R = 1.5 nm

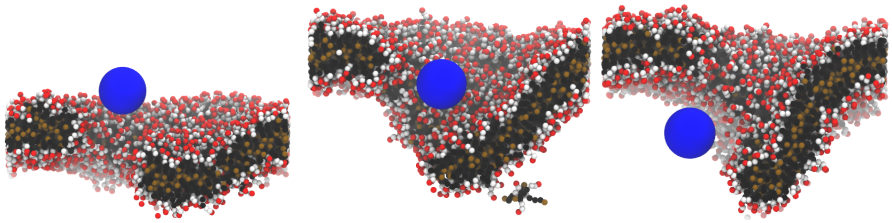

(c) R = 2.0 nm

Fig. 4.7 Simulation snapshots for the R = 1.0, 1.5 and 2.0 hydrophilic NPs for the SMD simulations with v = 5.0×10^{-7} Å fs^{-1}, shown in (a), (b) and (c) respectively.

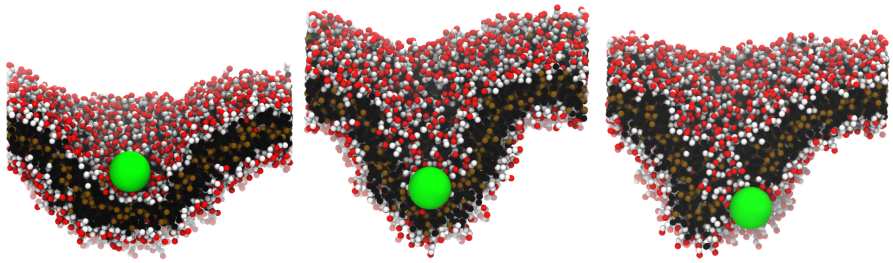

(a) R = 1.0 nm

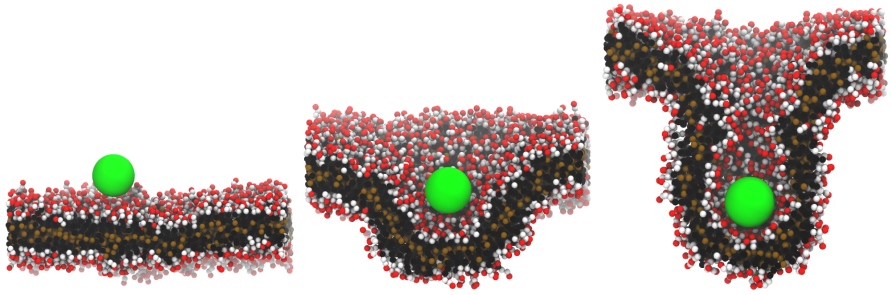

(b) R = 1.5 nm

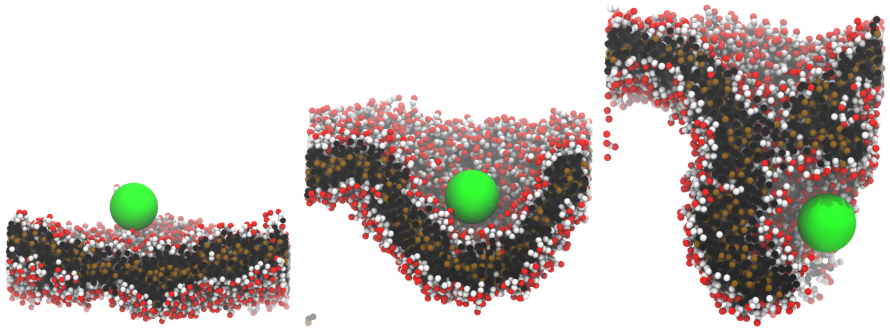

(c) R = 2.0 nm

Fig. 4.8 Simulation snapshots for the R = 1.0, 1.5 and 2.0 intermediate NPs for SMD simulations with v = 5.0 $\times$ 10^{-7} Å fs^{-1}, shown in (a), (b) and (c) respectively.

the bilayer and pore formation on the approach of the NP as with the hydrophilic example.

4.6.4 Mechanisms of NP Transit - Hydrophobic NPs - Pulling simulations

Figure 4.9 show the pulling transit of the intermediate NPs for the R = 1.0. 1.5 and 2.0 nm. In each case, we can observe significant attraction between the NPs and the hydrophobic tailgroups, which shows the entrapment of the NP above the bilayer surface.

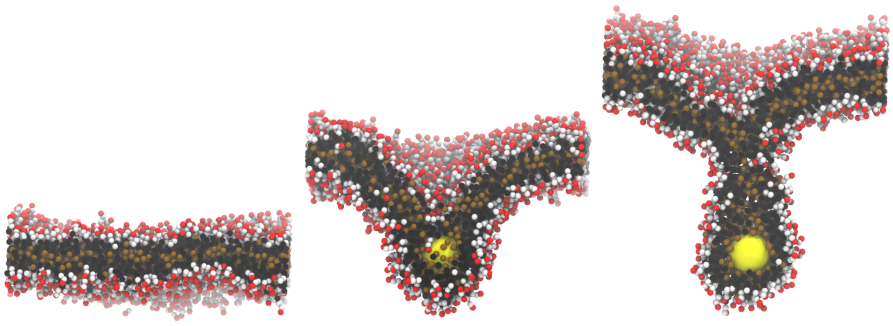

(a) R = 1.0 nm

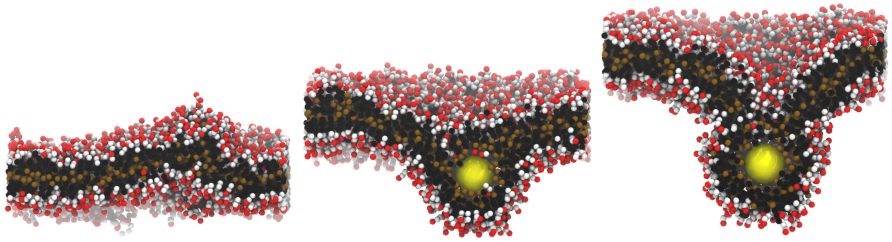

(b) R = 1.5 nm

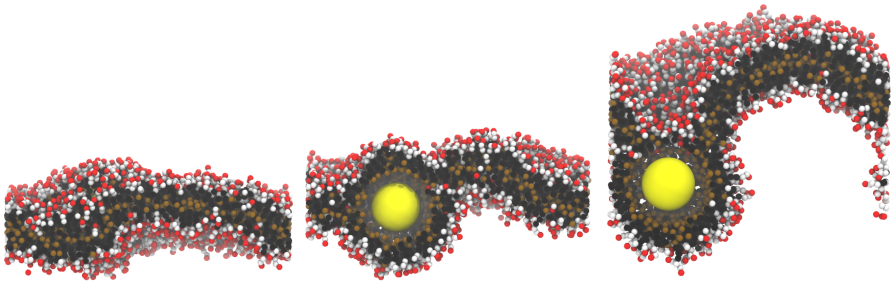

(c) R = 2.0 nm

Fig. 4.9 Simulation snapshots for the R = 1.0, 1.5 and 2.0 hydrophobic NPs for SMD simulations with v = 5.0 $\times$ 10^{-7} Å fs^{-1}, shown in (a), (b) and (c) respectively.

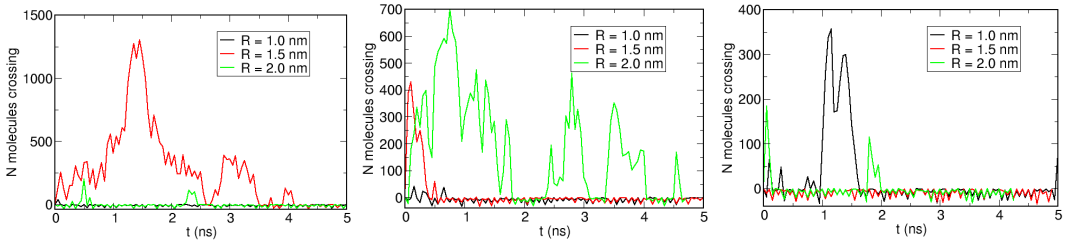

(a) (b) (c)

Fig. 4.10 The directional water flux as a function of simulation time. (a) shows the hydrophilic NPs, (b) the intermediate NPs, and (c) the hydrophobic NPs. Each flux calculation was computed when the NP was restrained at z = 0 Å. Each one of the water flux computations was calculated from the latter 5 ns of the z = 0 Å US simulations.

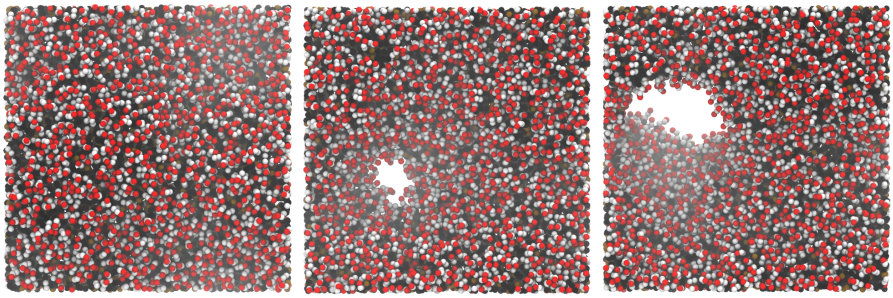

(a) $R = 1.0$ nm, $z = 0$ Å (b) $R = 1.5$ nm, $z = 0$ Å (c) $R = 2.0$ nm, $z = 0$ Å

Fig. 4.11 Top-down view of the bilayer when $z = 0$ Å for the hydrophilic NP; (a) shows the $R = 1.0$ nm NP, (b) shows the $R = 1.5$ nm NP, and (c) shows the $R = 2.0$ nm NP.

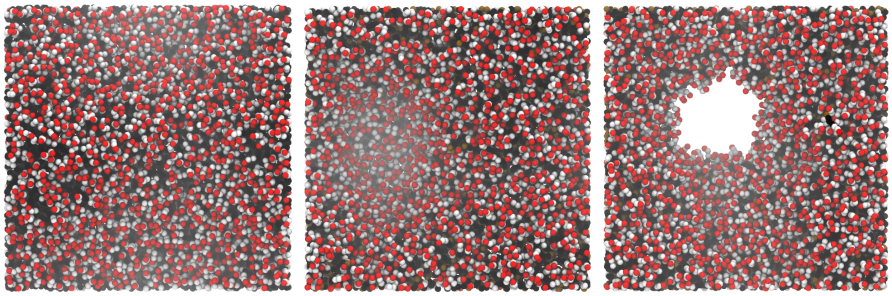

(a) $R = 1.0$ nm, $z = 0$ Å (b) $R = 1.5$ nm, $z = 0$ Å (c) $R = 2.0$ nm, $z = 0$ Å

Fig. 4.12 Top-down view of the bilayer when $z = 0$ Å for the intermediate NP; (a) shows the $R = 1.0$ nm NP, (b) shows the $R = 1.5$ nm NP, and (c) shows the $R = 2.0$ nm NP.

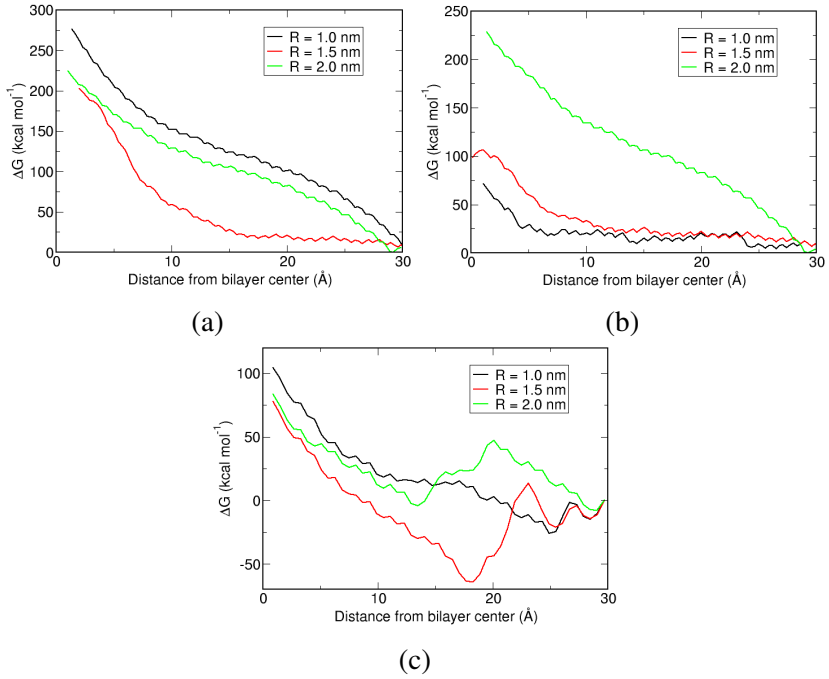

Fig. 4.13 Free energy profiles from US simulations for the hydrophilic, intermediate and hydrophobic NPs from 30 Å (bulk water) to 0 Å (bilayer center). (a) shows the hydrophilic NPs, (b) the intermediate NPs, and (c) the hydrophobic NPs respectively.

Water Flux of the Bilayer with NPs

Figure 4.10 shows the water flux around the z = 0 Å plane for each NP example. Here, we see a unique trend for each type of NP - for the hydrophilic NPs, we see the greatest water crossings with the R = 1.5 nm NP, while showing minor peaks of flux for the R = 2.0 nm NP. In the Intermediate case, we can see that the only apparent flux is observed with the R = 2.0 nm example. With the hydrophobic NPs, we observe peaks of small water leakage through the bilayer for the R = 2.0 nm NP, while significant peaks of water leakage was observed in the case of the R = 1.0 nm NP.

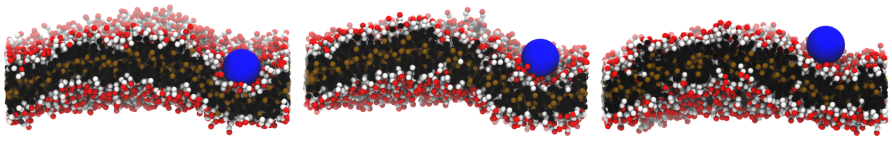

(a) $z = 0$ Å (b) $z = 10$ Å (c) $z = 20$ Å

Fig. 4.14 Snapshots of the bilayer at $z = 0$, 10 and 20 Å in the bilayer normal for the $R = 1.0$ nm hydrophilic NP, illustrated in (a), (b) and (c) respectively.

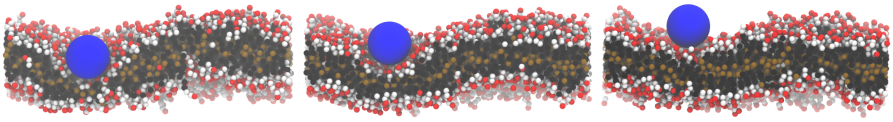

(a) $z = 0$ Å (b) $z = 10$ Å (c) $z = 20$ Å

Fig. 4.15 Snapshots of the bilayer at $z = 0$, 10 and 20 Å in the bilayer normal for the $R = 1.5$ nm hydrophilic NP, illustrated in (a), (b) and (c) respectively.

4.6.5 Analysis of the Free Energy Profiles

Hydrophilic NPs - US Simulations

Figure 4.13(a) shows the free energy profiles for R = 1.0, 1.5 and 2.0 nm hydrophilic NPs as obtained from US simulations. The pattern for the R = 1.0 and 2.0 nm show similar trends, where we see a gradual increase in the free energy as the NP enters the bilayer - the magnitude of change was greatest with the $R = 1.0$ nm example, with a free energy change of $\tilde{2}75$ kcal mol^{-1}, compared to the $\tilde{2}25$ kcal mol^{-1} change with the $R = 2.0$ nm example. We see a dramatically different profile for the $R = 1.5$ nm profile, where the increase in energy is significant near the 0 - 10 Å region, where the NP is fully embedded within the hydrophobic tailgroup region. The change in free energy in this case was similar in magnitude to the R = 2.0 nm example, of $\tilde{2}00$ kcal mol^{-1}.

Intermediate type NPs - US Simulations

Figure 4.13(b) shows the free energy profiles for R = 1.0, 1.5 and 2.0 nm intermediate NPs as obtained from US simulations. Here, the R = 1.0 and 1.5 nm profiles show a similar

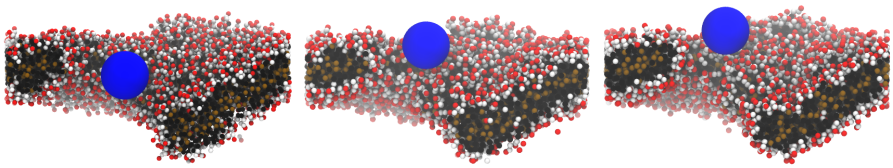

(a) $z = 0$ Å (b) $z = 10$ Å (c) $z = 20$ Å

Fig. 4.16 Snapshots of the bilayer at $z = 0$, 10 and 20 Å in the bilayer normal for the $R = 2.0$ nm hydrophilic NP, illustrated in (a), (b) and (c) respectively.

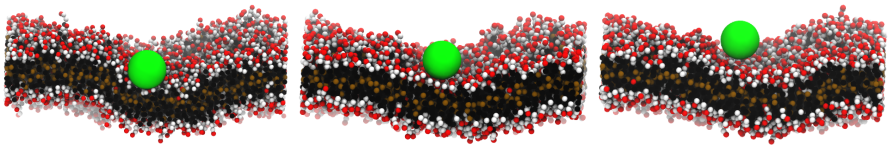

(a) $z = 0$ Å (b) $z = 10$ Å (c) $z = 20$ Å

Fig. 4.17 Snapshots of the bilayer at $z = 0$, 10 and 20 Å in the bilayer normal for the $R = 1.0$ nm intermediate NP, illustrated in (a), (b) and (c) respectively.

trend - unlike in the hydrophilic examples, we see a flattening of the free energy profile between 8 - 30 Å, with a steep increase near the core of hydrophobic region at 0 - 8 Å, with a free energy change of approximately 75 and 100 kcal mol^{-1} respectively, in contrast to the gradual increase seen with the hydrophilic example. This trend was not followed with the $R = 2.0$ nm example, which follows the hydrophilic NP example closely, with a gradual increase of the PMF, with a change of approximately 230 kcal mol^{-1}.

Hydrophobic Type NPs - US Simulations

Figure 4.13(c) shows the US free energy profiles for the $R = 1.0$, 1.5 and 2.0 nm hydrophobic NPs. The lack of symmetry present of the energy well can be explained due to the

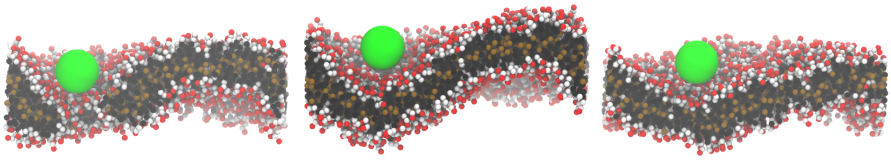

(a) $z = 0$ Å (b) $z = 10$ Å (c) $z = 20$ Å

Fig. 4.18 Snapshots of the bilayer at $z = 0$, 10 and 20 Å in the bilayer normal for the $R = 1.5$ nm intermediate NP, illustrated in (a), (b) and (c) respectively.

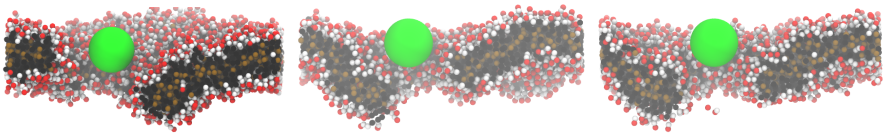

(a) $z = 0$ Å (b) $z = 10$ Å (c) $z = 20$ Å

Fig. 4.19 Snapshots of the bilayer at $z = 0$, 10 and 20 Å in the bilayer normal for the $R = 2.0$ nm intermediate NP, illustrated in (a), (b) and (c) respectively.

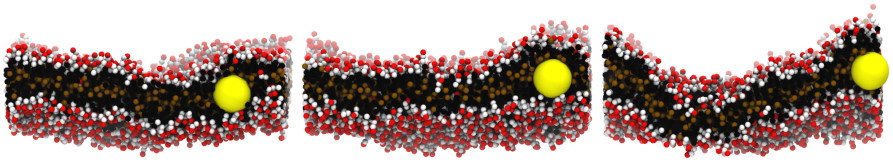

(a) $z = 0$ Å (b) $z = 10$ Å (c) $z = 20$ Å

Fig. 4.20 Snapshots of the bilayer at $z = 0$, 10 and 20 Å in the bilayer normal for the $R = 1.0$ nm hydrophobic NP, illustrated in (a), (b) and (c) respectively.

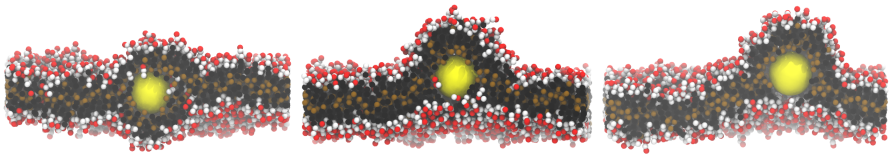

(a) $z = 0$ Å (b) $z = 10$ Å (c) $z = 20$ Å

Fig. 4.21 Snapshots of the bilayer at $z = 0$, 10 and 20 Å in the bilayer normal for the $R = 1.5$ nm hydrophobic NP, illustrated in (a), (b) and (c) respectively.

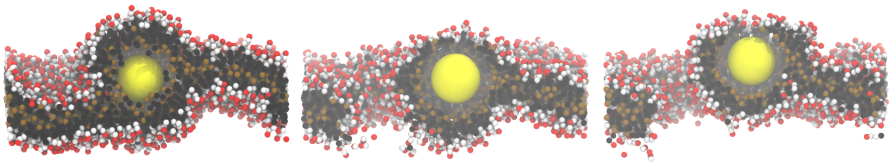

(a) $z = 0$ Å (b) $z = 10$ Å (c) $z = 20$ Å

Fig. 4.22 Snapshots of the bilayer at $z = 0$, 10 and 20 Å in the bilayer normal for the $R = 2.0$ nm hydrophobic NP, illustrated in (a), (b) and (c) respectively.

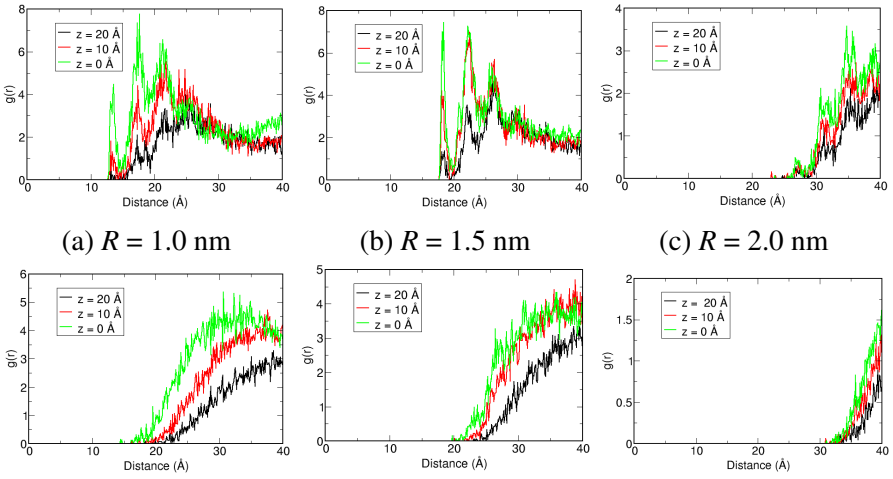

(a) R = 1.0 nm (b) R = 1.5 nm (c) R = 2.0 nm

(d) R = 1.0 nm (e) R = 1.5 nm (f) R = 2.0 nm

Fig. 4.23 RDF profiles around each hydrophilic NP at z = 20, 10 and 0 Å for the headgroups (OA and EO, shown in Figures (a), (b) and (c)) and tailgroups (CM and CT2, shown in Figures (d), (e) and (f)).

hydrophobic attraction between the surfactant tailgroups and the NP, which results in the bilayer rising up to intercept the NP between z = 0 - 30 Å, which indicates that the free energy trough that is correlated with the bilayer center will be placed above the bilayer normal - we see troughs of -25, -60, and -50 kcal mol^{-1} at 25 Å, 16 Å and 14 Å for the R = 1.0, 1.5 and 2.0 nm NP respectively.

4.7 Discussion

Due to the nature of the construction of the NP, there is no direct experimental equivalent that we can compare the PMF to in a quantitative manner. However, by comparing the properties of the system with respect to the NP position, comparisons with published literature can be made. Similar approaches at fine-graining the NP property has been done; using discontinuous molecular dynamics (DMD), NP studies done by Curtis *et al* [126] illustrated a radius limit for the hydrophilic NP to change from a bilayer 'embedding' phase (where the bilayer curves around the bilayer) to a bilayer 'wrapping' phase (where the bilayer com-

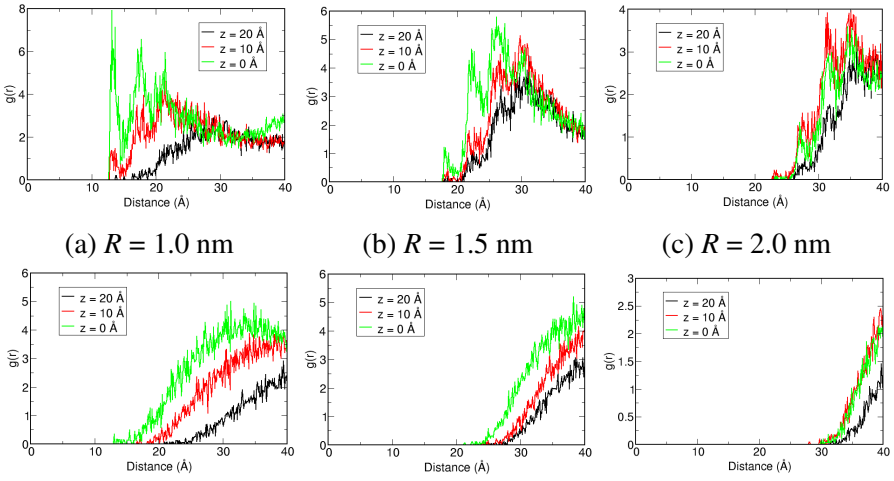

(a) R = 1.0 nm (b) R = 1.5 nm (c) R = 2.0 nm

(d) R = 1.0 nm (e) R = 1.5 nm (f) R = 2.0 nm

Fig. 4.24 RDF profiles around each intermediate NP at $z = 20$, 10 and 0 Å for the headgroups (OA and EO, shown in Figures (a), (b) and (c)) and tailgroups (CM and CT2, shown in Figures (d), (e) and (f)).

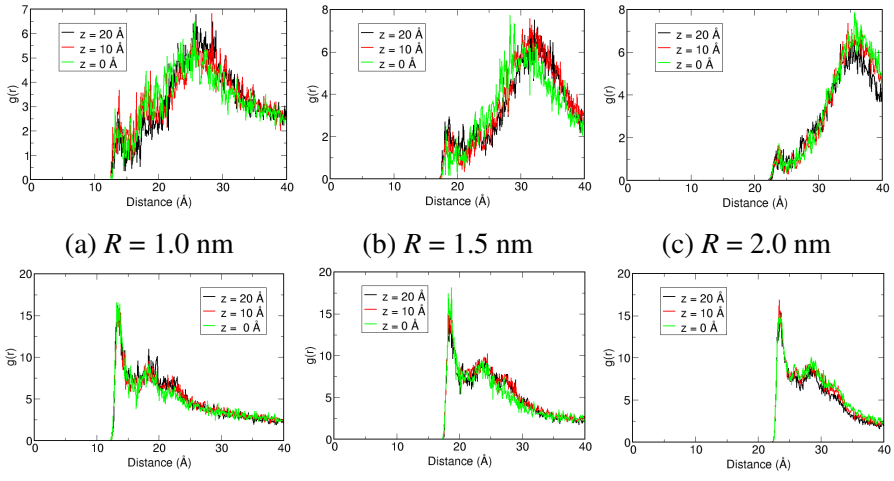

(a) R = 1.0 nm (b) R = 1.5 nm (c) R = 2.0 nm

(d) R = 1.0 nm (e) R = 1.5 nm (f) R = 2.0 nm

Fig. 4.25 RDF profiles around each hydrophobic NP at $z = 20$, 10 and 0 Å for the headgroups (OA and EO, shown in Figures (a), (b) and (c)) and tailgroups (CM and CT2, shown in Figures (d), (e) and (f)).

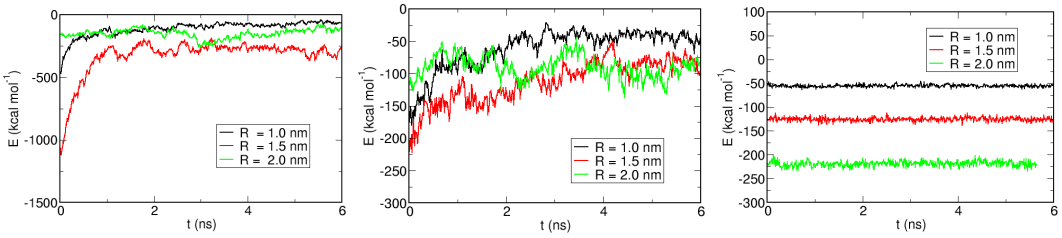

(a) (b) (c)

Fig. 4.26 The total interaction energy between the NPs and the $C_{12}E_2$ components. (a), (b) and (c) corresponds to the energy plots of the hydrophilic, intermediate and hydrophobic NPs respectively.

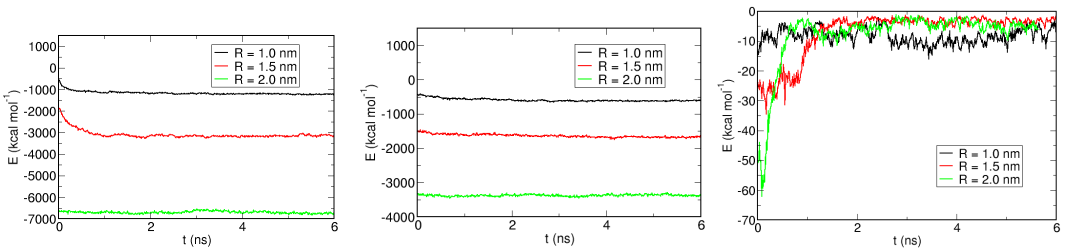

(a) (b) (c)

Fig. 4.27 The total interaction energy between the NPs and W beads (solvent). (a), (b) and (c) corresponds to the energy plots of the hydrophilic, intermediate and hydrophobic NPs respectively.

pletely wraps around the bilayer). Here, the range of radius measured in our study (R = 1.0 - 2.0 nm) falls within the 'embedding' phase, which is consistent with the DMD study, which is consistent with the phenomena observed for the hydrophilic and intermediate NPs.

To distinguish and analyse the mechanistic difference between each NP, the magnitude of change in the free energy profile and the shape of the PMF will be the main factors of consideration in this discussion. From visual analysis (Figures 4.7 - 4.9), for the case of the R = 1.0 and 1.5 nm hydrophilic and intermediate NPs, we observe a strong adsorption of the headgroups to the surface of the NP. This is consistent with simulations of hydrophilic NPs done by Rocha *et al* [142] and Gu [143], amongst others, where a higher charge density on the NP (which corresponded to a greater hydrophilicity) correlated with a stronger adsorption on the bilayer surface. Simulations of hydrophilic NPs by Gu [143] indicated that there is competition between the favourable electrostatic interaction between the charged groups in the bilayer and the positive/negatively charged NP, and the unfavourable energy associated with bending the bilayer. Simulations of acylated and un-acylated dendrimers through a lipid bilayer [144] show that the unacylated dendrimer acts analogous to the hydrophobic NP, as shown by the insertion of the dendrimer into the tailgroups; the acylated version shows adsorption on the surface of a 1,2-dipalmitoyl-sn-glycero-3-phosphocholine (DPPC) bilayer, analogous to the hydrophilic NPs simulated. The model we have used does not include charged components within the surfactant groups nor implement surface charges on the NP surface. However, the association of the hydrophilic headgroups around the hydrophilic/intermediate NPs follows the pattern of previous studies.

From the US profiles, the intermediate NP free energy profiles show a flattening of the free energy between 3-30 Å along the bilayer normal for the R = 1.0 and 1.5 nm, which is absent in the case of the R = 2.0 nm profile. This 'flattening' effect is consistent with recent

studies demonstrated by Su *et al* [145], who suggested that, at intermediate hydrophobicity, the NP is distributed between the head and tail groups, and in-between the bilayer leaflet layers, all accessible through a flattening of the free energy profile across the bilayer normal. Su also suggested that the barrier at the tail end of the flattened PMF (shown in 0 - 5 Å in the R = 1.0 and 1.5 nm intermediate NP profiles) is associated with the entropic cost of inducing order within the bilayer tailgroups. In that case, the barrier was shown to be within 10s of kT, which is clearly smaller than the barrier observed in this example, (which is in the range of 50 - 100 kcal mol^{-1}). It may be the case that the NP model used in this example overestimates the barrier. Simulations with intermediate type dendrimers by Hwankyu *et al* [144] demonstrated that the intermediate dendrimers adsorbed onto the bilayer surface (which is an 'acylated' trait) with strands of the dendrimer penetrate inside the bilayer, which suggests that such intermediate NPs to 'latch-on' to the hydrophilic surface, and subsequently penetrating through the bilayer normal through increased hydrophobic contacts. Another mechanism of insertion of intermediate type NPs was demonstrated using striated NPs as simulated by Yinfeng *et al* [146], who demonstrated that the rotational dynamics of hydrophobic/hydrophilic striped NPs can rotate while inside the bilayer to minimise the interaction with the hydrophobic interior, which again, leads to a 'flattening' of the free energy profile.

In other examples, Zhang *et al* [147] performed *dissipative particle dynamics* (DPD) membrane translocation simulations of NPs with fully hydrophilic (WNP), hydrophobic (ONP) and a random mixture of hydrophilic and hydrophobic points to represent a NP of intermediate hydrophobicity (RNP). Here, the resistance force (the combined repulsion force from the hydrophilic headgroups and hydrophobic tailgroups of the bilayer) acting against the RNP was minimal - it has been hypothesised that the randomly distributed hydrophilic forces counteract the attractive hydrophobic forces near the tailgroup region. Furthermore, it may

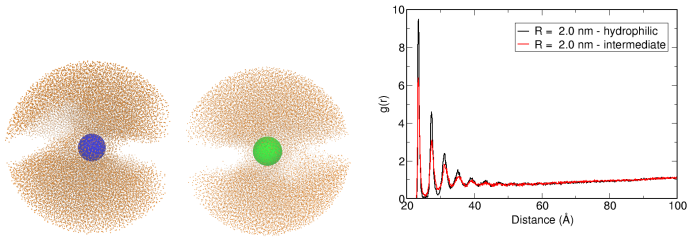

(a) (b) (c)

Fig. 4.28 Illustration of the water density around the $R = 2.0$ nm hydrophilic and intermediate NP, shown in a radius of 10 nm around each NP, shown in (a) and (b) respectively. (c) shows the corresponding RDF density profile.

be the case that larger aggregations will undergo cooperative mechanisms of translocation, which has not been covered with this model and will be a subject for a future work. This observation was followed by a flattening of the PMF near the membrane region, which is entirely consistent with the observation in this study in the case of $R = 1.0$ and 1.5 nm intermediate NPs. Another example of this type of direct penetration through membranes with intermediate hydrophobicity comes with striped NPs, as designed from monolayer-protected NPs [88, 148], which suggested that homogenous patterning of hydrophilic/hydrophobic beads on a NP surface enables the passive translocation of NPs through a lipid bilayer.

In contrast to the smaller examples, the $R = 2.0$ nm hydrophilic and intermediate NPs clearly shows the formation of holes or 'doors' on approach to the bilayer surface, as demonstrated in both the US and pulling simulations, and illustrated in Figure 4.11 and 4.12. The formation of doors has been speculated upon in the past; MD simulations by Lin *et al* [149] illustrated that the interaction of cationic alkanethiol-ligand AuNPs with the transmembrane potential as the driver of the movement of the NP, with the formation of similar doors on approach to the bilayer surface - it is thought that this mechanism is responsible for the rapid intake of cationic NPs and cell-penetrating peptides (CPPs) [150]. Here, as we have not included the ionic potential as a factor in the experiment, an alternate mechanism for

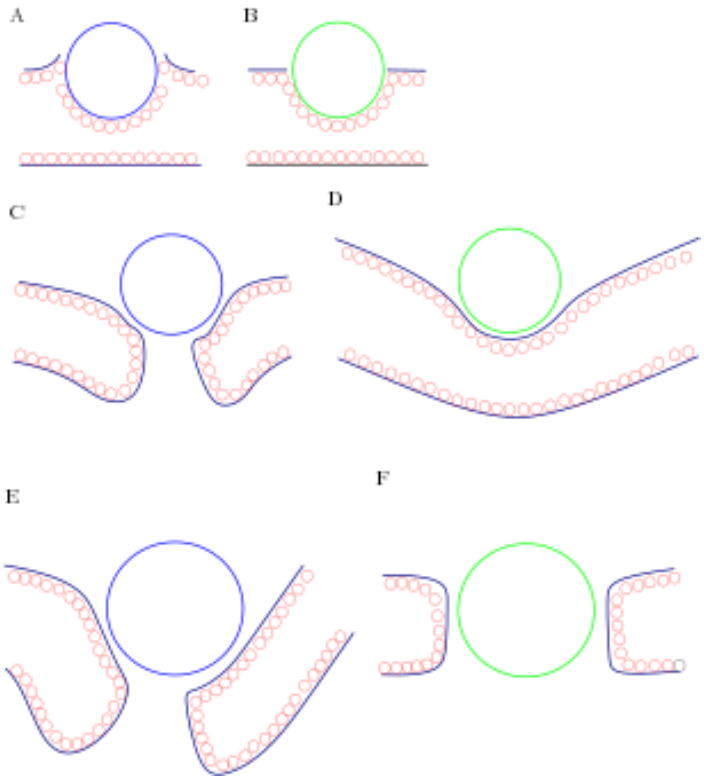

Fig. 4.29 The bilayer conformation with the NP at z = 0 Å; A and B shows the bilayer conformation around the NP for the R = 1.0 hydrophilic and intermediate NPs, C and D shows the bilayer conformation around the R = 1.5 hydrophilic and intermediate NPs, and D and E show the bilayer conformation around the R = 2.0 hydrophilic and intermediate NPs respectively.

direct penetration in a non-ionic case is necessary. The resultant bilayer geometry around the NPs for the hydrophilic and intermediate examples is illustrated in Figure 4.29. We see that for R = 1.0 nm, the NP does not rupture the bilayer when placed in the center of the bilayer at z = 0 Å. With the R = 1.5 nm example, we see a clear difference, where the hydrophilic example clearly shows a rupture/hole in the membrane, whilst being absent in the intermediate example. With the R = 2.0 nm example, we see that both the hydrophilic and intermediate NPs induce deformation of the bilayer and subsequent formation of 'doors' on approach to the bilayer. However, the shape of the bilayer around the rupture differs; in the hydrophilic example, the surrounding surfactants become 'folded', while in the intermediate example we observe a clear hole around the NP lateral plane, which indicates that the increased interaction with the hydrophobic tailgroups clearly affects rupture geometry. This rupture is not apparent with the hydrophobic NP example.

For further analysis on the porosity of the bilayer, we can analyze the water flux data, which is shown in Figure 4.10 (a), (b) and (c) for the hydrophilic, intermediate and hydrophobic NPs respectively. Here, what is noticeable is the reduction in flux for the hydrophilic NP when increasing its size from R = 1.5 nm to R = 2.0 nm. The opposite trend is seen in with the intermediate type NPs of R = 1.5 and 2.0 nm. To analyze this phenomena, we studied the RDF of water beads around each NP for the R = 2.0 nm example. This is shown in Figure 4.28 - here, we see show a significantly ordered solvent density around the hydrophilic NP compared to the intermediate example. Hence, we may speculate that the hydration sphere around the R = 2.0 nm hydrophilic NP actively prevents the flux of water molecules around the pore, while the dampened hydrophilicity of the intermediate equivalent cannot effectively order around the NP, which is reflected by the increase in the water flux.

To ascertain the total force contribution on the NP surface, we have computed the total

interaction energy between the NP and the surfactant and between the NP and bilayer/water. This is shown in Figures 4.26 and 4.27 respectively. The hydrophilic and intermediate examples show similar trends, but we see a diminished interaction energy with the surfactants with the intermediate types, where we see an interaction energy of -100 kcal mol^{-1}, compared to the limit of -300 kcal mol^{-1} we observe with the hydrophilic example, as would be expected from our model. When comparing the hydrophobic example with the hydrophilic/intermediate example, we see a high fluctuation in the interaction energy in the first two cases, which would suggest that the association between the surfactants and the hydrophilic/intermediate examples are far more unstable. The interaction energy with the solvent also indicates the high discrepancy in interaction energies between the hydrophilic and intermediate example, where in the hydrophilic case, the interaction energy with the solvent reaches values of -6800 kcal mol^{-1}, while we only observe values of 3400 kcal mol^{-1} at a maximum. In the hydrophobic case, the interaction energy with the solvent is minimal, as is expected. This indicates that in the hydrophilic example, the association with the solvent is significant and the headgroups is significant, while in the intermediate example, the interaction force between the bilayer and the NP surface is weak. This would suggest that the large intermediate NP largely deforms the bilayer on approach through its geometric curvature, while in the hydrophilic example, the increased association of the solvent with the NP surface changes the deformation on approach.

4.8 Conclusion

We have adapted the Hamaker-like continuum potentials to construct 3 different types of NPs; a *hydrophilic*, *hydrophobic* and *intermediate* particle of 3 different sizes; R = 1.0, 1.5 and 2.0 nm, and analysed the translocation of each NP through a neutral $C_{12}E_2$ bilayer

using NP pulling and US simulations with the bilayer normal as the reaction coordinate. By analyzing the free energy profile, flux and surfactant configuration around the NP, we have attempted to characterize the mechanism for each hydrophobicity. We see that for the hydrophilic NP, at smaller sizes (R = 1.0, 1.5 nm), the favourable interaction between the hydrophilic headgroups of the surfactants and the NP surface overcomes the energetic cost of forming the curvature around the NP, while for the larger example (R = 2.0 nm), we observe that the NP forms a 'hole' upon approach to the surfactant surface. In the intermediate NP case, we observe a flattening of the PMF in the surfactant region in the cases of the R = 1.0 and 1.5 nm radius, while with the R = 2.0 nm case, we see the formation of a hole on approach to the surfactant surface. While numerous challenges to the clinical applications of NPs remain, this study shows that by tuning the hydrophobicity of the NP surface, it may be possible to design targeted NP delivery mechanisms that can strictly bypass the bilayer - as the lifetime within the bilayer may be short, the concerns regarding nanotoxicity and complications regarding accumulation of NPs within the interior of the membrane.

CHAPTER 5

HYDROPHOBIC NANOPARTICLES ACT AS LINEACTANTS IN MIXED BILAYERS

The interactions between heterogeneous components in a biomimetic bilayer controls its physical properties such as its rigidity, local and bulk curvature and propensity towards phenomena such as membrane fission and fusion. In particular, membrane proteins (MPs) and nanoparticles (NPs) have been subjects of intense interest due to their similar scale to the bilayer width and because of their ability to affect local membrane structure. However, how such NPs interact in the presence of heterogeneous aggregates in the bilayer has been the subject of much debate, especially its effect on raft-like structures. To better understand the effects of hydrophobic integration of nanoscale components on such raft-like structures, we have simulated a generic hydrophobic NP with a generic two-component polymeric bilayer. We find that the hydrophobic NP tends to aggregate at the phase interface, acting as a line tension *relaxant* i.e. a lineactant (or line-active) on the phase separated interface, which results in differing demixing behavior, and the slowing of phase separation of surfactant aggregates. In addition, we have demonstrated that depending on the size of the NP, the effect of the line tension can drive the a cap/bud formation around the NP, ultimately resulting in the formation of a NP-micelle formation. The results from this study illustrates that NP nanotoxicity arising from hydrophobicity must take into account its effect on aggregate

domains, and shows that the mechanism of bud/micelle formation may form a significant part of the translocation mechanisms of nanoscale-virions and the mechanism of membrane proteins near membrane domains.

5.1 Introduction

Lipids and similar polyether/polyethylene type molecules form the building blocks of a whole range of materials ranging from traditional manufacturing ingredients such as detergents and paints [151], to more recent, complex, applications such as in bio-sensing devices, drug delivery capsules and biomedical apparatus [152–156]. Whether the lipid/polymer is biological or artificial, its basic building blocks comprise short hydrophilic headgroups and a longer hydrophobic tails. Attaching these opposites groups into a single lipid type species, this allows the aggregation of these molecules - the hydrophilic headgroups can associate with the surrounding bulk water surrounding it, and the water-avoiding hydrophobic tail-groups which aggregate away from the headgroup and water. Depending on the structure and the molecular species which make up the lipid/polymer moiety, the bulk structure can form a large array of structures ranging from a monolayer micelle to a semi-flexible planar bilayer or a bilayer vesicle. Within these bilayers, heterogeneous components can control the overall physical characteristics, such as the curvature, rigidity and permeability. Bilayers also constitute the semi-permeable vesicles that build the major organelles within biological organisms.

The preferential interactions between the molecular components, due to steric preference or direct intermolecular energetic preference has been hypothesised to drive numerous complex processes within the bilayer. The pioneering work by Simons and Ikonen [157] illustrated the possible existence of *lipid rafts* - structures ranging from 10-200 nm radius - enriched semi-circular domains that are stabilised by heterogeneous components, forming

what are known as liquid-ordered (l_o) phases (which primarily make up the raft formation) from the liquid-disordered (l_d) components. The formation of patches in a mixed bilayer has been suggested to form the platform for complex macro-structures, such as membrane proteins to control the translocation of particles and ions across the bilayer [58]. In general, it is thought that the energetic cost of the raft formation depends on two main factors - the free energy gain when like lipid species coagulate together (either through packing energy or hydrophobic interaction match), and secondly, minimisation of the free energy cost of domain boundaries. It has been suggested that the hybrid lipid species (with a saturated and unsaturated tail), such as monosaturated POPC may control the type and size of the domains formed, through a controlled 'loosening' of the membrane domain line tension. Other stabilising factors include the presence of cholesterol (CHOL), which aggregates to the saturated tailgroups, therefore acting as a stabilising element to l_o phases [158].

The presence of raft-like structures has yet to be demonstrated without doubt, and lingering issues remain in terms of its lifetime within a membrane, and the minimum and maximum sizes of domains that may form, but an increasing number of experimental and simulation studies show mounting evidence towards its existence. For example, the evidence for lipid rafts was shown with fluorescence spectroscopy experiments with giant unilamellar vesicles (GUVs) by Baumgart *et al* [159, 160], where a 3 component (DSPC/DOPC/CHOL) mixed bilayer showed an abrupt increase in the raft formation - from modulated patterns to macroscopic round domains with a minor increase in the DOPC ratio in rapid order. In the past, Lawrence and Yuan [161, 162] showed demonstrated through atomic force microscopy (AFM) that phases increasing step-wise in thickness existed within heterogeneous membranes. More recently, Nickels *et al* [48] used neutron scattering length density (NSLD) and small angle neutron scattering (SANS) techniques to 'color' the lipid components (by labelling the hydrogen's on the lipids with hydrogen or deuterium atoms depending on its

saturation type), which demonstrated that domain-like (l_o) features had distinctive bending moduli.

With increasing amounts of experimental data for rafts, molecular simulation (MS) techniques has been used to reproduce the formation of such rafts. Hakoyoban *et al* [163] for example, used coarse-grained molecular dynamics (CG-MD) with the *MARTINI* [15] force field to systematically study a ternary 1,2-dioleoyl-sn-glycero-3-phosphocholine/1,2-dilauroyl-sn-glycero-3-phosphocholine/cholesterol (DOPC/DLPC/CHOL) system, with added variations in the headgroup and tailgroup regions. The study suggested that the rigidity of lipid/cholesterol species has a significant effect on stabilising/slowing the phase separation between l_o and and l_d species in a heterogeneous lipid bilayer system, which closely follows experimental observations. In addition, the interaction of raft-like aggregates with MPs seems to suggest that these can modulate the rate of phase separation. For example, Fowler *et al* [164] demonstrated through molecular simulation that the distribution and density of peripheral membrane proteins can change the bending rigidity. Hence, the domain formation in unsaturated/saturated mixtures has been shown to be slowed by the presence of such 'linking' proteins, where it can reduce the unfavourable contact in the interface between the l_o and l_d phases [164]. In addition, hybrid lipid structures (lipids with both saturated and unsaturated tails) has been shown evidence to act in a similar way. For example, Rosetti *et al* [165] demonstrated through quarternary mixtures of PAPC (hybrid)/DAPC (unsaturated)/DPPC (saturated)/CHOL mixtures that hybrid lipid type structures acted to reduce the hydrophobic mismatch area between the l_o and l_d regions. Furthermore, all-atomic (AA) simulation results by Hassan-Zadeh *et al* [166] demonstrated that POPC/PLPC/PAPC type lipids essentially 'even-out' the physical characteristics between the l_o and l_d phase, which effectively reduced the domain line tension. Hence, the primary role of line tension (LT) relaxants (otherwise referred to as lineactants) is believed to be modulating the rate of

phase separation by reducing the contact surface between the unfavourable components.

Hence, when designing practical applications to work in these complex environment, the interaction between any object and its interaction with the individual components, and larger structures such as these lipid rafts become an important factor to consider. Due to their potential for applications such as targeted drug-delivery and their high bio-compatibility, nanoparticles (NPs), nanometer-scale objects of various radius and anisotropy, have recently been a subject of intense interest in relation to their application with bilayer systems. As indicated from past studies, the primary driving force for the phase separation into l_o rafts and l_d is the LT between the phases.

NPs with hydrophobic characteristics have been shown to act in a similar manner. For example, Barnoud *et al* [167] observed that domain stability depends on the presence of aliphatic species/NPs (Octane, Hexadecane, Cyclohexane) near the l_d/l_o domains. In addition, through mesoscopic simulations, Cheung [168] also demonstrated the control of raft-like domains with mesoscale-dynamics in the presence of hydrophobic NPs, suggesting that a hydrophobic NP and a hydrophobic protein analogue can nucleate domains and act as lineactants, in a similar manner to membrane proteins. However, to the authors best knowledge, the effect and quantitative measure of a hydrophobic NP upon the rate and type of phase separation has not been studied before. In our work, we simulate a mixed bilayer with a hydrophobic NP of a series of radii - we designed a *continuum* model of a hydrophobic NP to model the effects of a nanoscale hydrophobic component in a delibrately phase-separated biomimetic surface. We show that the rate of phase separation increases with a larger radius, and we also show that the NP of all sizes locates itself within the interfaces between the phases. In addition, we show that with larger radius, the NP drives a budding process that may lead to the formation of caps to a full-fledged budding.

5.2 Methods

5.2.1 Preparation of the Mixed Biomimetic Models

The Base Surfactant Model and its Modification

The polyethylene glycol ($C_{12}E_2$) model used by Shinoda *et al* (otherwise known as the SDK model) [127, 128] was the basis of the model used in this work. All simulations were performed using the LAMMPS molecular dynamics package [112] (The *SDK* model is avaliable with the most recent LAMMPS release). The model has been parameterised against thermodynamic properties (densities, interfacial tensions, transfer free energies) and has been applied successfully by itself or as a model to study a range of soft matter systems [12, 129, 130] and recently extended to include representations of amino acid residues and rigid molecules such as cholesterol. A brief description of their CG approach follows here - within this model 3-5 heavy atoms are represented by a single interaction site or “bead" (one water bead represents three water molecules). The surfactant molecule is described using four CG bead types: OA (-CH_2OH) and EO (-CH_2OCH_2-) which represent the hydrophilic head group and CM (-$CH_2CH_2CH_2$-) and CT2 ($CH_3CH_2CH_2$-), which represent the hydrophobic tail groups. To produce a mixed bilayer, half of the $C_{12}E_2$ molecules were changed into modified equivalents, which has identical *molecular mechanical* (MM) (i.e. the intramolecular potentials are identical) properties. This initial configuration was produced by a randomized change of indices atoms of the bilayer data file. The modified lipid was produced by changing the *Lennard-Jones* (LJ) ε values for the non-bonded potentials between surfactant and mimic beads - the LJ parameters were changed so that we could produce a system which show a self-preferential phase separation to take into account the

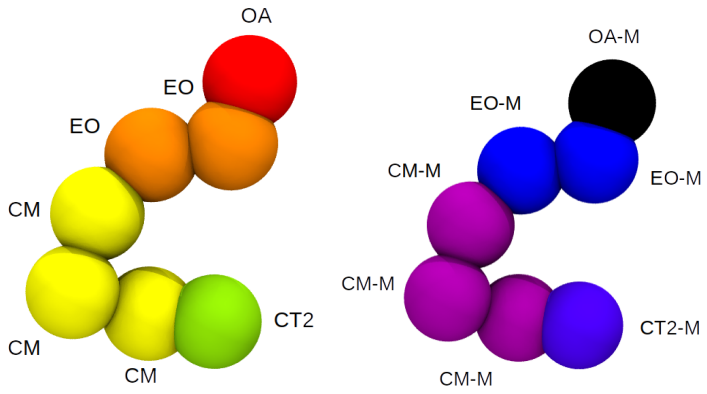

(a) (b)

Fig. 5.1 The schematic and colour scheme for the CG components of the mixed bilayer. (a) represents the unmodified polymer, $C_{12}E_2$, while (b) represents the modified polymer $C_{12}E_2$-M (c) A top view of the initial configuration of the 50:50 random mixture of $C_{12}E_2$ and $C_{12}E_2 - M$ was as the initial configuration of the bilayer (that is, before minimisation and the production run).

large variety of phase separation mechanisms which can be seen in real lipid bilayers. The tabulated values for these systems are shown in Appendix 1. The schematic for this modification is shown in Figure 5.1. The non-bonding potentials between the $C_{12}E_2$ and $C_{12}E_2$-M has been modified to show a greater extent of intermolecular repulsion between the original and mimic beads.

The non-bonded interactions between the surfactant molecules were described using a Lennard-Jones (LJ) 12-4 potential, while the non-bonded interactions between the surfactant molecules and water were described by a LJ 9-6 potential:

$$U_{LJ12-4}(r) = \frac{3\sqrt{3}\varepsilon}{2}\left[\left(\frac{\sigma}{r}\right)^{12} - \left(\frac{\sigma}{r}\right)^{4}\right] \tag{5.1a}$$

$$U_{LJ9-6}(r) = \frac{27\varepsilon}{4}\left[\left(\frac{\sigma}{r}\right)^{9} - \left(\frac{\sigma}{r}\right)^{6}\right] \tag{5.1b}$$

where ε is the well depth (the numerical factors in the prefactor are chosen such that the minimum value of the potential is $-\varepsilon$) and $U(\sigma) = 0$, following a standard Lennard-Jones

model. The intra-molecular interactions were described using a MM force field:

$$U_{\text{bond}} = k_\ell(\ell - \ell_0)^2 \tag{5.2a}$$

$$U_{\text{angle}} = k_\theta(\theta - \theta_0)^2 \tag{5.2b}$$

where k_ℓ and k_θ are the bond stretching and bending force constants and ℓ_0 and θ_0 are the equilibrium bond lengths and angles respectively. Parameters for both the bonded and non-bonded interactions are taken from parameters published by Shinoda *et al* [131] and are tabulated in Appendix 1 for completeness.

Potential Parameters for Mixed Systems

The NP-bilayer interaction for each of the CG beads of the $C_{12}E_2$/$C_{12}E_2$-M residues is identical - the modifications were implemented so that the tailgroup-tailgroup (between CM & CT2 and CM-M & CT2-M) and headgroup-headgroup (between EO & OA and EO-M & OA-M) non-bonding interactions were modified, but the other interactions were left identical to the $C_{12}E_2$ surfactant, so that the only parameter we are concerned with is the changing interaction between the amphiphiles and their modified equivalents. Therefore the main source of the line tension (γ) comes from the modification of the LJ potentials between the original and modified polymers. The modifications to the original LJ potentials to create a mixed component bilayer is illustrated in Appendix B.

Model of the NPs

The NP was treated as collection a of uniformly distributed interaction sites i.e. the particle was treated as a surface-to-molecule potential, based upon Hamaker's model for modeling the non-bonding potential of surfaces [132, 133]. To represent the hydrophobic NPs, the interaction sites of the particle took the LJ parameters of the bead type CT2; the interactions between the NP and CG beads were derived from integrating the interaction potential be-

tween a CG bead and an interaction site within the NP over the particle's volume. Assuming that the interaction between a CG bead and single interaction site can be described through the modified LJ functions above (Equations 5.1a and 5.1b) the interaction between a NP and a CG bead may be written as

$$U_{NP}^{12-4}(r,R) = \left(\frac{2\sqrt{3}\pi\rho\varepsilon\sigma^{12}R^3}{15}\right)\left(\frac{5R^6+45R^4r^2+63R^2r^4+15r^6}{(r^2-R^2)^9}\right) - \frac{3\pi\rho\varepsilon\sigma^4R}{r^2-R^2} + \frac{3\sqrt{3}\pi\rho\varepsilon\sigma^4}{2r}\ln\left[\frac{r-R}{r+R}\right]$$

$$U_{NP}^{9-6}(r,R) = 9\pi\rho\varepsilon\sigma^9R^3\frac{3R^4+42R^2r^4+35r^4}{35r(r^2-R^2)^6} - \frac{9\pi\rho\varepsilon\sigma^6R^3}{r^2-R^2}$$

where ρ is the density of the NP and R is the NP radius. The density of the NP was taken to be 1000 kg m^{-3} (based on the density of water). Full derivations of these formulae are given in Appendix 1. The parameters ε and σ are the Van der Waals parameters for the W (hydrophilic) or CM (hydrophobic) CG beads. The interaction potential between the NP and solvent bead is taken as a simple interpolation of the hydrophilic and hydrophobic potentials i.e.

$$U_{NP}^{\text{type}}(r) = (x)U_{NP}^{\text{hydrophilic}}(r) + (1-x)U_{NP}^{\text{hydrophobic}} \tag{5.1}$$

where we set x = 0 to ensure a fully hydrophobic NP. Plots of the interaction potentials of each NP are provided in Appendix 1. Three R values were used for creating the NPs - R = 1.0, 1.5 and 2.0 nm. The 1.0 nm radius NP represents a NP that is comparable to the tailgroup (CM and CT2) length of the amphiphile, while the 2.0 nm radius NP represents a NP with a width that is comparable to the thickness of the bilayer, the 1.5 nm radius being the intermediate. For each R, the hydrophobic interaction between the NP and $C_{12}E_2$/$C_{12}E_2$-M is identical.

Fig. 5.2 The colour scheme and schematic for the hydrophobic NPs we used in conjunction with the mixed bilayer.

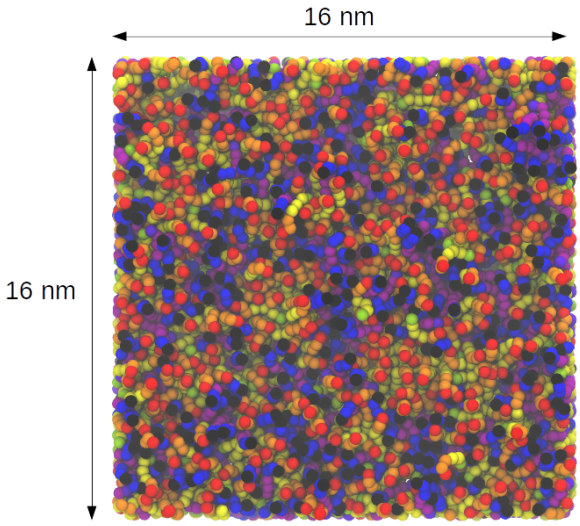

Fig. 5.3 The top-down view of the mixed bilayer system we have simulated in this system - we used a 16 $\times$ 16 nm bilayer to ensure that it was large enough to avoid size-dependent artefacts in its properties when interacting with the NP.

5.2.2 System Configuration

To generate the initial configuration of the bilayer, 2000 total residues of $C_{12}E_2$ and $C_{12}E_2$-M were randomly distributed to arrange a bilayer in a simulation box ranging from dimensions 160 Å $\times$ 160 Å $\times$ 200 Å with the rest of the box being filled with 57312 water beads. This system was equilibrated using a *NVT* ensemble for 1 ns simulation time with increasing timesteps (from 0.01 fs to 10 fs) to ensure that the overlaps between molecules were resolved and to ensure that the system did not fluctuate substantially. This system was subsequently subjected to 1 ns of *NVT* equilibration, with a timestep of 10 fs. The *NVT* equilbration was kept relatively short to ensure that a significant extent of phase separation did not occur during that period.

NP Insertion inside the Bilayer

To insert the NP, initially the CG water beads were removed within the simulation box. The distance in the direction normal to the bilayer (z-direction) was set to range from 100 Å to -100 Å, with the bilayer center being located at z = 0 Å. The NP was inserted into the system 50 Å above the center of mass of the bilayer followed by re-solvation (randomly allocating the same number of water beads in the box dimensions defined before). The system was simulated in the *NPT*-ensemble, to ensure that the area per lipid was flexible, with temperature and pressure set to 303 K and 1 atm respectively. The temperature and pressure were controlled using a Nose-Hoover thermostat and barostat[134–136], both with relaxation times of 0.2 ps. The equations of motion were integrated using the rRESPA multiple-timestep algorithm [137] with a 2.0 fs inner (bonded) and 10.0 fs (non-bonded) outer timesteps. Non-bonded interactions were truncated at r_{cut} = 15 Å. Periodic Boundary Conditions (PBCs) were set in the x and y directions.

Mixed Component Bilayers with and without NPs

Each NP-free system was initialised in an NVT ensemble at 303 K for 0.5 ns. Subsequently, an NPT production run was simulated at 303 K and 1 atm for approximately 1 μs for each simulation, to ensure that each system comes as close as possible to full phase separation. When setting the analogous NP-bilayer systems, each NP example (R = 1.0, 1.5 and 2.0 nm , where R = radius) hydrophobic NP was placed approximately 30 Å above the bilayer surface during the equilbration step. The R = 1.0 nm size chosen for the NP encompasses the tailgroup region of the bilayer, while the R = 2.0 nm is similar to the entire bilayer thickness. Two types of NP simulations were done for each radius - one with the NP embedded inside the bilayer without a restraining potential, and one with the potential. In addition, as a benchmark to the effects of a multicomponent bilayer, a monocomponent bilayer with each NP was simulated under the identical conditions for the mixed bilayer simulations. For each simulation, we simulated for approximately 1 μs to analyse if we can identify similar phenomena to the mixed bilayer examples. We have used the *Midplus*, *Tinis* and *Apocrita* [169, 170] clusters generously provided from the University of Warwick and Queen Mary University of London to undertake the simulations in this work. The catalogue of simulations for this work is illustrated in table 5.1.

5.3 Analysis of the Bilayers

5.3.1 Cluster Formation Analysis

To analyse the effect of the hydrophobic NP on the rate of phase separation, we implemented a *nearest-neighbour* clustering algorithm, which measures the aggregation of identical types of surfactants within Å radius around the $C_{12}E_2$ and $C_{12}E_2$-M component. The analysis was implemented for the NP-absent/NP systems - where the NP-absent system can act as the

Index	NP Radius	System Type	Simulation Length
1	-	Mixed	1 μs
2	1.0	Mixed	1 μs
3	1.5	Mixed	1 μs
4	2.0	Mixed	1 μs
5	1.0	Mixed-spring	1 μs
6	1.5	Mixed-spring	1 μs
7	2.0	Mixed-spring	1 μs
8	1.0	Mono	1 μs
9	1.5	Mono	1 μs
10	2.0	Mono	1 μs

Table 5.1 The simulations allocated for this work. The grey coded rows indicate the NP absent control experiments, while the cyan lists show the simulations including the NPs.

benchmark system to the NP-present system, where the key difference (if any) we want to observe is how the presence of a NP affects the rate of phase separation. Where the system has a NP, we have the NP at z = 0 Å (i.e. in the bilayer normal) using an umbrella spring potential, whilst keeping the degrees of freedom in the x and y direction free to ensure the NP can diffuse around in the bilayer. To calculate the rate of phase separation and the size of clusters, the distance between a surfactant and it's neighbours was defined between the center of mass (COM) of each surfactant - if the number of identical type ($C_{12}E_2$ or $C_{12}E_2$-M) was detected within a r = 10 Å distance, then we increment the 'cluster' counter. This cluster counter was averaged over the total number of $C_{12}E_2$/$C_{12}E_2$-M respectively, and measured over the course of the simulation.

5.3.2 Membrane Domain and Budding Energetics

We have approached the problem of membrane energetics in the way as described by Wolff *et al* [171] and Lipowsky [172–174], which involves dividing up the bending, interface and composition energetics, following on from the elastic properties of a bilayer described by Helfrich [175]. The approach entails dividing up the bilayer conformation around the domain and the NP in terms of the bending energy (the cost of increasing the curvature around

the NP), the edge energy (the unfavourable energetic contribution between the domains) and the adhesion energy (the energetic cost of adhering on the NP surface). The bending energy term is defined by:

$$E_{\text{bending}} = 2\pi L^2 \kappa \left[(C - C_0)^2 + (C + C_0)^2 \right] \tag{5.2}$$

Where κ is the bending rigidity, L is the radius of the dimple/cap, C is the curvature of the dimple/cap, and C_0 the spontaneous curvature of the bilayer. Here, we can estimate the curvature as $\frac{1}{R}$, if we assume that the center of the NP position is aligned with the peak of the cap/micelle. The energetic cost of forming the edge also needs to be taken into account - the domain edge energy can be defined as:

$$E_{\text{edge}} = 2\pi L \gamma \sqrt{1 - (LC/2)^2} \tag{5.3}$$

where γ indicates the line tension. To measure γ, it is required to measure the unfavourable interaction forces at the phase interface - originating from the difference in intermolecular potentials and/or structural variations. To infer γ, we have extracted the stress tensor components for each CG bead of the $C_{12}E_2$ and $C_{12}E_2$-M components and averaged them over the intra-planar axes i.e. the x and y axes. This is extracted from the stress tensor components from the molecules in the system. For every atom in the system, the stress tensor in the simulation (described in detail in the LAMMPS manual [112]) is given by the following

equation:

$$\text{Stress}_{ab} = -\Bigg[\overbrace{mv_a v_b}^{A} + \overbrace{\frac{1}{2}\sum_{n=1}^{N_p}(r_{1_a}F_{1_b} + r_{2_a}F_{2ty_b})}^{B} + \overbrace{\frac{1}{2}\sum_{n=1}^{N_b}(r_{1_a}F_{1_b} + r_{2_a}F_{2_b})}^{C}$$
$$+ \overbrace{\frac{1}{3}\sum_{n=1}^{N_a}(r_{1a}F_{1_b} + r_{2_a}F_{2_b} + r_{3_a}F_{3_b})}^{D} + \overbrace{\frac{1}{4}\sum_{n=1}^{N_d}(r_{1_a}F_{1_b} + r_{2_a}F_{2_b} + r_{3_a}F_{2_b} + r_{4_a}F_{4_b})}^{E}$$
$$+ \overbrace{\frac{1}{4}\sum_{n=1}^{N_i}(r_{1_a}F_{1_b} + r_{2_a}F_{2_b} + r_{3_a}F_{2_b} + r_{4_a}F_{4_b})}^{F} + \overbrace{\text{Kspace}(r_{i_a}, F_{i_b})}^{G} + \overbrace{\sum_{n=1}^{N_f} r_{i_a}F_{i_b}}^{H}\Bigg] \tag{5.4}$$

where a and b take the axis values (x, y, z) to generate the 6 components of the stress tensor, r_1 and r_1 are the positions of the two atoms when taking into account pairwise interactions, F_1 and F_2 represent the forces on the two atoms involved in the expression. Term A is the kinetic energy term, term B is the pairwise energy contribution, terms C, D, E and F are the bond, angle, dihedral, and improper contributions, term G represents the reciprocal lattice contribution to the coulombic term, and term H refers to the constraint forces on the molecule. To estimate γ, we computed the stress component across the x and y planes (term B) and this was lock-averaged across the axes at every Å interval - hence, over 180 Å. The axes components (xx, yy, zz, xy, xz, yz) where we identify the most significant discrepancy near the domain boundary is identified as our estimate of γ. This value was also measured for simulations with NPs to identify how the presence of the NP affects the γ between the phase separated domains.

For our estimate of the bending modulus, we extracted the observed experimental bending moduli as the estimate - for $C_{12}E_2$, this was reported as 5.4 k_BT [176]. As we have simply modified the VdW parameters between the $C_{12}E_2$ and $C_{12}E_2$-M components, we

have used this value of bending moduli for the bending modulus of the bilayer. The adsorption/adhesion energy $E_{adhesion}$ of the surfactants to the NP surface, as estimated by Bahrami *et al* [177] is calculated as:

$$E_{\text{adhesion}} = -4\pi R^2 U x \tag{5.5}$$

where U $\geq$ 0 is the adhesion energy per unit area, and x is the fraction of the NP area that is wrapped by the surfactant. Here, we have measured the interaction energy of the $C_{12}E_2$ and $C_{12}E_2$-M components with the NP surface. The sum of the interaction forces in the x, y and z axes can be estimated as the $E_{adhesion}$, which in turn can be used to infer U. A negative $E_{adhesion}$ is responsible for the formation of the micelle/bud, while $E_{bending}$ and E_{edge} are the equivalent to the energetic cost required.

In addition to the interaction of the surfactant components with the NP, it is necessary to measure the influence from the bilayer composition around the NP. The spontaneous curvature of the $C_{12}E_2$ bilayer was used for the bilayer energetics calculation and modified accordingly depending on a local composition. Initially, from the lateral pressure profile, $\pi(z) = P_L(z) - P_N(z)$, the first integral moment of the lateral pressure profile (τ_1^m) is calculated as:

$$\tau_1^m = \int_0^h z\pi(z)dz \tag{5.6}$$

where z = 0 at the center of the bilayer and z = h in the water phase. From this, the spontaneous curvature, C_0, was calculated as:

$$C_0 = \frac{\tau_1^m}{\kappa_m} \tag{5.7}$$

where κ_m is the monolayer bending modulus, which is defined as $\kappa_m = \kappa_b/2$, i.e. approximately 2.7 k_BT. Hence, the primary values to compute in this work are the spontaneous curvature of the bilayer, the curvature around the NP, and τ.

Composition Analysis around the NPs

Wolff *et al* [171] estimated the 'incompatibility' energy (or the measure of the tendency of each bilayer component to disaggregate) from the Landau expansion of the monolayer composition, which is highly dependent on the monolayer compositions of the bilayer, which in turn affects the magnitude of the spontaneous curvature. A flat bilayer domain may become spontaneously curved whenever an excess of a single lipid component is highly concentrated in a patch of the monolayer. Here, the exact composition energy is difficult to extract, as the interaction energy near the domain region cannot be easily extracted, and while the interaction energy between the $C_{12}E_2$ and $C_{12}E_2$-M can be computed, this does not guarantee its relevance as the incompatibility energy. Instead, following the convention followed by Wolff, we have calculated monolayer compositions ϕ_1 and ϕ_2 (indices 1 and 2 representing each monolayer) around the NP in a 15 Å radius around the NP, to modify the composition dependent spontaneous curvature:

$$\phi_1 = \phi_1^{C_{12}E_2} - \phi_1^{C_{12}E_2-M} \tag{5.8}$$

$$\phi_2 = \phi_2^{C_{12}E_2} - \phi_2^{C_{12}E_2-M} \tag{5.9}$$

Each of the monolayer compositions around the NP region was analysed to measure how the interaction of the surfactants of the bilayer affected the local compositions around the NP. The list of possible $C_{12}E_2$/$C_{12}E_2$-M with the NP is shown in Figure 5.4. Hence, by analysing this composition data, we can estimate the extent during incompatibility near the NP region, and the 'lifetime' which this 'incompatible' conformation remains around the NP.

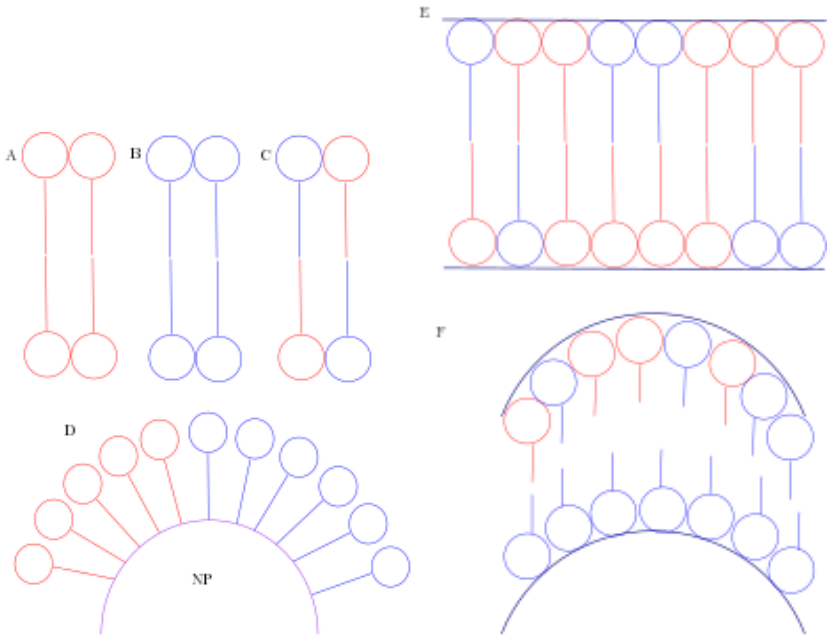

Fig. 5.4 The surfactant conformations with the different energetic penalties. A and B are equivalent in this case, while C shows the mismatch between the $C_{12}E_2$ and $C_{12}E_2$-M (the red and blue species respectively) which is unfavourable in both the lateral and normal plane of the bilayer. D shows a slice of the NP surface where the $C_{12}E_2$ and $C_{12}E_2$-M species are adsorbed. E shows the scenario where the top and bottom monolayer are well-mixed, which is equivalent to the top (1) and bottom (2) monolayer composition being equal ($\phi_1 \sim \phi_2$), while F shows the case where the one monolayer is significantly more domain-like ($\phi_1 \neq \phi_2$).

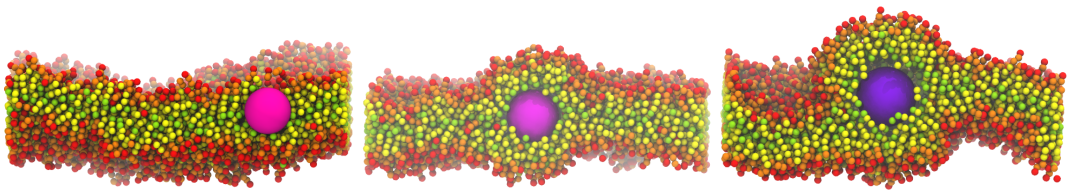

(a) (b) (c)

Fig. 5.5 Monocomponent bilayer with hydrophobic NPs - (a), (b) and (c) show the snapshots after 1 μs simulations for the R = 1.0, 1.5 and 2.0 nm NPs respectively.

Voronoi Analysis - Area per Surfactant and Thickness

We have used the *voronoi tesselation* method to visualise the change in the area per lipid and thickness of the bilayer. The *APLVORO* program [178] was used to calculate the effect of phase separation on each components. The voronoi cell corresponding to changes in length and area was plotted to observe the effect of the NP in the interface of the phases. The voronoi method allows the effective measurement of the area and thickness per lipid in a multicomponent bilayer by proportional allocation of space for the point on the xy plane.

5.4 Results and Discussion

5.4.1 Control Simulations with the Monocomponent Bilayers

Figure 5.5 (a), (b) and (c) show the snapshots of the pure $C_{12}E_2$ with the R = 1.0, 1.5 and 2.0 nm radius simulations respectively. We have observed that in these cases, the NPs remain within the hydrophobic interior of the bilayer. We did not observe any significant budding or fission processes with the monolayer, which was consistent with the results we have seen with Chapter 4.

5.4.2 Mixed Bilayer Systems with/without the NPs

The mixed bilayer system without the NP is shown in Figure 5.6. We see that significant phase separation occurs after 800 ns. We also see an increase in the curvature of the bilayer corresponding to a greater phase separation. The analogous simulations with the hydrophobic NPs for R = 1.0, 1.5 and 2.0 nm are shown in Figures 5.7, 5.8 and 5.9. With the entry of the NP into the bilayer center we see the formation of a cap for the R = 1.0 nm example, and a full budding/micelle formation in the case of the R = 2.0 nm example. The R = 1.5 nm shows the intermediate case, showing the formation of a significant cap around the NP. By measuring the the density of each type of surfactant around the NP, we can measure the dynamic change in the conformation of the cap/bud. Figures 5.10, 5.11 and 5.12 show the RDF profiles of the $C_{12}E_2$ and $C_{12}E_2$-M components around each NP. For all the NP samples, we see a direction of change in the density profile, where a decrease in the $C_{12}E_2$ peaks corresponds to a $C_{12}E_2$-M peaks within 20 Å of the NP surface, which suggests a dynamic change of the surfactant conformations on the NP surface. From distances of 40 Å to 100 Å, we observe a significant trough forming which is most exaggerated in the case of the R = 2.0 nm, which corresponds to the budding of the NP.

5.4.3 Measuring the Phase Separation

Figure 5.14 shows our measurements of the average cluster sizes, as a function of time for the NP-free and NP present systems involved, of the $C_{12}E_2$/$C_{12}E_2$-M components. From it, we do not observe a significant increase/decrease in the rate of phase separation, which would suggest that the effect of a single hydrophobic NP in the system does not indicate a significant effect on the rate of phase separation.However, we can still observe the diffusion of the NPs the the domain interface, which suggests that it behaves as a lineactant, and hence we cannot rule out its effect as a rate inhibitor for phase separation.

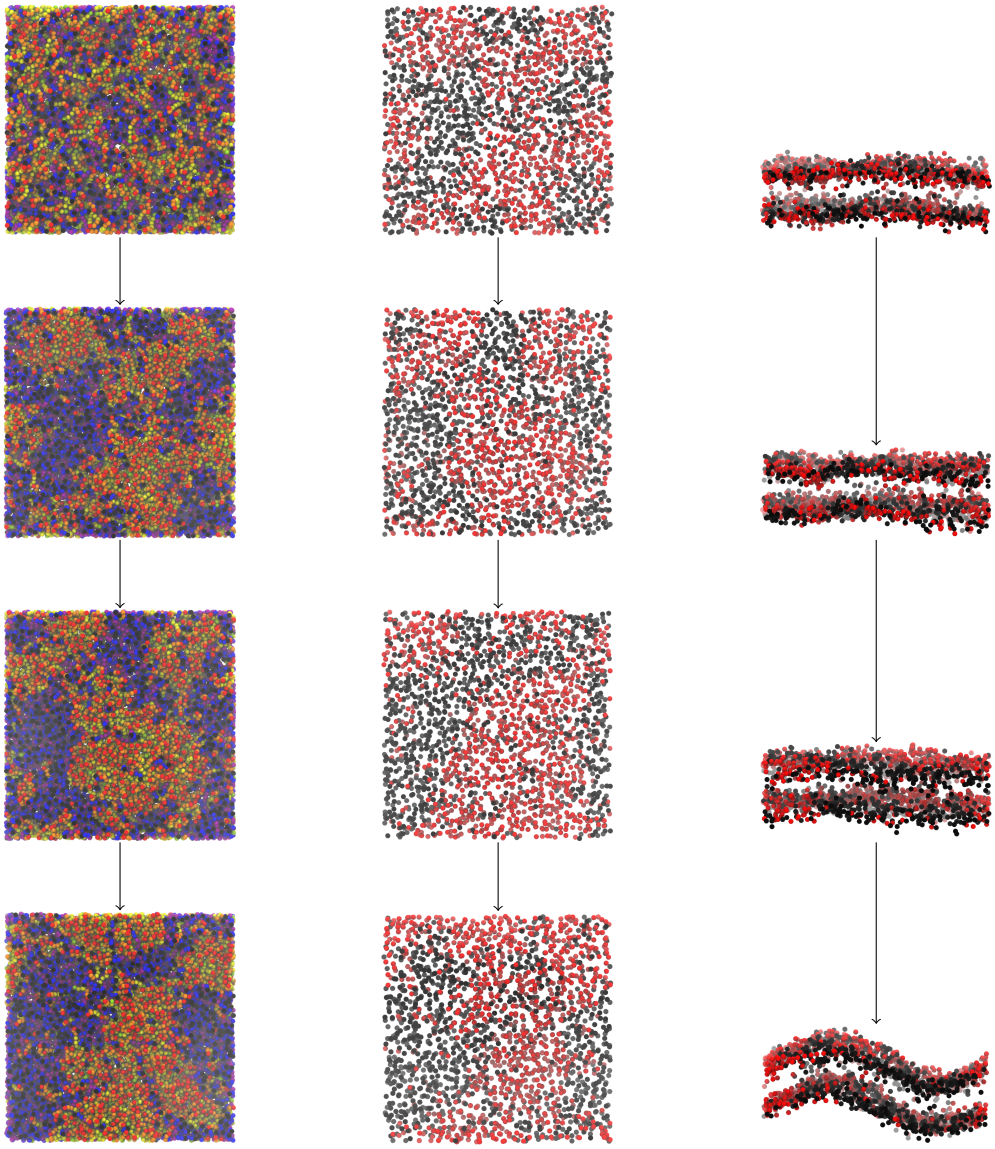

Fig. 5.6 The time evolution of the mixed bilayer over 1 μs. (a) shows the top-down view of the simulation, while (b) and (c) represents the stripped top down and side snapshots.

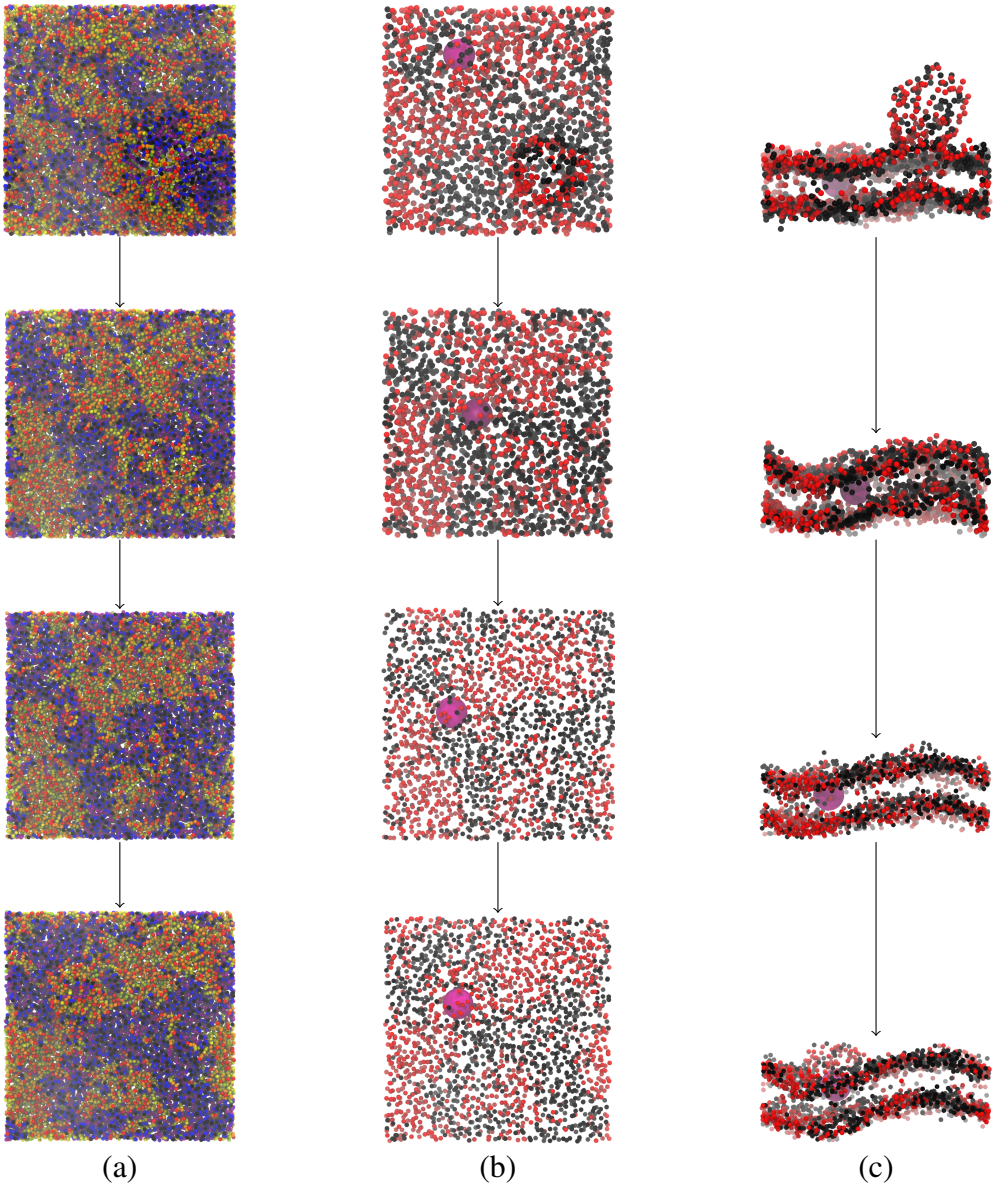

Fig. 5.7 The time evolution of the mixed bilayer with a $R = 1.0$ hydrophobic nm NP over 1 μs. (a) shows the top-down view of the simulation, while (b) and (c) represents the stripped top down and side snapshots, to illustrate the position of the NP inside the bilayer

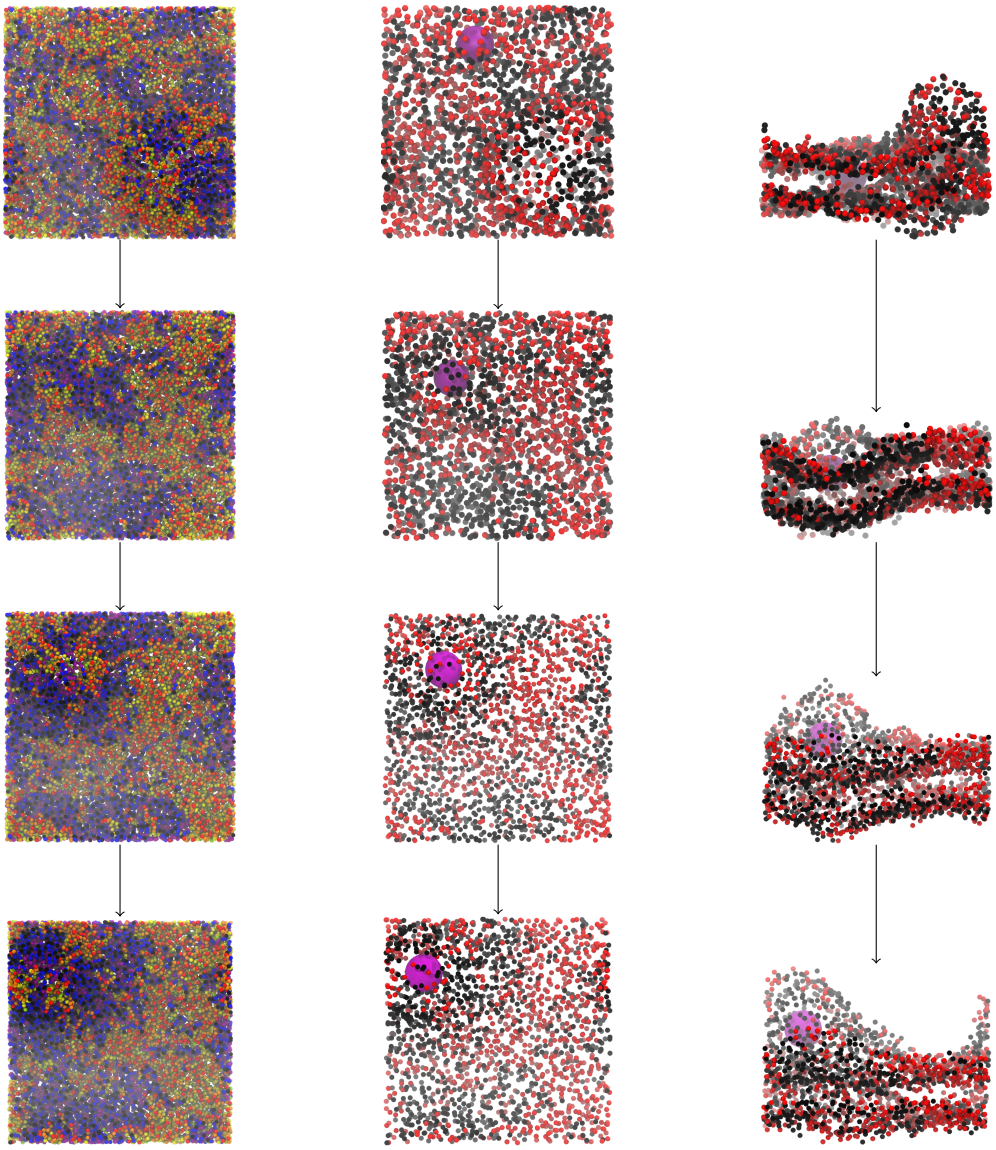

Fig. 5.8 The time evolution of the mixed bilayer with a $R = 1.5$ nm hydrophobic NP over 1 μs. (a) shows the top-down view of the simulation, while (b) and (c) represents the stripped top down and side snapshots, to illustrate the position of the NP inside the bilayer.

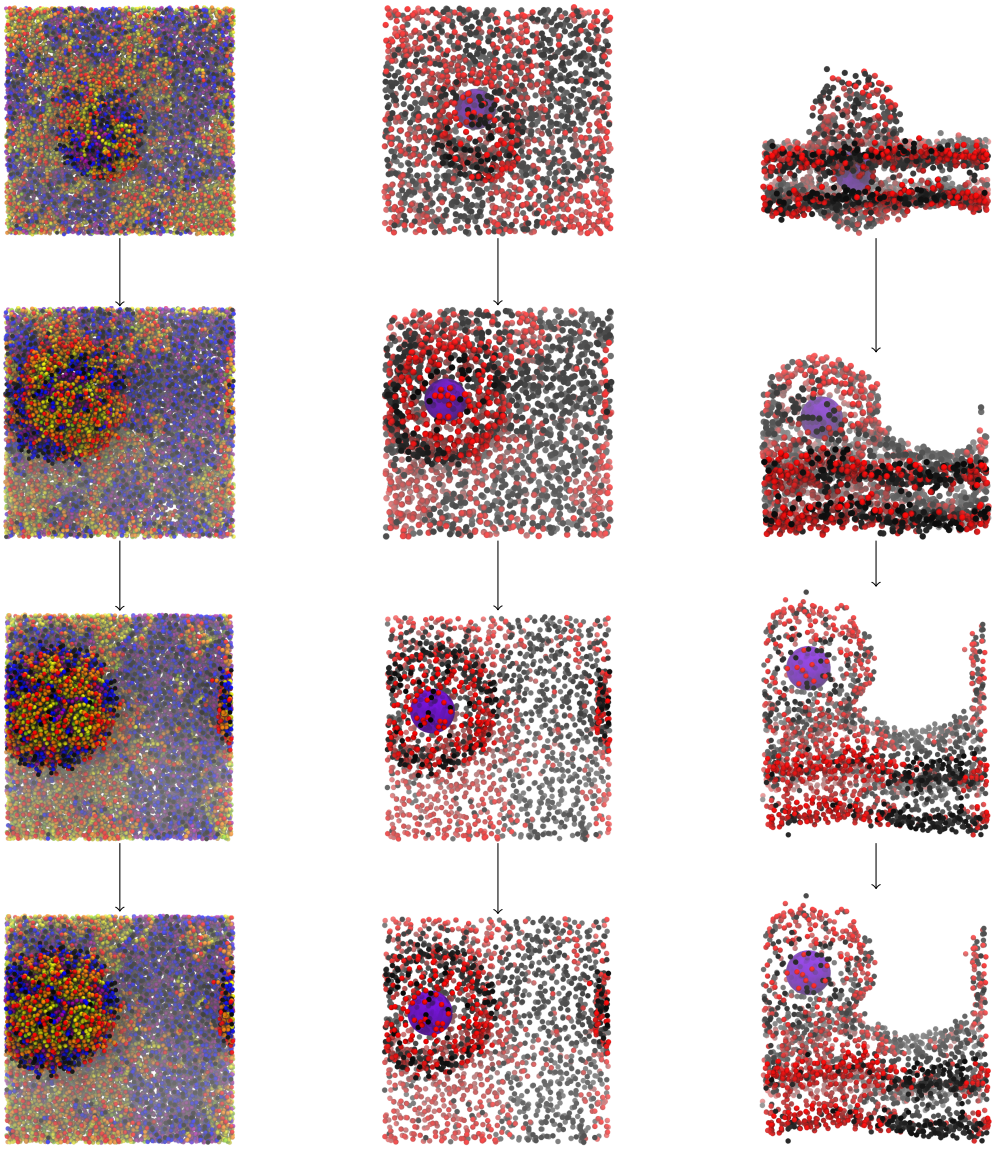

Fig. 5.9 The time evolution of the mixed bilayer with a $R = 2.0$ nm hydrophobic NP over 1 μs. (a) shows the top-down view of the simulation, while (b) and (c) represents the stripped top down and side snapshots, to illustrate the position of the NP inside the bilayer.

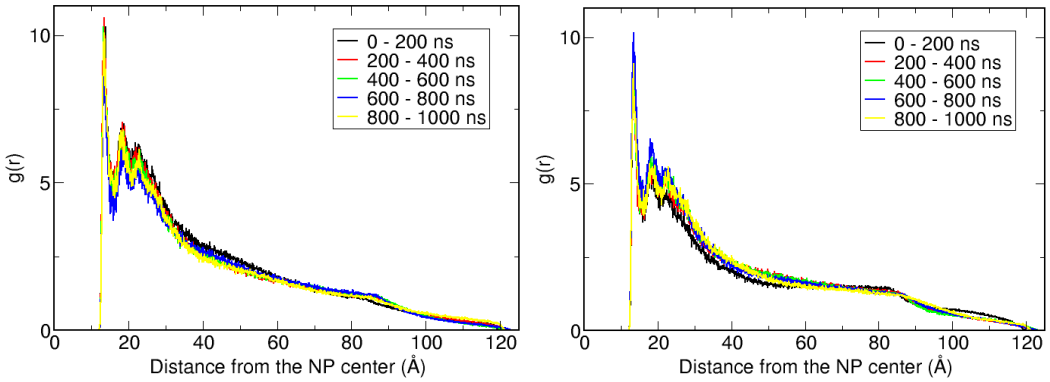

Fig. 5.10 The radial distribution profile (RDF) around the R = 1.0 nm hydrophobic NP, averaged over 200 ns increments for the $C_{12}E_2$ and $C_{12}E_2$-M components around the NP, illustrated the structural change around the NP as a function of time. (a) show the distribution of $C_{12}E_2$, while (b) shows the distribution of $C_{12}E_2$-M.

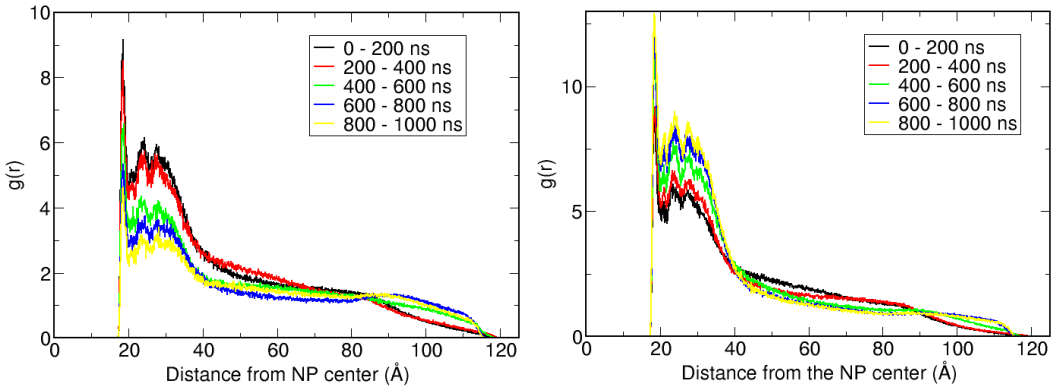

Fig. 5.11 The radial distribution profile (RDF) around the R = 1.5 nm hydrophobic NP, averaged over 200 ns increments for the $C_{12}E_2$ and $C_{12}E_2$-M components around the NP, illustrated the structural change around the NP as a function of time. (a) show the distribution of $C_{12}E_2$, while (b) shows the distribution of $C_{12}E_2$-M.

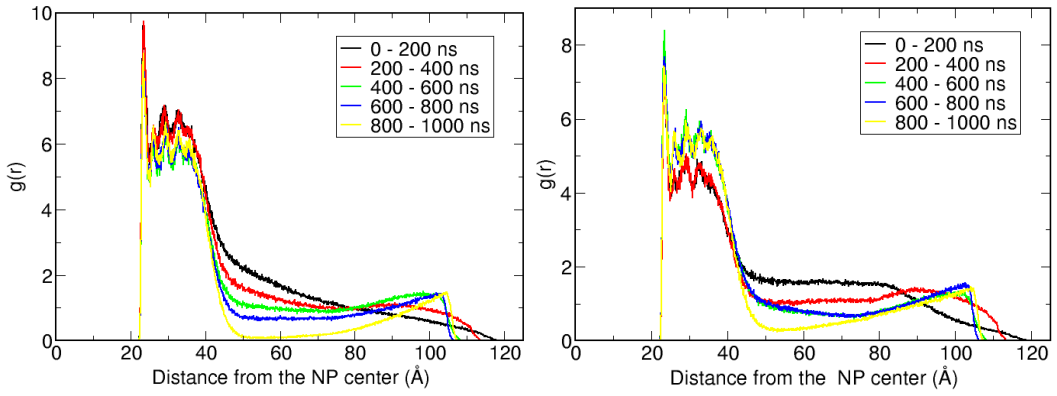

(a) (b)

Fig. 5.12 The radial distribution profile (RDF) around the R = 2.0 nm hydrophobic NP, averaged over 200 ns increments for the $C_{12}E_2$ and $C_{12}E_2$-M components around the NP, illustrated the structural change around the NP as a function of time. (a) show the distribution of $C_{12}E_2$, while (b) shows the distribution of $C_{12}E_2$-M.

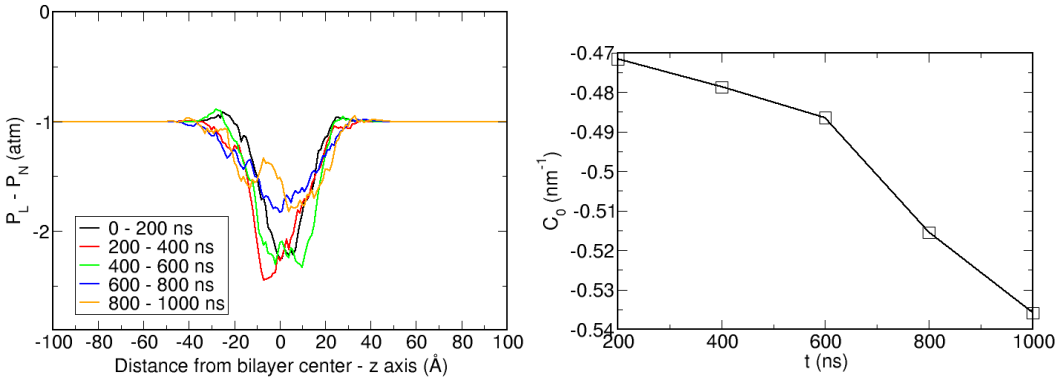

(a) (b)

Fig. 5.13 (a) shows the averaged lateral pressure profiles for the $C_{12}E_2$/$C_{12}E_2$-M mixed bilayer in 200 ns intervals over 1 µs. The pressure profiles were used to infer the change and convergence of the spontaneous curvature of the bilayer. (b) shows the corresponding spontaneous curvature.

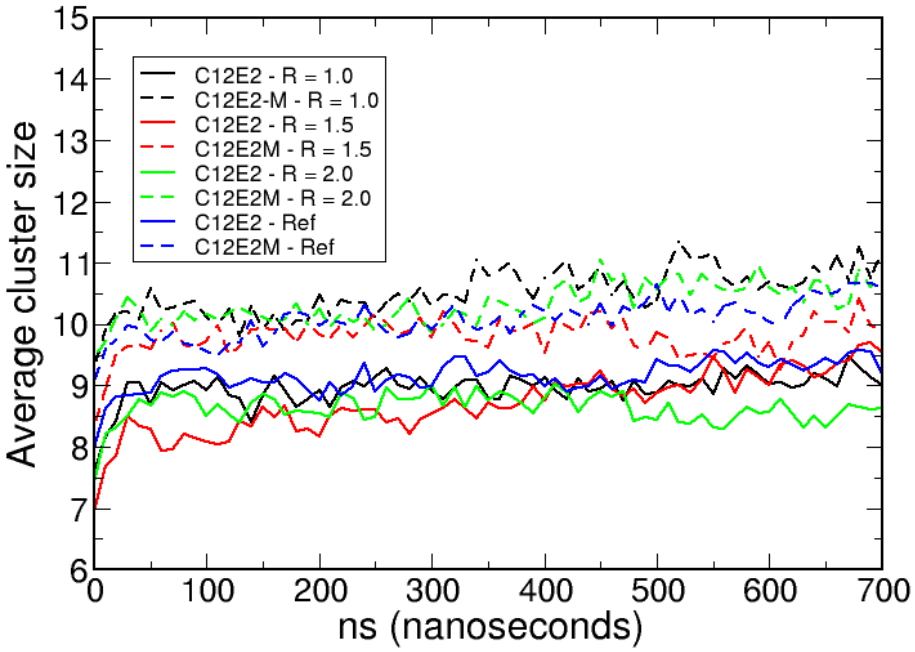

Fig. 5.14 Analysis of cluster formation for the $C_{12}E_2$ and $C_{12}E_2$-M components with each NP sizes, and the reference system with no NP present as a control.

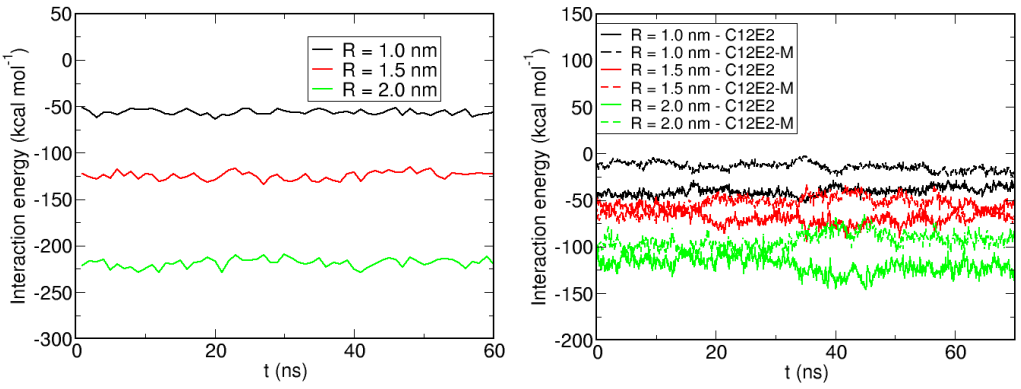

(a) (b)

Fig. 5.15 (a) shows the interaction energy between each hydrophobic NP and a mono-component $C_{12}E_2$ bilayer, while (b) shows the interaction energy between each NP and the $C_{12}E_2$/$C_{12}E_2$ components for the last 70 ns of the 1 μs simulations.

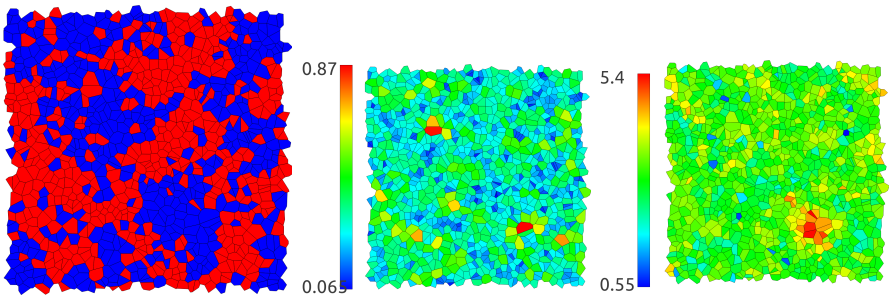

(a) (b) (c)

Fig. 5.16 The voronoi analysis of the snapshot at 1 μs of the $R = 1.0$ nm NP simulation with the mixed bilayer - for each voronoi cell, the type, area and length of the cell was illustrated in (a), (b) and (c) respectively.

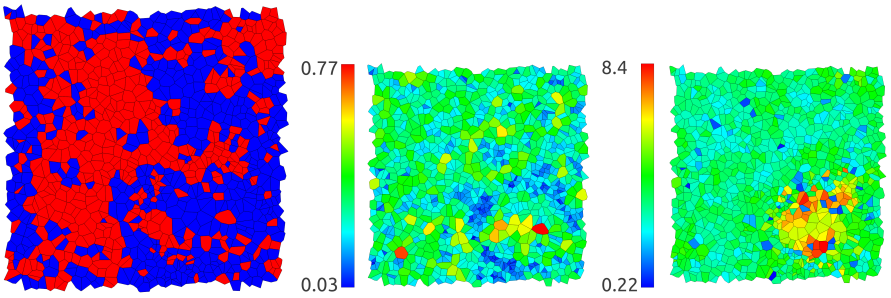

(a) (b) (c)

Fig. 5.17 The voronoi analysis of the snapshot at 1 μs of the $R = 1.5$ nm NP simulation with the mixed bilayer - for each voronoi cell, the type, area and length of the cell was illustrated in (a), (b) and (c) respectively.

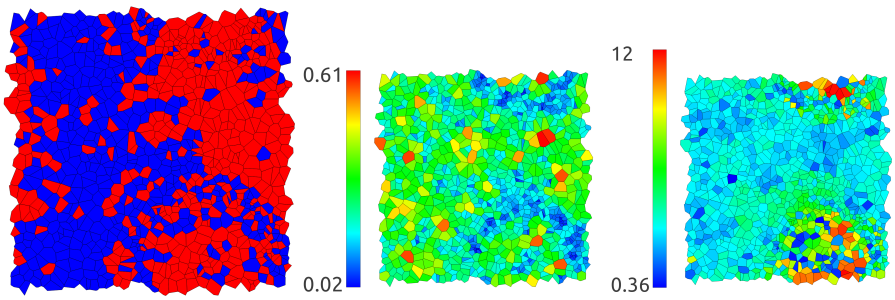

(a) (b) (c)

Fig. 5.18 The voronoi analysis of the snapshot at 1 μs of the $R = 2.0$ nm NP simulation with the mixed bilayer - for each voronoi cell, the type, area and length of the cell was illustrated in (a), (b) and (c) respectively.

From the voronoi illustration for the R = 1.0, 1.5 and 2.0 nm (Figures 5.16, 5.17 and 5.18 respectively), we observe that in general, the length of the the surfactants in the region of the core of the NP is increased. For the larger NPs (R = 1.5 and 2.0 nm), we observe also a decrease in the area per lipid around the NP region - an area per lipid of 0.03 nm^2 and 0.02 nm^2 is observed in this ring for the R = 1.5 and 2.0 nm respectively. This constrained area per lipid around the larger NPs would suggest that the larger surface area of the NP allows a local ordering of the surfactant components around it.

Membrane Budding and Micelle Formation - the Interaction between the Domain Boundary and the NPs

From the stress tensor measurements (Figure 5.19) from a mixed bilayer simulation with clear domain boundaries, we can see the fluctuation and range of values of the γ. The averaged value for γ for the length of the domain interface is in the range of 1.0-7.0 $\times$ 10^{-10} N over 1000 ns, as measured from the absolute difference in the γ values near the domain boundaries. Experimental measurements of γ range in the region of 0.2-6.2 $\times$ 10^{-12} J m^{-1} (0.2-6.2 $\times$ 10^{-12} N) [159, 179, 180], which shows that the mixed bilayer showed in this simulation has γ values comparable to experimental systems. Lipowsky [172] computed a crude estimate of γ as 10^{-17} Jμm^{-1} = 10^{-11} N. Simulation studies by Rosetti *et al* [165] measured a γ values in the range of 28-32 pN (2.8-3.2 $\times$ 10^{-11} N) in the domain boundaries between DAPC and DPPC. This value is notably higher than the estimates seen in the mentioned literature values, which is consistent with the rapid phase separation we induced in this system. However, we believe that this estimate is also close enough in range to the measured values such that we can make comparable analyses and measurements. Clearly, the effect of the hydrophobic NPs is such that it introduces a surface that allows the surfactant components to reorganise itself to create a domain interface *around* it, as shown by the gradual increase of the RDF plots of the $C_{12}E_2$/$C_{12}E_2$-M as a function of time. (Figures

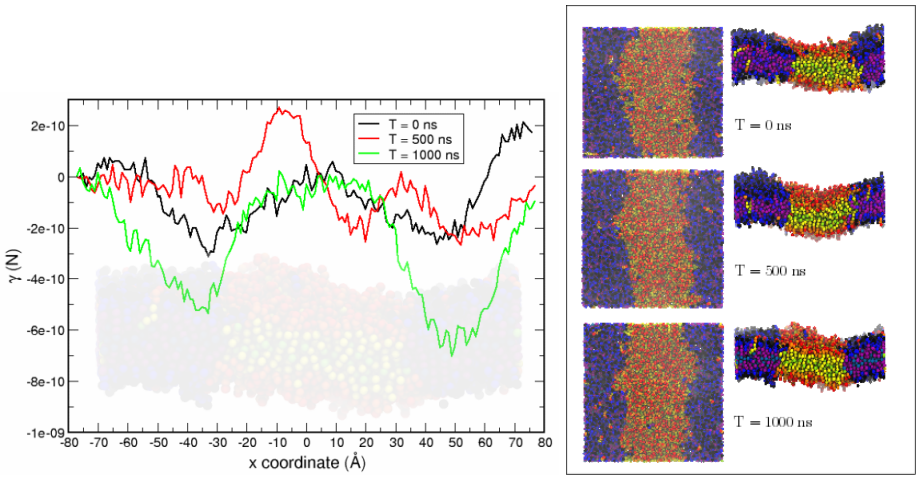

(a) (b)

Fig. 5.19 Line tension (γ) measurements on a mixed bilayer of $C_{12}E_2$/$C_{12}E_2$-M binary mixture over 1000 ns. (a) shows the line tension calculation with the averaged stress tensor components over unit length measurements at 0, 500 and 1000 ns, while (b) shows the top-down and side views of the simulations snapshots at 0, 500 and 1000 ns.

5.10, 5.11 and 5.12). If we break down the influence of the hydrophobic NP upon a mixed bilayer, the locational preference of the NP near the domain interface indicates that it is a line-active component, and hence, reflects a local reduction of γ.

The spontaneous curvature as a function of time for the mixed bilayer with no NP is shown in Figure 5.13, where (a) shows the change in lateral pressure profile shown as a function of time and (b) showing the change. We see that spontaneous curvature ranges from -0.47 to -0.54 nm^{-1} as the system evolves - i.e the magnitude of the spontaneous curvature increases with greater phase separation, which is clear from Figure 5.6. With calculations that included the spontaneous curvature (the $E_{bending}$), we have used the value of -0.47 which corresponds to the well mixed portion of the mixed bilayer simulation, and minimises the effects of the phase separation. Taking the center of the NP in each simulation as the cap/bud center, we can estimate the curvature C as $\frac{1}{2.8nm}$, $\frac{1}{3.3nm}$ and $\frac{1}{3.8nm}$ for the R = 1.0, 1.5 and 2.0 nm NPs respectively, which is equivalent to 0.357 nm^{-1}, 0.303 nm^{-1} and

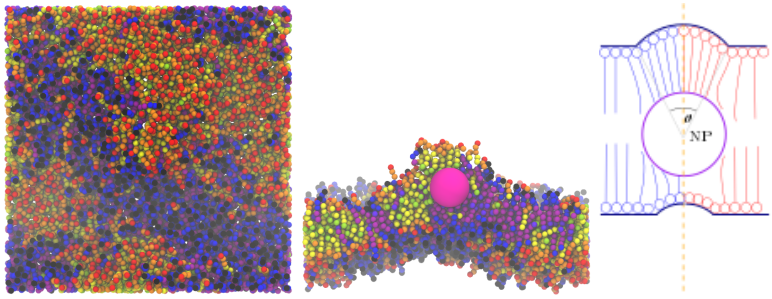

(a) (b) (c)

Fig. 5.20 The snapshot of the $R = 1.0$ nm NP simulation with the mixed bilayer, at the end of the 1 μs of simulation time. (a) and (b) show the top-down and side snapshots of the bilayer, while (c) shows the schematic of the snapshot. The angle θ refers to the angle between the circumference edge of the bulge and the center of the NP, which is used to calculate the curvature.

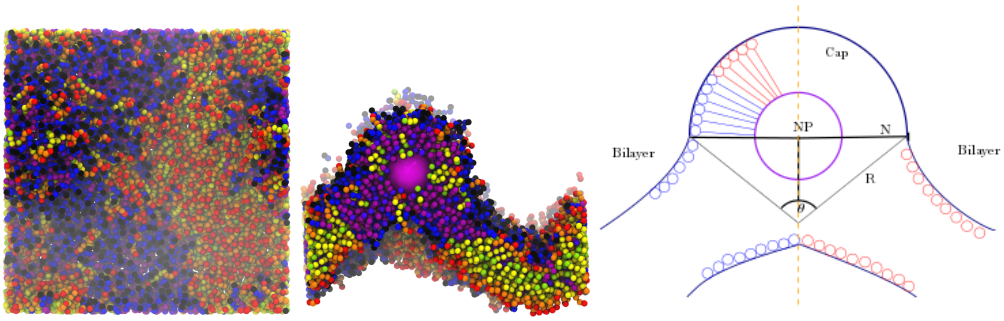

(a) (b) (c)

Fig. 5.21 The snapshot of the $R = 1.5$ nm NP simulation with the mixed bilayer, at the end of the 1 μs of simulation time. (a) and (b) show the top-down and side snapshots of the bilayer, while (c) shows the schematic of the snapshot. The length R is used to approximate the radius of the bud, of which the inverse (R^{-1}) is used as the curvature of the bud.

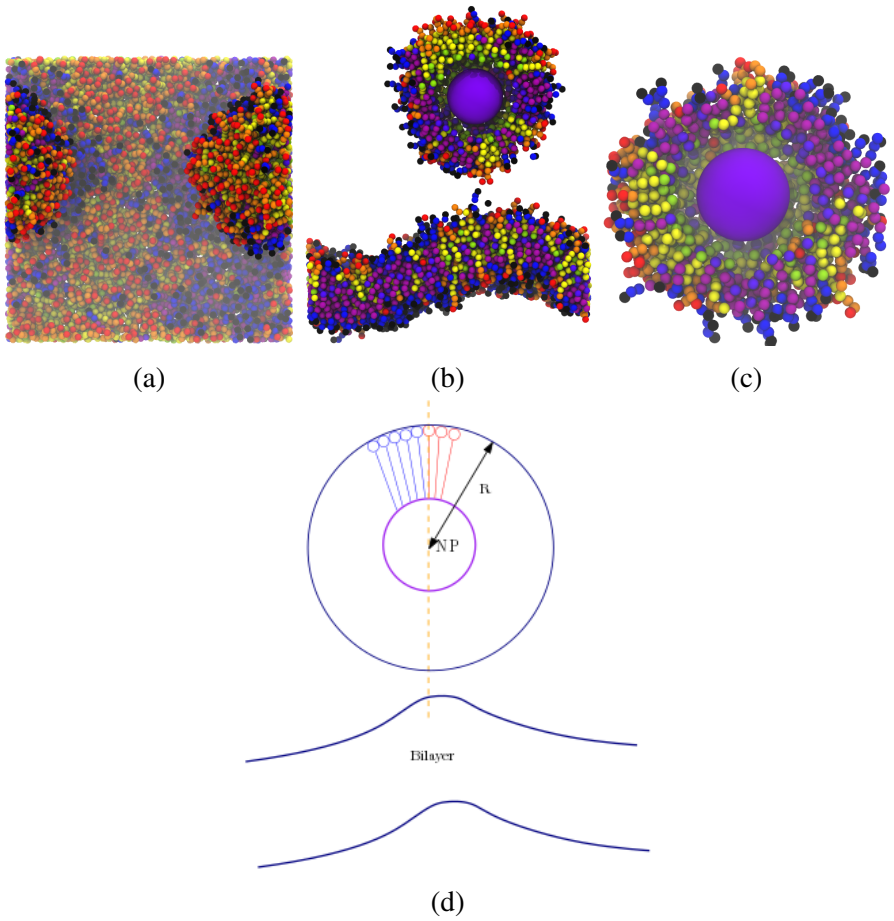

Fig. 5.22 The snapshot of the R = 2.0 nm NP simulation with the mixed bilayer, after 1 μs of simulation time. (a) and (b) show the top-down and side snapshots of the bilayer, (c) shows the NP-micelle, while (d) shows the schematic of the snapshot. The micelle radius R was calculated as the radius of the NP with the length of the surfactant on the surface, which was then used to calculate the estimated curvature of the initial bud and the micelle itself.

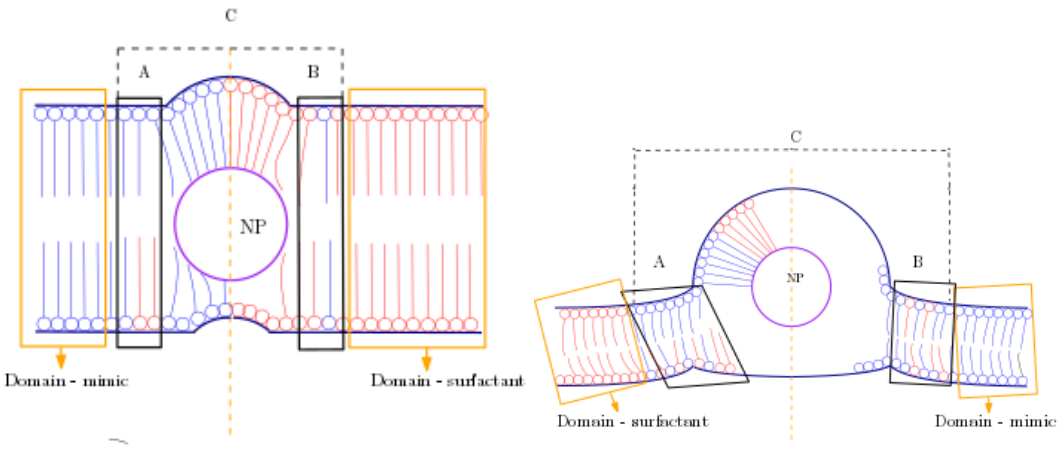

(a) (b)

Fig. 5.23 Schematics showing the capping/budding region of the 1.0 nm NP (a) and 1.5/2.0 nm NP (b) respectively. In each case, regions A and B illustrate the regions where there a high spontaneous curvature, due to the unsymmetrical coupling between the top and bottom monolayers. Region C shows the radius where the FF of the NP acts, and hence, the region where γ is reduced; this reduced γ allows the dynamic rearrangement of the $C_{12}E_2$ and $C_{12}E_2$-M components, which in turn drives the greater spontaneous curvature. The regions illustrated in orange show the bulk domains unaffected by the NP.

0.2 nm^{-1} respectively - the schematic for this estimate are shown in Figures 5.20, 5.21 and 5.22 respectively.

The membrane budding model suggested by Lipowsky [172] showed that the competition between the γ and the membrane bending energy results to a transition to either a partial or complete budding state. It has been hypothesised that once the domain region exceeds a critical size, the domain can transition into a dimpled or fully budded state, or in other words, become unstable and hence undergo a invagination process driven primarily by the fluctuation in the bilayer curvature caused by changes in temperature. In our simulations, we observe dimpled states of differing magnitudes with the R = 1.0 and 1.5 nm NP, and a fully budded state with the R = 2.0 nm NP example. As the NPs become larger, the budding becomes much more significant, which would suggest that this effect would also occur with large, rigid clusters of hydrophobic NPs, which has been observed as common

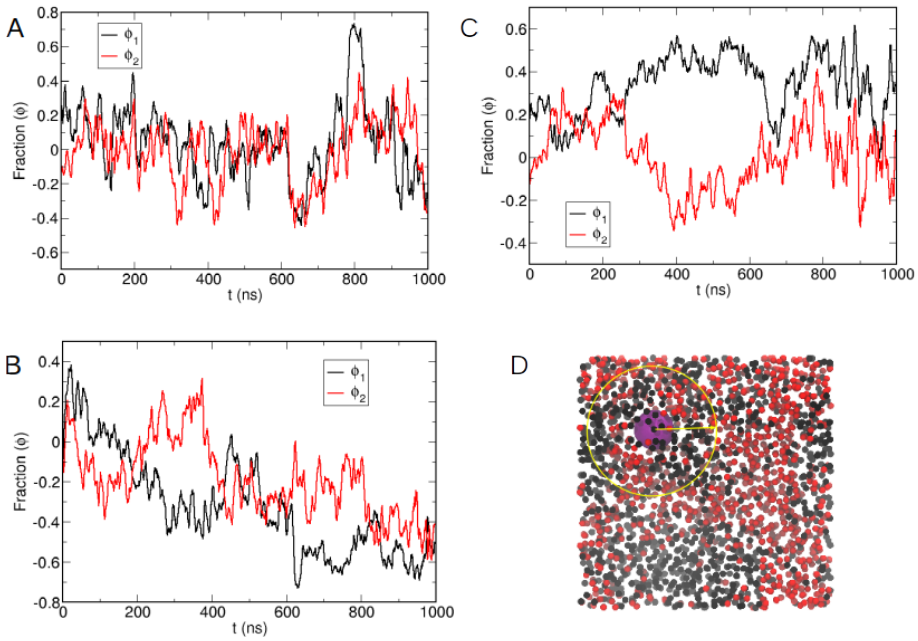

(a)

Fig. 5.24 Measuring the monolayer composition ratios (ϕ_1, ϕ_2) over the trajectory of each NP simulation with the mixed bilayer. (a) shows the illustration of the radius (of 15 Å around the NP surface). (b), (c) and (d) correspond to the monolayer composition change for the R = 1.0, 1.5 and 2.0 nm NPs respectively.

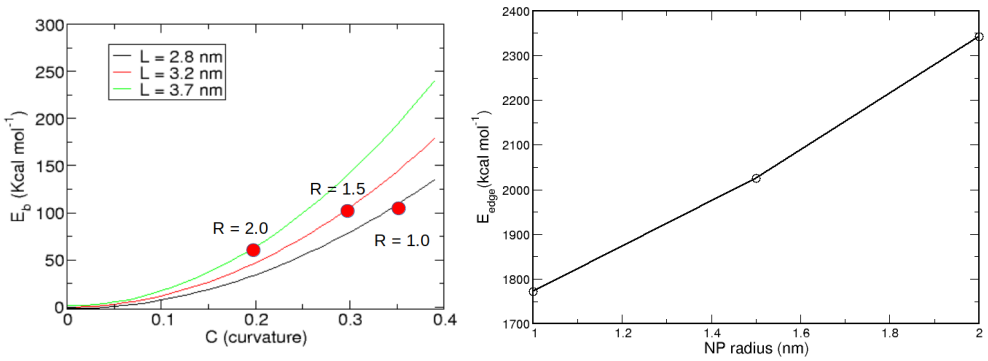

(a) (b)

Fig. 5.25 The approximate bending ($E_{bending}$) and edge energy (E_{edge}) for the bud/cap sizes that correspond to those formed in the the R = 1.0. 1.5 and 2.0 nm NP simulations, shown in (a) and (b) respectively. For the $E_{bending}$, the curvature induced by the NP is annotated as red points on the graph specifically pointing out the curvatures of the NP, while for E_{edge} we show the energetics as a function of the NP radius.

occurrences in nature [181, 182]. Here, the contributing forces in the cap/bud formation are the unfavourable interactions between the $C_{12}E_2$/$C_{12}E_2$-M, the energetic cost of forming the cap/bud, the effect of the NP upon the local arrangement of the surfactants around it, and the extent of interaction between the NP surface and the $C_{12}E_2$/$C_{12}E_2$-M components. Figure 5.25 shows the estimated bending and edge energy, omitting the influence of the NP. We see that the edge energy is significant, measuring at approximately 1772.0 kcal mol^{-1}, 2025 kcal mol^{-1} and 2342 kcal mol^{-1} for the R = 1.0, 1.5 and 2.0 nm cases respectively. The bending contribution to the energetic cost of forming the cap/bud is estimated $E_{bending}$ is estimated near 100, 110 and 50 kcal mol^{-1} for the R = 1.0, 1.5 and 2.0 nm respectively.

Figure 5.15 (a) and (b) shows the $E_{adhesion}$ computation for the single component and multicomponent bilayer respectively. Here, we see a clear difference in the $E_{adhesion}$ between the single component and multicomponent bilayers - the single component bilayer show $E_{adhesion}$ values of -50, -125 and -225 kcal mol^{-1} for the R = 1.0, 1.5 and 2.0 nm NPs respectively, while the multicomponent types gives an estimate of the $E_{adhesion}$ as -0 - -40 kcal mol^{-1}, -50 - -75 kcal mol^{-1}, and -100 - -125 kcal mol^{-1} respectively. Here, the primary distinction we see between the mono and multi-component examples is that the increased interaction with $C_{12}E_2$ bilayer is coupled with a decreased interaction with the $C_{12}E_2$-M components - in each case, the total interaction energy with the NP seems to equal that of the monocomponent examples. This supports our previous analysis in the RDF (Figures 5.10, 5.11, 5.12, for the R = 1.0, 1.5 and 2.0 nm respectively), which suggests the presence of dynamic rearrangements around the NP radius. In each case, we see a negative adhesion energy which favours the wrapping of the NP [177]. As it is apparent from simulation snapshots that each NP is fully wrapped by the surfactant components (hence, x is treated a unity, as it represents the fraction of the NP engulfed in the bilayer, and it has been completely engulfed). From equation 5.5, the adhesion energy per area for each NP can be approximated

as 5.98 kcal mol^{-1} nm^{-2} (10.074 k$_b$T nm^{-2}), 4.42 kcal mol^{-1} nm^{-2} (7.462 k$_b$T nm^{-2}), and 4.476 kcal mol^{-1} nm^{-2} (4.835 k$_b$T nm^{-2}) for the R = 1.0, 1.5 and 2.0 nm NP respectively. We can consider the sum of the $E_{bending}$, $E_{adhesion}$ and E_{edge} as the main components due the bud/micelle formation, therefore, the total energetic contribution to the formation of the cap/bud is given by:

$$E_{total} = E_{bending} + E_{adhesion} + E_{edge} \tag{5.10}$$

From our estimates, we can estimate E_{total} in each case as 50, -25, -175 kcal mol^{-1} for R = 1.0, 1.5 and 2.0 nm examples respectively for the monocomponent cases, where the E_{edge} = 0 as there are no domains. In the case of the mixed bilayer models, we can see that the E_{total} is approximately 1882, 2010 and 2167 kcal mol^{-1} respectively for the R = 1.0, 1.5 and 2.0 nm, where the main source of discrepancy from the monocomponent bilayer comes from the E_{edge} contribution. Yet by these estimates, it would indicate that energetic cost for forming the cap/bud in each of these cases would be too high, primarily due to the energetic penalty from forming the boundary between the domain and the flat membrane i.e. it does not account for the budding phenomena we see, and we would expect that the NPs would remain embedded inside the bilayer. Hence, the remaining factor which would influence the energetics of the membrane budding is the effect of the NP as the lineactant, and the dynamic movement of the surfactants on the the NPs surface. Figure 5.24 shows the time evolution of the monolayer compositions around the NPs - we can see that the fluctuation of composition difference is small in the R = 1.0 nm case, while highly dynamic in the case of R = 1.5 nm. This composition difference is fully stabilized with the R = 2.0 nm example, which also shows the greatest difference in monolayer composition, which would suggest that the presence of larger NPs is correlated with the stabilization of the 'rearranging' state of $C_{12}E_2$ and $C_{12}E_2$-M near the NPs. Figure 5.26 illustrates the mechanism - the distinguishing factor for larger NPs (especially prevalent in R = 2.0 nm example) is that there is a greater surface area for the surfactants to adsorb onto the surface. For the smaller NPs,

steric hindrance between the surfactants and its effect of being a 'smaller' lineactant (i.e. the surface are around the NP of the which the γ is relaxed is smaller) results in the marginal rearrangements around the NP. With larger NPs, the 'rearrangements' of the surfactants as a result of the relaxed line tension in the NP region is present as with the $R = 2.0$ nm example. As the $C_{12}E_2$ and $C_{12}E_2$-M molecules are dynamic near the NP radius, we hypothesize that this has two effects - it would increase the unfavourable interaction energy between the $C_{12}E_2$ and $C_{12}E_2$-M and increase the local curvature around the NP, which would effectively decrease the local bending rigidity, and hence, induce the invagination process.

We are aware that the key weakness of this study is that the mixed bilayer does not represent a single type of bilayer. For example, experimental studies using neutron scatter measurements detected distinctly separate bending moduli in lateral heterogenities [48]. Also, for certain mixed compositions, we observe drastically varying bending moduli in mixed bilayers [183], ranging from 30 (l_d phases) to 100 k_BT (l_o phases) - of an order of magnitude larger than the bending rigidity observed for this study (5.4 k_BT). However, as this study explicitly looks at an extreme case of phase separation, it may be possible to extrapolate this result as the mechanisms behind the fission processes near the boundary domain regions.

The lineactant effect of the hydrophobic NPs has been observed in other studies. Palmieri *et al* [184] showed through ternary composition bilayer simulations that line-active components are observed to accumulate on the binary interface, and acted to decrease the area of interaction between the domain regions, inducing an overall decrease in the rate of phase separation. Similar to that case, following the language of Hassan-Zadeh *et al* [166], we can conclude that the hydrophobic NP acts as a 'loosening' type of lineactant, compared to hybrid lipids which may act to decrease γ by partitioning inside the domain structure. This effect is most likely not confined to NPs - Jefferys *et al* for example, suggested that in the

presence of the membrane-associated G-protein NRas, the rate of domain formation/phase separation in a tertiary bilayer was shown to be dampened [164], which is consistent with its hypothetical effect as a line active component in a mixed bilayer. The slower phase separation observed from the clustering analysis (Figure 5.14) in the presence of the hydrophobic NPs implies a similar effect, which would suggest that in real biological systems, the presence of hydrophobic NPs would directly affect the controlled phase separation mediated by the domain interface membrane proteins. This interface nucleating effect of hydrophobic NPs has been replicated by Cheung [168] using *dissipative particle dynamics* (DPD) simulations, and from this simulation, we see that the nucleation is initially driven the hydrophobic attraction between the NP and each of the lipid/lipid mimic components, and in large numbers, clustering of NPs along the interface has been shown to affect the size of the rafts formed in the DPD simulations. More recently, Risseleda *et al* [185] demonstrated the presence of 'stalkophilic' and 'stalkophobic' regions in the domain boundaries, which act as the insertion points of viral protein structures. The hydrophobic interface provided by the NP here can be compared to the binding motifs on proteins such as the HIV-gp41, which binds specifically to CHOL molecules [186], whilst other proteins have been known to bind to sphingolipids and sphingomyelin components [187, 188].

5.5 Conclusion

By modifying a CG-MD model of a $C_{12}E_2$ surfactant bilayer, we have shown that it is possible to model a two-component bilayer that shows phase separation phenomena on a rapid timescale, which can mimic the domain formation in heterogeneous biomembranes. This allows the rapid formation of a rafts in a bilayer normally attainable only with multiple microsecond timescales. We have illustrated that the hydrophobic NPs of all sizes

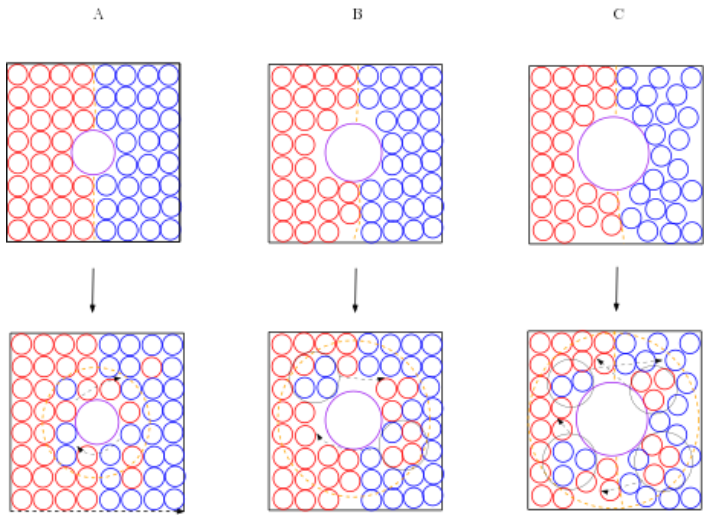

(a)

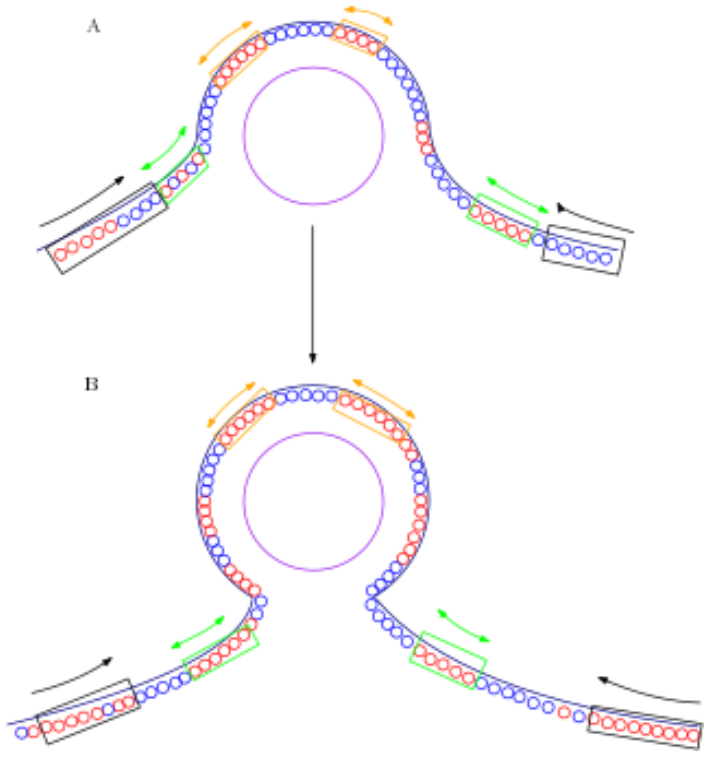

(b)

Fig. 5.26 (a) shows the dynamic composition around the NP budding process - A, B and C show the composition change for the R = 1.0, 1.5 and 2.0 nm respectively, while (b) shows the invagination process with the R = 2.0 NP. the orange and green portions represents the small aggregates that move on the NP surface, driven by the competition between the favourable interaction with the NP surface and the unfavourable interactions with the $C_{12}E_2$/$C_{12}E_2$-M aggregates, while the black portions show the overall interaction of the bulk domain structures towards the NP surface - the invagination process is driven by the increased spontaneous curvature around the green regions due to the combination of these interactions.

locate themslves within the interfaces between the phases. In addition, we show that with larger radius, the NP drives a budding process that may lead to the formations of caps and a full-fledged budding, depending on the NP surface area. We have illustrated a general mechanism involving the interaction between the NPs and the phase boundary which enables a invagination process to a cap to the entire budding of the NP away from the surface. We hypothesize that this is driven by the energetically favourable adsorption onto the surface of the NP, and the simultaneous increase in the spontaneous curvature around the NPs driven by the mismatch of the monolayer compositions around the NP.

Hence, the interplay between the bending energy associated with the membrane curvature around the NP, and the adhesion energy due to favourable hydrophobic interaction is disrupted when placed in a multicomponent bilayer. We hypothesize that with a higher surface area of the NP (i.e. when when the radius become larger), the bud/cap around the NP is stabilised due to a additional coordination with its neighbouring surfactants, and the lesser steric hindrance between the surfactant components when adsorbed on the NP surface. The lineactant hydrophobic NP increases the radius of disorder as the NP radius increases, which materializes as significant composition difference between the monolayers. As seen from estimating the bending and edge energies, these energies do not differ significantly between each NP size, which suggests that the adsorption energy on the NP surface and the increase in the spontaneous curvature around the NP is the primary driver for the cap/budding of the NP. This 'loosening' effect of the domain interface increases the unfavourable interaction between the surfactant components, as shown when comparing to a monocomponent bilayer. This mechanism shows that the membrane line tension may act as a marker for hydrophobic species to conglomerate and as a catalyst for budding events, and requires further investigation.

CHAPTER 6

CONCLUSIONS AND FUTURE WORK

We have managed to conduct a series of nanoparticles (NPs) of hydrophilic, hydrophobic and intemediate properties, using a Hamaker-potential based model. This model consists of a single particle which can be modified to take into account the density of particles that make up the NP, and accurately takes into account surface effects. However, adsorption of the NP onto the surface was not observed, and for larger NPs the energetic cost of bending the bilayer overshadows any gain from surface adsorption, which can be accounted for due to the absence of coulombic interactions in our model. The size effect is also apparent for the hydrophobic and intermediate NP, where we have seen that the larger the size, the greater the rise in free energy when the NP is bending the bilayer (hydrophilic/intermediate) and when exiting (hydrophobic). However, it is clear that the model itself, by simplifying the surface details of the particle, has limitations. Adsorption phenomena typically seen with hydrophilic NPs [84, 142] was not reproduced adequately with the R = 1.5 and 2.0 nm, and even in the R = 1.0 nm it was only hinted at through the PMF.

Analysing the free energy from using Jarsynki's equality (JE) with the steered molecular dynamics (SMD), one can observe that the PMF profiles of the NPs are qualitavely very similar to umbrella sampling (US) results known in literature [62, 84, 189]. However, by

analysing a range of *force* and *velocities*, it can be seen that weighted analysis methods can depict a gross simplification of the model at hand. The main issue with this is that the velocity relaxation time, or the time the solute takes to relax from markovian forces modeling a solvent fails near the bilayer. Adjusting the force means that either the random force term in the Langevin equation is actually controlled by the stiff spring potential being used, which means the work values taken into account with our methods will be prone to errors. The opposite case, where the force is not of a magnitude where it affects the random force term, then the PMF accordingly is dominated by collision frequencies around the bilayers, which does not follow the same trend as the markovian solvent model [190]. This shows that all weighted potential models for mapping the free energy surface breaks down near the bilayer surface. However, Jarsynski's equality based models provide a *moving* solute compared to umbrella sampling, where the reaction coordinate is mapped at a very restricted window. This means that the parts in the reaction coordinate where the Markovian assumption of random force fails can be mapped with some degree of accuracy, and as such, such parts of the PMF can be pointed out and recalibrated to take into account the differing collison frequencies and friction. Qualititavely, the umbrella sampling and JE based methods do not point out any significant qualitiative difference. However, The simulations of the NP-bilayer reaction coordinate has shown that the even just 10 simulations of the bilayer normal reaction coordinate gives a accurate PMF. This is much more convenient method compared to the US methods where the force constants of umbrella 'windows' canbe an order of magnitude higher than that used in SMD simulations [143], which would directly affect the random force term in the langevin equation. Howver, this is only in the situation where the reaction coordinate is as simple as the NP-bilayer normal; any simulations of true *in vivo* environments would be difficult to sample with either methods without a drastic adjustment of the Markovian model.

The overall trend in the PMF graphs of the two-component bilayers seem to suggest that the interaction between the NP and each bilayer component comes with a cost, as seen by the shallower free energy well centered near the tailgroup region. However, there is a tendency for the hydrophobic NP to group near the 'phase interface'. This is suprising, since each component of the bilayer has it's non-bonding potentials as identical as the single-component bilayer of $C_{12}E_2$ used in Chapter 3 and 4. Hence, to consistently observe this free energy effect, it may be a interesting research proposal for to look at the parallel of the bilayer surface as the reaction coordinate for free energy analysis, as this will directly move the NP in the direction of the interface and away from it.

As the Chiu *et al* [132] has shown a greater solvation energy that correponds with with aggregation of hydrophobc particles, it would be interesting for future simulations to study the effects of multiple hydrophobic NPs in a bilayer, where one would expect a competeing effect between the free energy gain from the solvation free energy by aggregation and the hydrophobic tailgroup region. Also, adjusting the Hamaker-potential to take into account other, such as spheroids, rods, and cyclinders may be insightful, as a number of studies have illustraed on the importance of the shape of the NP and the corresponding ease of entry into the bilayer [62, 77].

BIBLIOGRAPHY

[1] J. N. Israelachvili, *Intermolecular and Surface Forces*. Elsevier, 1989.

[2] W. Shinoda and M. L. Klein, "Coarse-Grained molecular modeling of non-ionic surfactant self-assembly," *Soft Matter*, vol. 4, no. 2454-2462, 2008.

[3] B. J. Alder and T. E. Wainwright, "Studies in molecular dynamics. i. general method," *J. Chem. Phys*, vol. 31, 1959.

[4] N. Metropolis, A. W. Rosenbluth, M. N. Rosenbluth, A. H. Teller, and E. Teller, "Equation of state calculations by fast computing machines," *J. Chem. Phys*, vol. 21, no. 1087, 1953.

[5] G. E. Moore, "Cramming more components onto integrated circuits," *Electronics*, vol. 38, no. 8, 1965.

[6] S. Plimpton, "Fast parallel algorithms for short-range molecular dynamics," *J. Comp. Phys*, vol. 117, pp. 1 – 19, 1995.

[7] B. R. Brooks, R. E. Bruccoleri, B. D. Olafson, D. J. States, S. Swaminathan, and M. Karplus, "Charmm: A program for macromolecular energy, minimization, and dynamics calculations," *J. Comp. Chem*, vol. 4, no. 2, pp. 187–217, 1983.

[8] A. D. Mackerell, B. Brooks, C. L. Brooks, L. Nilsson, B. Roux, Y. Won, and M. Karplus, *CHARMM: The Energy Function and Its Parameterization with an Overview of the Program*. Elsevier, 1998.

[9] B. R. Brooks, C. L. Brooks, A. D. Mackerell, L. Nilsson, R. J. Petrella, B. Roux, Y. Won, G. Archontis, C. Bartels, S. Boresch, A. Caflisch, L. Caves, Q. Cui, A. R. Dinner, M. Feig, S. Fischer, J. Gao, M. Hodoscek, W. Im, K. Kuczera, T. Lazardis, J. Ma, V. Ovchinnikov, R. Paci, R. W. Pastor, C. B. Post, J. Z. Pu, M. Schaefer, B. Tidor, R. M. Venable, H. L. Woodcock, X. Hu, W. Yang, D. M. York, and M. Karplus, "Charmm: The biomolecular simulations program," *J. Comp Chem*, vol. 30, no. 10, pp. 1545–1614, 2009.

[10] H. I. Ingolfsson, C. A. Lopez, J. J. Uusitalo, D. J. de Jong, S. M. Gopal, X. Periole, and S. J. Marrink, "The power of coarse-graining in biomoleular simulations," *WIRES Comput Mol Sci*, vol. 4, pp. 225 – 248, 2014.

[11] W. Shinoda, R. DeVane, and M. L. Klein *Journal of Physical Chemistry B*, vol. 114, no. Zwitterionic Lipid Assemblies: Molecular Dynamics Studies of Monolayers, Bilayers, and Vesicles Using a New Coarse Grain Force Field, pp. 6386 – 6849, 2010.

[12] R. Devane, M. L. Klein, C. Chiu, S. O. Nielson, W. Shinoda, and P. B. Moore, "Coarse-Grained Potential Models for Phenyl-Based Molecules: I. Parametization using Experimental Data," *J. Phys. Chem. B*, vol. 296, pp. 6386 – 6393, 2002.

[13] M. Orsi and J. W. Essex, "The ELBA Force Field for Coarse-Grain Modeling of Lipid Membranes," *Plos One*, vol. 6, no. 12, p. e28637, 2011.

[14] M. Orsi, "Comparative assessment of the ELBA coarse-grained model for water," *Molecular Physics*, vol. 112, no. 11, pp. 1566 – 1576, 2014.

[15] S. J. Marrink, H. J. Risselada, S. Yefimov, P. D. Tieleman, and A. H. de Vries, "The MARTINI Force Field: Coarse Grained Model for Biomolecular Simulations," *J. Phys. Chem. B*, vol. 111, no. 27, pp. 7812–7824, 2007.

[16] J. Zhou, I. F. Thorpe, S. Izekov, and G. A. Voth, "Coarse-grained peptide modeling using a systematic multiscale approach," *Biophys. J*, vol. 92, pp. 4289–4303, 2007.

[17] A. Davtyan, N. P. Schaefer, W. Zheng, C. Clementi, and P. G. Papoian, "Awsem-md: protein structure prediction using coarse-grained physical potentials and bioinformatically based local structure biasing," *J. Phys. Chem. B*, vol. 116, pp. 8494–8503, 2012.

[18] M. Jamroz, M. Orozco, A. Kolinski, and S. Kmiecik, "Consistent view of protein fluctuations from all-atom molecular dynamics and coarse-grained dynamics and knowledge-based force-field," *J. Chem. Theory. Comput*, vol. 9, pp. 119–125, 2013.

[19] Y. Chebaro, S. Pasquali, and P. Derreaumaux, "The coarse-grained opep force field for non-amyloid and amyloid proteins," *J. Chem. Theory. Comput*, vol. 116, no. 30, pp. 8741–8752, 2012.

[20] P. Kar, S. M. Gopal, Y. Cheng, A. Predeus, and M. Feig, "Primo: A transferable coarse-grained force field for proteins," *J. Chem. Theory. Comput*, vol. 9, no. 8, pp. 3769–3788, 2013.

[21] N. Basdevant, D. Borgis, and T. Ha-Duong, "A coarse-grained protein-protein potential derived from an all-atom force field," *J. Chem. Phys. B*, vol. 111, no. 8, pp. 9390–9399, 2013.

[22] Y. He, M. A. Mozolewska, P. Krupa, A. K. Sieradzan, T. K. Wirecki, A. Liwo, K. Kaschlishvili, S. Rackosky, D. Jagiela, R. Slusarz, C. R. Czaplewski, S. Oldziej, and H. A. Sheraga, "Lessons from application of the unres force field to predictions of structures of casp10 targets," *Proc. Nat. Acad. Sci*, vol. 110, no. 37, pp. 14936–14941, 2013.

[23] J. K. Marzinek, P. J. Bond, G. Lian, Y. Zhao, L. Han, M. G. Noro, E. N. Pistkopoulos, and A. Mantalaris, "Free energy Predictions of Ligand Binding to a α-Helix using Steered Molecular Dynamics and Umbrella Sampling Simulations," *J. Chem. Inf. Mod*, vol. 54, no. 2, pp. 2093 – 2104, 1997.

[24] J. Kastner and W. Thiel, "Bridging the gap betwen thermodynamic integration and umbrella sampling provides a novel analysis method: "Umbrella integration"," *J. Chem. Phys*, vol. 123, no. 144104, pp. 1 – 5, 2005.

[25] S. Kumar, J. M. Rosenberg, D. Bouzida, R. H. Swendsen, and P. A. Kollman, "The weighted historgram analysis method for free-energy calculations on biomolecules. I. The method," *J. Comput. Chem*, vol. 13, pp. 1011 – 1021, 1992.

[26] R. W. Zwanzig, "High-temperature equation of state by a perturbation method. i. nonpolar gases.," *J. Chem. Phys*, vol. 22, pp. 1420 – 1426, 1976.

[27] A. Laio and M. Parrinello, "Escaping free-energy minima," *Proc Natl Acad Sci U S A*, vol. 99, pp. 12562–12566, 2002.

[28] M. Sousaile and B. Roux, "Extension to the weighted histogram analysis method: Combining umbrella sampling with free energy calculations," *Comput. Phys. Commun*, vol. 135, pp. 40 – 57, 2001.

[29] F. Musiani and A. Giorgetti, "Protein aggregation and molecular crowding: Perspectives from multiscale simulations," *International Review of Cell and Molecular Biology*, vol. 329, pp. 49 – 77, 2017.

[30] S. Park and F. Khalili-Araghi, "Free energy calculation from steered molecular dynamics simulations using jarzynski's equality," *J. Chem. Phys*, vol. 119, no. 6, pp. 3559 – 3566, 2003.

[31] C. Jarzynski, "Nonequilibrium equality for free energy differences," *Phys Rev Lett*, vol. 78, pp. 2690–2693, 1997.

[32] J. S. Patel, A. Berteotti, S. Ronsisvalle, K. Rocchia, and A. Cavalli *J. Chem. Inf. Model*, vol. 54, pp. 470 – 480, 2014.

[33] J. Kumari, R. J. J. Sudan, and C. Sudandiradoss *PLos One*, p. 0183041, 2017.

[34] D. Kosztin, S. Izrailev, and K. Schulten, "Unbinding of retinoic acid from its receptor studied by steered molecular dynamics," *Biophys. J*, vol. 76, no. 188, 1999.

[35] S. J. Marrink, O. Berger, P. Tielemann, and F. Jahnig, "Adhesion forces of lipids in a phospholipid membrane studied by molecular dynamics simulations," *Biophys. J*, vol. 74, p. 931, 1998.

[36] S. Stepaniants, S. Izrailev, and K. Schulten, "Extraction of lipids from phopholipid membranes by steered molecular dynamics," *J. Mol. Model*, vol. 473, no. 3, 1997.

[37] D. A. Christian, A. Tian, W. G. Ellenbroek, I. Levental, K. Rajogopal, P. A. Jamney, A. J. Liu, T. Baumgart, and D. E. Discher, "Spotted vesicles, striped Micelles and Janus assemblies induced by ligand binding," *Nature Materials*, vol. 8, pp. 843–849, 2009.

[38] I. Levental and S. L. Veatch, "The continuing mystery of lipid rafts," *J. Mol. Biol*, vol. 428, no. 2, p. e87369, 2016.

[39] J. H. Lorent and I. Levental, "Structural determinants of protein partitioning into ordered membrane domains and lipid rafts," *Chemistry and Physics of Lipids*, vol. 192, pp. 23 – 32, 2015.

[40] T. Rog and I. Vattulainen, "Structural determinants of protein partitioning into ordered membrane domains and lipid rafts," *Chemistry and Physics of Lipids*, vol. 183, pp. 82 – 104, 2014.

[41] P. F. Almeida, "The many faces of lipid rafts," *Biophysical Journal*, vol. 106, pp. 1841 – 1843, 2014.

[42] P. F. Almeida, "Transbilayer colocalization of lipid domains explained via measurement of strong coupling parameters," *Biophysical Journal*, vol. 109, pp. 2317 – 2327, 2015.

[43] J. B. Helms and C. Zurzolo, "Lipids as targeting signals: Lipid rafts and intracellular trafficking," *Traffic*, vol. 5, pp. 247–254, 2004.

[44] J. H. Ipsen, O. G. Mouritsen, and M. Bloom, "Relationships between lipid membrane area, hydrophobic thickness, and acyl-chain orientational order. the effects of cholesterol," *Biophysical Journal*, vol. 57, no. 3, pp. 405 – 421, 1990.

[45] D. A. Brown and E. London, "Structure and Function of Sphingolipid- and Cholesterol-rich Membrane rafts," *The Journal of Biological Chemistry*, vol. 275, pp. 17221 – 17224, 2000.

[46] K. Simons and E. Ikonen, "Functional rafts in cell membranes," *Nature*, vol. 387, pp. 569 – 572, 1997.

[47] R. G. Anderson and K. A. Jacobson, "Role for lipid shells in targeting proteins to caveolae, rafts, and other lipid domains," *Science*, vol. 296, pp. 1821 – 1825, 2002.

[48] J. D. Nickels, X. Cheng, B. Motofian, C. Stanley, B. Lindner, F. A. Herberle, S. Perticaroli, M. Feygenson, T. Egami, R. F. Standert, J. C. Smith, D. A. A. Myles, M. Ohl, and J. Katsaras, "Mechanical Properties of Nanoscopic Lipid Domains," *ACS Nano*, vol. 8, pp. 2161–2175, 2014.

[49] H. T. McMahon and J. L. Gallop, "Membrane curvature and mechanisms of dynamic cell membrane remodelling," *Nature*, vol. 438, pp. 590–596, 2005.

[50] W. M. Oldham and H. E. Hamm, "Heterotrimeric G protein activation by G-protein-coupled receptors," *Nature Reviews Molecular Cell Biology*, vol. 9, pp. 60 – 71, 2008.

[51] E. H. Kerns, *Drug-like Properties: Concepts, Structure Design and Methods: from ADME to Toxicity Optimization*. Elsevier. Inc, 2008.

[52] X. Xu, R. Li, M. Ma, X. Wang, Y. Wang, and H. Zou, "Multidrug resistance protein P-glycoprotein does not recognize nanoparticle C_{60} experiment and modelling," *Soft Matter*, vol. 8, pp. 2915 – 2923, 2012.

[53] S. A. Pandit, E. Jakobsson, and H. L. Scott, "Simulation of the early stages of nanodomain formation in mixed bilayers of sphingomyelin, cholesterol, and dioleylphosphatidylcholone," *Biophysical Journal*, vol. 87, no. 12562, pp. 3312 – 3322, 2004.

[54] R. S. Cantor *Biophysical Journal*, vol. 76, p. 2625, 1999.

[55] M. F. Brown *Chem. Phys. Lipids*, vol. 73, p. 159, 1994.

[56] S. Scarlata and S. M. Gruner *Biophys. Chem*, vol. 67, p. 269, 1997.

[57] P. Jediovszky and M. Mezel, "Effect of Cholesterol on the Properties of Phospholipid Membranes. 2. Free Energy Profile of Small Molecules," *J. Phys. Chem. B*, vol. 107, no. 22, pp. 5322 – 5332, 2003.

[58] G. V. Meer, D. R. Voelker, and G. W. Feigenson, "Membrane lipids: where they are and how they behave," *Nature Reviews*, vol. 9, pp. 112 – 124, 2008.

[59] A. H. de Vries, A. E. Mark, and S. J. Marrink, "The Binary Mixing Behavior of Phospholipids in a Bilayer: A Molecular Dynamics Study," *Journal of Physical Chemistry B*, vol. 108, pp. 2454 – 2463, 2004.

[60] R. Faller and S. J. Marrink, "Simulation of domain formation in dlpc-dspc mixed bilayers," *Langmuir*, vol. 20, no. 12562, pp. 7686 – 7693, 2004.

[61] E. Sezgin, I. Levental, S. Mayor, and C. Eggeling, "The mystery of membrane organization: composition, regulation and the roles of lipid rafts," *Nature Reviews*, vol. 18, pp. 383 – 392, 2017.

[62] S. L. Fiedler and A. Violi, "Effect of Cholesterol on the Properties of Phospholipid Membranes. 2. Free Energy Profile of Small Molecules," *Biophys. J*, vol. 99, no. 22, pp. 144 – 152, 2010.

[63] R. S. G. D'Rozario, C. L. Wee, E. J. Wallace, and M. S. P. Sansom, "The interaction of C_{60} and its derivatives with a lipid bilayer via molecular dynamics simulations," *Nanotechnology*, vol. 20, no. 22, p. 115102, 2009.

[64] W. Jiang, B. Y. S. Kim, J. T. Rutka, and W. C. W. Chan, "Nanoparticle-mediated cellular response is size-dependent," *Nature Nanotechnology*, vol. 3, pp. 145 – 150, 2008.

[65] B. Wang, J. Yin, I. Kurash, Z. Chai, Y. Zhao, and W. Feng, "Physiochemical origin for free radical generation of iron oxide nanoparticles in biomicroenvironment: Catalytic activities mediated by surface chemical states," *J. Phys. Chem. C*, vol. 117, no. 1, pp. 383 – 392, 2013.

[66] G. Bothum, "Hydrophobic silver nanoparticles trapped in lipid bilayers: Size distribution, bilayer phase behavior, and optical properties," *J. Nanobiotech*, vol. 6, no. 1, p. 4994, 2008.

[67] R. V. Goreham, V. C. Thompson, Y. S. Christopher, T. Gibson, J. G. Shapter, and I. Koper, "Interaction of Silver Nanoparticles with Tethered bilayer Lipid membranes," *Langmuir*, vol. 31, pp. 5868–5874, 2015.

[68] T. Verano-Braga, R. Miethling-Graff, K. Wojidyla, W. Rogowska, and J. R. Brewer, "Insights into the cellular response triggered by silver nanoparticles using quantitive proteonemics," *ACS Nano*, vol. 8, pp. 2161–2175, 2014.

[69] Y. Su, X. Zheng, Y. Chen, M. Li, and K. Liu, "Alteration of intracellular protein expressions as a key mechanism of the deteoriation of bacterial denitrification caused by copper oxide nanoparticles," *Scientific Reports*, vol. 5, p. 15824, 2015.

[70] S. Zhang, H. Gao, and G. Bao, "Physical principles of nanoparticle cellular endocytosis," *Nature Reviews*, vol. 9, no. 9, pp. 8655 – 8671, 2015.

[71] J. A. Swanson, "Coarse-grained molecular dynamics simulations of binary charged lipid membranes: Phase separation and morphological dynamics," *Nat. Rev. Mol. Cell. Biol*, vol. 9, pp. 639 – 649, 2008.

[72] W. H. Lewis *Bull. Johns. Hopkins. Hosp*, vol. 49, pp. 639 – 649, 1931.

[73] S. B. Sieczkarski and G. R. Whittaker, "Influenza virus can enter and infect cells in the absence of clathrin mediated endocytosis," *J. Virol*, vol. 76, no. 10, pp. 10455 – 10464, 2002.

[74] M. Marsh and A. Helenius, "Virus entry: Open sesame," *Cell*, vol. 124, no. 10, pp. 729 – 740, 2006.

[75] K. Yang and Y. Ma, "Computer simulation of the translocation of nanoparticles with different shapes across a lipid bilayer," *Nat. Nanotechnology*, vol. 5, p. 579, 2010.

[76] R. Vacha, F. J. Martinez-Veracochea, and D. Frenkel *Nano. Lett*, vol. 11, no. Receptor-Mediated Endocytosis of Nanoparticles of Various Shapes, pp. 5391 – 5395, 2011.

[77] S. M. Loverde, M. L. Klein, and D. E. Discher, "Nanoparticle shape Improves delivery: Rational Coarse Grain Molecular Dynamics (rCG-MD) of Taxol in Worm-Like PEG-PCL Micelles," *Advanced Materials*, vol. 24, pp. 3823–3830, 2011.

[78] J. P. P. Ramalho, P. Gkeka, and L. Sarkisov, "Structure and Phase Transformations of DPPC Lipid Bilayers in the Presence of Nanoparticles: Insights from Coarse-Grained Mlecular Dynamics Simulations," *Langmuir*, vol. 27, no. 3723-3730, 2011.

[79] S. Pogodin, M. Werner, J. Sommer, and V. A. Baulin, "Nanoparticle-Induced Permeability of Lipid Membranes," *Nano. Lett*, vol. 6, no. 12, pp. 10555 – 10561, 2012.

[80] J. Barnoud, G. Rossi, S. J. Marrink, and L. Monticelli, "Hydrophobic compounds reshape membrane domains," *PLoS Comput Biol*, vol. 10, no. 10, p. e1003873, 2014.

[81] J. Wong-ekkabut, S. Boukina, W. Triampo, I.-M. Tang, D. P. Tieleman, and L. Monticelli, "A simulation study of fullerene translocation through lipid membranes," *Nature Nanotechnology*, vol. 3, no. 7, pp. 363 – 368, 2008.

[82] L. Monticelli, "On atomistic and coarse-grained models for C60 fullerene," *J. Chem. Theory Comput*, vol. 8, no. 7, pp. 1370 – 1378, 2012.

[83] H. Ding and Y. Ma, "Interactions between Janus particles and membranes," *Nanoscale*, vol. 4, pp. 1116–1122, 2012.

[84] Y. Li, X. Chen, and N. Gu, "Computational invetigation of interaction between nanoparticles and membranes: Hydrophobic/hydrophilic effect," *J. Phys. Chem. B*, vol. 15, pp. 16647 – 16653, 2013.

[85] C. Su, H. Merlitz, H. Rabbel, and J. Sommer, "Nanoparticles of various degrees of hydrophobicity interacting with lipid membranes," *J. Phys. Chem. Lett*, vol. 8, no. 10, pp. 4069 – 4076, 2017.

[86] S. Laurent, D. Forge, M. Port, A. Roch, C. Robic, L. V. der Elst, and R. N. Muller, "Magnetic Iron Oxide Nanoparticles: Synthesis, Stabilization, Vectorization, Physiochemical Characterizations, and Biological Applications," *Chem. Rev*, vol. 108, no. 6, pp. 2064 – 2110, 2008.

[87] L. K. Bogart, G. Pourrey, C. J. Murphy, V. Puntes, T. Pellegrino, D. Rosenblum, D. Peer, and R. Levy, "Nanoparticles for Imaging, Sensing, and Therapeutic Intervention," *ACS Nano*, vol. 8, no. 4, pp. 3107 – 3122, 2014.

[88] A. Verma, O. Uzun, Y. Hu, Y. Hu, H. Han, N. Watson, S. Chen, D. J. Irvine, and F. Stellachi, "Surface-structure-regulated cell-membrane penetration by monolayer-protected nanoparticles," *Nature Materials*, vol. 7, pp. 588 – 595, 2008.

[89] A. M. Jackson, P. J. Silva, and F. Stellaci, "From homoligand- to mixed-ligand-monolayer-protected metal nanoparticles: A scanning tunneling microscopy investigation," *J. Am. Chem. Soc*, vol. 128, pp. 11135 – 11149, 2006.

[90] P. K. Ghorai and C. Glotzer, "Molecular dynamics simulation study of self-assembled monolayers of alkanethiol surfactants on spherical gold nanoparticles," *J. Phys. Chem. C*, vol. 111, p. 226106, 2007.

[91] J. Lin, H. Zhang, Z. Chen, and Y. Zhang, "Penetration of Lipid Membranes by Gold Nanoparticles: Insights into Cellular Uptake, Cytotoxicity, and Their Relationship," *Langmuir*, vol. 4, no. 5421-5429, 2010.

[92] Y. Guo, E. Terazzi, R. Seemann, J. B. Fleury, and V. A. Baulin, "Direct proof of spontaneous translocation of lipid-covered hydrophobic nanoparticles through phospholipid bilayer," *Sci. Adv*, vol. 2, no. 10, p. e1600261, 2016.

[93] P. Gkeka, P. Angelikopulos, L. Sarkisov, and Z. Courina, "Membrane paritioning of anionic, ligand-coated nanoparticles is accompanied by ligand snorkeling, local disordering, and cholestrol depletion," *PLoS Comput Biol*, vol. 10, no. 12, p. e1003917, 2014.

[94] R. C. V. Lehn and A. Alexander-Katz, "Fusion of ligand-coated nanoparticles with lipid bilayers: Effect of ligand flexibility," *J. Phys. Chem. A*, vol. 118, no. 12, pp. 5848 – 5856, 2014.

[95] F. Chen, G. Wang, J. I. Griffin, B. Brenneman, N. K. Banda, V. M. Holers, D. S. Backos, L. Wu, S. M. Moghimi, and S. Simberg, "Complement proteins bind to nanoparticle protein corona and undergo dynamic exchange in vivo," *Nature Nanotechnology*, vol. 12, p. 387, 2017.

[96] V. Mirshafiee, R. Kim, M. Mahmoudi, and M. L. Kraft, "Impact of protein precoating on the protein corona composition and nanoparticle cellular uptake," *Biomaterials*, vol. 75, p. 387, 2016.

[97] S. Abbasi, A. Paul, W. Shao, and S. Prakesh, "Cationic Albumin Nanoparticles for Enhanced Drug Delivery to Treat Cancer: Preparation and In Vitro Assessment," *Journal of Drug Delivery*, no. 686108, 2012.

[98] M. Arruebo, M. Valladeres, and A. Gonzalez-Fernandez, "Antibody-Conjugated Nanoparticles for Biomedical Applications," *Journal of Nanomaterials*, no. 439389, 2009.

[99] A. Salvati, A. S. Pitek, M. P. Monopoli, K. Prapainop, F. B. Bombelli, D. R. Hristrov, K. M. Phillip, C. Aberg, E. Mahon, and K. A. Dawson, "Transferrin-functionalized nanoparticles lose their targeting capabilities when a biomolecule corona adsorbs on the surface," *Nature Nanotechnology*, vol. 8, p. 137, 2013.

[100] L. Verlet and D. Levesque, "Molecular-dynamics and time reversibility," *J. Stat. Phys*, vol. 72, pp. 3 – 4, 1993.

[101] W. F. V. Gunsteren and J. C. Berendsen, "A leap-frog algorithm for stochastic dynamics," *J. Stat. Phys*, vol. 3, pp. 173 – 185, 1988.

[102] D. Beeman, "Some multistep methods for use in molecular dynamics calculations," *J. Comp. Phys*, vol. 20, no. 2, pp. 130 – 139, 1976.

[103] P. Ewald, "Die Berechnung optischer und elektrostatischer Gitterpotentiale," *Ann. Phys*, vol. 369, pp. 253 – 287, 2008.

[104] D. Reith and F. P. M. Muller-Pathe, "Deriving effective mesoscale potentials from atomistic simulations," *J. Comput. Chem*, vol. 24, pp. 1624 – 1636, 2003.

[105] W. G. Noid, J. W. Chu, G. S. Ayton, K. Krishna, S. Izekov, G. A. Voth, A. Das, and H. C. Andersen, "A multiscale coarse-graining method i. a rigourous bridge between atomistic and coarse-grained models," *J. Chem. Phys*, vol. 128, p. 244114, 2008.

[106] G. M. Torrie and J. P. Valleau, "Monte Carlo free energy estimates using non-Boltzmann sampling: Application to the sub-critical Lennard-Jones fluid.," *Chem Phys Lett*, vol. 28, pp. 578–581, 1974.

[107] C. Jarzynski, "Equalities and Inequalities: Irreversibility and the Second Law of Thermodynamics at the Nanoscale," *Annu. Rev. Condens. Matter Phys*, vol. 329 – 351, pp. 3575 – 3590, 2011.

[108] S. Park and K. Schulten, "Calculating potentials of mean force from steered molecular dynamics simulations," *J. Chem. Phys*, vol. 120, p. 5946, 2004.

[109] D. Collin, F. Ritort, C. Jarzynski, S. B. Smith, I. T. Jr, and C. Busamante, "Nonequilibrium measurements of free energy differences for microscopically reversible markovian systems," *Nat Lett*, vol. 90, no. 1481, 1998.

[110] T. Bastug, P. Chen, S. M. Patra, and S. Kuyucak, "Potential of mean force calculations of ligand binding to ion channels from jarzynski's equality and umbrella sampling," *J. Chem. Phys*, vol. 128, p. 155104, 2008.

[111] T. Bastug and S. Kuyucak, "Application of jarzynski's equality in simple versus complex systems," *Application of Jarzynski's equality in simple versus complex systems*, vol. 436, pp. 383 – 387, 2007.

[112] S. Plimpton, "Fast parallel algorithms for short-range molecular dynamics," *Journal of Computational Physics*, vol. 117, pp. 1–19, 1995.

[113] M. Orsi and J. W. Essex, "Physical properties of mixed bilayers containing lamellar and nonlamellar lipids: insights from coarse-grain molecular dynamics simulations," *Faraday Discuss*, pp. 249 – 272.

[114] J. Wang, R. M. Wang, J. W. Cadwell, P. A. Kollman, and D. A. Case, "Development and testing of a general AMBER force field," *J. Comput. Chem*, vol. 25, pp. 1157–1174, 2004.

[115] S. Genheden and J. W. Essex *J. Chem. Theory. Comput*, vol. 11, no. 10, pp. 4749 – 4759, 2015.

[116] J. Wang, W. Wang, P. A. Kollman, and D. A. Case, "Automatic atom type and bond type perception in molecular mechanical calculations," *Journal of Molecular Graphics and Modelling*, vol. 25, no. 247260, 2006.

[117] A. Grossfield, "WHAM: the weighted histogram analysis method,"

[118] J. Gore, F. Ritort, and C. Busamante, "Bias and error in estimates of equilibrium free-energy differences from nonequilibrium measurements," *Proc. Nat. Aca. Sci*, vol. 100, no. 22, pp. 12564 – 12569, 2003.

[119] T. V. Pogorelov, J. V. Vermaas, M. J. Arcario, and E. Tajkhorshid, "Partitioning of amino acids into model membrane: Capturing the interface," *The Journal of Physical Chemistry B*, vol. 118, pp. 1481–1492, 2014.

[120] J. L. MacCallum, W. F. D. Bennett, and D. P. Tieleman *Biophys. J*, vol. 94, pp. 3393 – 3404, 2008.

[121] L. Monticelli, S. K. Kandasamy, X. Periole, R. G. Larson, D. P. Tieleman, and S. J. Marrink *J. Chem. Theory. Comput*, vol. 4, pp. 819 – 834, 2008.

[122] A. Warshel, P. K. Sharma, M. Kato, and W. W. Parson, "Bias and error in estimates of equilibrium free-energy differences from nonequilibrium measurements," *Biochimica et Biophysica Acta*, vol. 1764, pp. 1647 – 1676, 2006.

[123] N. Lewinski, V. Colvin, and R. Drezek, "Cytotoxicity of nanoparticles," *Small*, vol. 4, pp. 26 – 49, 2008.

[124] M. M. Bailey, E. M. Gorman, E. J. Munson, and C. J. Berkland, "Pure insulin nanoparticle agglomerates for pulmonary delivery," *Langmuir*, vol. 23, no. 24, pp. 13614 – 13620, 2008.

[125] F. Liu, D. Wu, R. D. Kamm, and K. Chen, "Direct proof of spontaneous translocation of lipid-covered hydrophobic nanoparticles through a phopholipid bilayer," *Biochimica et Biophysica Acta*, vol. 1828, pp. 1667 – 1673, 2013.

[126] E. M. Curtis, A. H. Bahrami, T. R. Weikl, and C. K. Hall, "Modeling nanoparticle wrapping for translocation in bilayer membranes," *Nanoscale*, vol. 7, no. 34, pp. 10799 – 10808, 2015.

[127] S. Bandyopadhyay, M. Tarek, M. L. Lynch, and M. L. Klein, "Molecular Dynamics Study of the Poly(oxyethylene) Surfactant $c_{12}e_2$ and Water," *Langmuir*, vol. 16, pp. 942 – 946, 2000.

[128] W. Shinoda, R. DeVane, and M. L. Klein, "Coarse-grained molecular modeling of non-ionic surfactant self-assembly," *Soft Matter*, vol. 4, pp. 2454–2462, 2008.

[129] D. Alemani, F. Collu, M. Cascalla, and M. D. Peraro, "A Nonradial Coarse-Grained Potential for Proteins Produces Naturally Stable Secondary Structure Elements," *J. Chem. Theory Comput*, vol. 6, no. 1, pp. 315 – 324, 2010.

[130] D. N. LeBard, B. G. Levine, P. Mertmann, S. A. Barr, A. Jusufi, S. Sanders, M. L. Klein, and A. Z. Panagiotopoulos, "Self-assembly of coarse-grained ionic surfactants accelerated by graphics processing units," *Soft Matter*, vol. 8, no. 1, pp. 2385 – 2397, 2012.

[131] W. Shinoda, R. DeVane, and M. L. Klein, "Multi-property fitting and parameterization of a coarse grained model for aqueous surfactants," *Molecular Simulation*, vol. 33, no. 1-2, pp. 27–28, 2007.

[132] C. Chi-Cheng, P. B. Moore, W. Shinoda, and S. O. Nielson, "Size-dependent hydrophobic to hydrophilic transition for nanoparticles: A molecular dynamics study," *The Journal of Chemical Physics*, vol. 131, p. 244706, 2009.

[133] H. C. Hamaker, "The London—van der Waals attraction between spherical particles," *Physica*, vol. 4, no. 10, pp. 1058 – 1072, 1937.

[134] S. Nose, "A unified formulation of the constant temperature molecular dynamics methods," *The Journal of Chemical Physics*, vol. 81, p. 511, 1984.

[135] M. E. Tuckermann, C. J. Mundy, and G. J. Martyna *Journal of Chemical Physics*, vol. 115, p. 1678, 2001.

[136] M. E. Tuckermann, C. H. Mundy, and G. J. Martyna *Europhys . Lett*, vol. 45, p. 149, 1999.

[137] M. Tuckermann, B. J. Berne, and G. J. Martyna, "Reversible multiple time scale molecular dynamics," *J. Chem. Phys*, vol. 97, pp. 1990 – 2001, 1992.

[138] A. B. Krylov, P. Pohl, M. L. Ziedel, and W. G. Hill, "Water permeability of asymmetric lipid bilayers," *J. Gen. Physiol*, vol. 118, no. 4, pp. 333 – 340, 2001.

[139] S. Bandyopadhyay and J. Chanda, "Monolayer of monododecyl diethylene glycol surfactants adsorbed at the air/water interface: A molecular dynamics study," *Langmuir*, vol. 19, no. 10443-10448, 2003.

[140] S. S. Fumari and G. Rapp *J. Phys. Chem. B*, vol. 101, no. 2, pp. 732 – 739, 1997.

[141] S. Bandyopadhyay and J. Chanda, "Molecular dynamics study of surfactant monolayers adsorbed at the oil/water and air/water interfaces," *J. Phys. Chem. B*, vol. 110, no. 10443-10448, 2006.

[142] E. L. da Rocha, G. F. Caramori, and C. R. Rambo, "Nanoparticle translocation through a lipid bilayer tuned by surface chemistry," *Phys. Chem. Chem. Phys*, vol. 15, pp. 2282 – 2290, 2013.

[143] Y. Li and N. Gu, "Thermodynamics of Charged Nanoparticle Adsorption on Charge-Neutral Membranes:A Simulation study," *J. Phys. Chem. B*, vol. 114, no. 8, pp. 2749 – 2754, 2010.

[144] L. Hwankyu and R. G. Larson, "Molecular dynamics simulations of pamam dendrimer-induced pore formation in dppc bilayers with a coarse-grained model," *Journal of Physical Chemistry B*, vol. 110, pp. 18204 – 18211, 2006.

[145] C. Su, H. Merlitz, H. Rabbel, and J. Sommer, "Nanoparticles of various degrees of hydrophobicity interacting with lipid membranes," *Phys. Chem. Lett*, vol. 8, pp. 4069 – 4076, 2017.

[146] L. Yinfeng, L. Xuejin, L. Zhongha, and H. Gao, "Surface-structure-regulated penetration of nanoparticles across a cell membrane," *Nanoscale*, vol. 4, p. 3768, 2012.

[147] H. Zhang, Q. Ji, C. Huang, S. Zhang, B. Yuan, K. Yang, and Y. Ma, "Cooperative transmembrane penetration of nanoparticles," *Scientific reports*, vol. 5, p. 10525, 2015.

[148] P. Gkeka, L. Sarkisov, and P. Angelikopoulos, "Homogenous hydrophobic-hydrophilic surface patterns enhance permeation of nanoparticles through membranes," *J. Phys. Chem. Lett*, vol. 4, pp. 1907 – 1912, 2013.

[149] J. Lin and A. Katz, "Cell membranes open "doors" for cationic nanoparticles/biomolecules: Insights into uptake kinetics," *ACS Nano*, vol. 7, no. 12, pp. 10799 – 10808, 2013.

[150] P. Nativo, I. A. Prior, and M. Brust, "Uptake and intracellular fate of surface modified gold nanoparticles," *ACS Nano*, vol. 2, no. 8, pp. 1639 – 1644, 2008.

[151] T. Baumgart, S. T. Hess, and W. W. Webb *Nature*, vol. 821, p. 821, 2003.

[152] W. Zhou and P. J. Burke, "Versatile bottom-up synthesis of tethered bilayer lipid membranes on nanoelectric biosensor devices," *ACS Appl. Mater. Interfaces*, vol. 9, pp. 14618–14632, 2017.

[153] N. Dimov, E. Kastner, M. Hussain, Y. Perrie, and N. Szita, "Formation and purification of tailored liposomes for drug delivery using a module-based micro continuous-flow system," *Nature Scientific Reports*, vol. 7, no. 12045, 2017.

[154] F. Inci, U. Celik, B. Turken, H. Ozer, and F. Kok, "Construction of p-glycoprotein incorporated tethered lipid bilayer membranes," *Biochemistry and Biophysics Reports*, vol. 2, no. 12045, pp. 115 – 122, 2015.

[155] F. Mazur, M. Bally, B. Stadler, and R. Chandrawati, "Liposomes and lipid bilayers in biosensors," *Advances in Colloid and Interface Science*, vol. 2, 2017.

[156] M. Petaccia, C. Bombelli, F. P. Sterbini, M. Papi, L. Giansanti, F. Bugli, M. Sanguinetti, and G. Mancini, "Liposome-based sensor for the detection of bacteria," *Sensors and Actuators B: Chemical*, vol. 248, pp. 247–256, 2017.

[157] K. Simons and E. Ikonen, "Functional rafts in cell membranes," *Nature*, vol. 387, pp. 569 – 572, 1997.

[158] F. Schmid, "Physical mechanisms of micro- and nanodomain formation in multicomponent lipid membranes," *Biochimica et Biophysica Acta*, 2016.

[159] M. C. Heinrich, L. Levental, P. A. Janmey, and T. Baumgart, "Critical Exponents for Line Tension and Dipole Density Difference from Lipid Monolayer Domain Boundary Fluctuations," *J. Phys. Chem. B*, vol. 112, no. 27, pp. 8063 – 8068, 2008.

[160] R. S. Usery, T. A. Enoki, S. P. Wickramasinghe, M. D. Weiner, W. Tsai, M. B. Kim, S. Wang, T. L. Torng, D. G. Ackerman, F. A. Heberle, J. Katsaras, and G. W. Geigenson, "Line tension controls liquid-disordered + liquid-ordered domain size transition in lipid bilayers," *Biophysical Journal*, vol. 112, pp. 1431 – 1443, 2017.

[161] J. C. Lawrence, D. E. Saslowsky, J. M. Edwardson, and R. M. Henderson, "Real-time analysis of the effects of cholestrol on lipid raft behavior using atomic force microscopy," *Biophys. J*, vol. 84, pp. 1827 – 1832, 2003.

[162] C. B. Yuan, J. Furlong, P. Burgos, and L. J. Johnson, "The size of lipid rafts: an atomic force microscopy study of ganglioside gm1 domains in sphingomyelin/dopc/cholestrol membranes," *Biophys. J*, vol. 82, pp. 2526 – 2535, 2002.

[163] D. Hakobyan and A. Heuer, "Key Molecular Requirements for Raft Formation in Lipid/Cholesterol Membranes," *Plos One*, vol. 9, no. 2, p. e87369, 2014.

[164] E. Jefferys, M. S. P. Sansom, and P. W. Fowler, "NRas slows the rate at which a model lipid bilayer phase separates," *Faraday Discussions*, vol. 169, pp. 209–223, 2014.

[165] C. M. Rosetti, G. G. Montich, and C. Pastorino, "Molecular insight into the line tension of bilayer membranes containing hybrid polyunsaturated lipids," *J. Phys. Chem. B*, vol. 121, no. 4, pp. 1587 – 1600, 2017.

[166] E. Hassan-Zadeh, E. Baykal-Caglar, M. Alwarawrah, and J. Huang, "Complex roles of hybrid lipids in the composition, order and size of lipid membrane domains," *Langmuir*, vol. 30, pp. 1361 – 1369, 2014.

[167] J. Barnoud, G. Rossi, S. J. Marrink, and L. Monticelli, "Hydrophobic Compounds Reshape Membrane Domains," *PLOS Comput Biol*, vol. 10, no. 10, p. e1003873, 2014.

[168] D. Cheung, "Aggregation of nanoparticles on one and two-component bilayer membranes," *The Journal of Chemical Physics*, vol. 141, p. 194908, 2015.

[169] "Hpc midlands plus." http://www.hpc-midlands-plus.ac.uk/.

[170] "Qmul hpc." https://docs.hpc.qmul.ac.uk/.

[171] J. Wolff, S. Komura, and D. Andelman, "Budding of domains in mixed bilayer membranes," *Physical Review E*, vol. 91, p. 012708, 2015.

[172] R. Lipowsky, "Budding of membranes induced by intramembrane domains," *J. Phys. II France*, vol. 91, pp. 1825 – 1840, 1992.

[173] U. Seifert and R. Lipowsky, *Handbook of biological physics*, vol. 1 of *10*. Elsevier, 1995.

[174] S. Seifert and R. Lipowsky, "Adhesion of vesicles," *Phys. Rev. A*, vol. 42, pp. 4768 – 4771, 1990.

[175] W. Helfrich, "Elastic properties of lipid bilayers: theory and possible experiments," vol. 208, pp. 214 – 224, 1973.

[176] E. Kurtisovski, N. Taulier, R. Ober, M. Waks, and W. Urbach, "Molecular origin of model membrane bending rigidity," *Phys. Rev. Lett*, vol. 91, p. 258103, 2007.

[177] W. of nanoparticles by membranes, "Wrapping of nanoparticles by membranes," *Advances in Colloid and Interface Science*, vol. 208, pp. 214 – 224, 2014.

[178] G. Lukat, J. Kruger, and B. Sommer, "APL@Voro: A Voronoi-based Membrane Analysis Tool for Gromacs Trajectories," *J. Chem. Inf. Model*, vol. 5, no. 10525, 2013.

[179] T. Baumgart, S. T. Hess, and W. W. Webb *Nature*, vol. 821, p. 821, 2003.

[180] A. Tian, C. Johnson, W. Wang, and T. Baumgart *Phys. Rev. Lett*, vol. 98, p. 208102, 2007.

[181] H. Yeonjeong, L. E. Katz, and M. Liljestrand, "Distribution of Fullerene Nanoparticles between Water and Solid Supported Lipid Membranes: Thermodynamics and Effects of Membrane Composition on Distribution," *Environmental Science and Technology*, vol. 49, no. 2, p. 14546, 2015.

[182] J. A. Brant, J. Labille, J. Y. Bottero, and M. R. Wiesner, "Characterizing the impact of preparation method on fullerene cluster structure and chemistry," *Langmuir*, vol. 22, no. 8, pp. 3878 – 3885, 2006.

[183] G.Khelashvili, B. Kollmitzer, P. Heftberger, G. Pabst, and D. Harries, "Calculating the bending modulus for multicomponent lipid membranes in different thermodynamic phases," *Journal of Chemical Theory and Computation*, vol. 91, p. 258103, 2007.

[184] B. Palmieri, M. Grant, and S. A. Afran, "Prediction of the dependence of the line tension on the composition of lineactants and the temperature in phase separated membranes," *Phys. Rev. Lett*, vol. 30, pp. 11734 – 11745, 2014.

[185] H. J. Risseleda, "Membrane fusion stalks and lipid rafts: A love-hate relationship," *Biophys. J*, vol. 112, pp. 2475 – 2478, 2017.

[186] R. Schwarzer, I. Levental, A. Gramatica, S. Scolari, V. Buschmann, M. Veit, and A. Herrmann, "The cholestrol-binding motif of the hiv-1 glycoprotein gp41 regulates lateral sorting and oligomerization," *Cell. Microbiol*, vol. 16, no. 10, pp. 1565 – 1581, 2014.

[187] U. Coskun, M. Gryznek, D. Dreshsel, and K. Simons, "Regulation of human egf receptor by lipids," *Proc. Nat. Acad. Sci*, vol. 108, no. 10, pp. 9044 – 9048, 2010.

[188] F. X. Contreras, A. M. Ernst, P. Haberkant, P. Bjorkholm, E. Landahl, B. Gonen, C. Tischer, A. Elofsson, G. von Heijne, C. Thiele, R. Pepperkok, F. Wieland, and B. Brugger, "Molecular recognition of a single sphingolipid species by a protein's transmembrane domain," *Nature*, vol. 481, pp. 525 – 529.

[189] X. B. Lin, Y. Li, and N. Gu, "Nanoparticle's size effect on its translocation across a lipid bilayer: a molecular dynamics simulation," *J. Comput. Theor. Nanosci*, vol. 7, no. 1, pp. 269 – 276, 2010.

[190] Y. M. Ban, R. A. Tasseff, and D. I. Kopelevich, "Non-adiabatic dynamics of interfacial systems: a case study of a nanoparticle penetration into a lipid bilayer," *Molecular Simulation*, vol. 37, pp. 525 – 436, 2011.

APPENDIX A

FORCE FIELD DATA

Potential Parameters

Non-bonded interaction parameters (Table A.1) and parameters for bond stretching (Table A.2) and angle bending (Table A.3) are taken (without modification) from Shinoda *et al* [127].

Table A.1 Nonbonded interaction parameters

Bead 1	Bead 2	Function	ε (kcal/mol)	σ (Å)
W	W	LJ12-4	0.8950	4.3710
W	OA	LJ12-4	0.7000	3.9500
W	EO	LJ12-4	0.5700	4.3100
W	CM	LJ12-4	0.3400	4.4385
W	CT2	LJ12-4	0.2900	4.2960
OA	OA	LJ9-6	0.4491	3.7130
OA	EO	LJ9-6	0.4400	3.8900
OA	CM	LJ9-6	0.3650	3.9870
OA	CT2	LJ9-6	0.3800	3.8400
EO	EO	LJ9-6	0.4050	4.2500
EO	CM	LJ9-6	0.3770	4.2740
EO	CT2	LJ12-4	0.3700	4.1400
CM	CM	LJ12-4	0.4200	4.5060
CM	CT2	LJ9-6	0.3620	4.3635
CT2	CT2	LJ9-6	0.3120	4.2210

Table A.2 Bond parameters where k_l is the bond stretching force constant and l_0 is the equilibrium bond length.

Bead 1	Bead 2	k_l (kcal/mol/Å^2)	l_0 (Å)
OA	EO	15.000	2.79
EO	EO	4.900	3.28
EO	CM	7.100	3.56
CM	CM	6.160	3.64
CM	CT2	9.000	3.13

Table A.3 Angle parameters where k_θ is the angle bending force constant and θ_0 is the equilibrium angle.

Bead 1	Bead 2	Bead 3	k_θ (kcal/mol/rad^2)	θ_0 (degree)
OA	EO	EO	3.000	131.0
EO	EO	CM	3.200	146.0
EO	CM	CM	3.200	146.0
CM	CM	CM	1.190	173.0
CM	CM	CT2	1.600	172.0

Derivation of Nanoparticle-Solvent Interaction Potentials

To derive the nanoparticle-solvent interaction potentials (and forces) it is useful to consider the nanoparticles as continuum, spherical solids (by analogy to the work of Hamaker [133]). The interaction may be written as

$$\begin{aligned} U(r) &= U_{rep}(r) + U_{att} \\ &= C_{rep} r^{-n} + C_{att} r^{-m} \end{aligned} \tag{A.1}$$

To determine the interaction between a CG bead and the nanoparticle we may then integrate this over the interior volume of the nanoparticle

$$U(r) = \int_V dr' \rho u(r) = \int_V dr' \rho (u_{rep}(r) + u_{att}(r)) \tag{A.2}$$

where ρ is the density of atoms in the NP. Separating this into repulsive and attractive contributions gives

$$U_{rep}(r,R) = \int_V dr' \rho u_{rep}(r) = \int_V dr \rho C_{rep} \left| r - r' \right|^{-n} \tag{A.3}$$

$$U_{att}(r,R) = \int_V dr' \rho u_{att}(r) = -\int_V dr \rho C_{att} \left| r - r' \right|^{-m} \tag{A.4}$$

so this reduces to the calculation of integrals of the form

$$\int_V dr' \left| r - r' \right|^{-N} \tag{A.5}$$

With no loss of generality we can place the centre of the nanoparticle at $R = (0,0,0)$ and the solvent particle at $r = (0,0,r)$. Using spherical coordinates the position of a volume

element in the particle may be written as $r' = (a\sin\theta\cos\phi, a\sin\theta\sin\phi, a\cos\theta)$ and

$$\begin{aligned}\left|r-r'\right| &= \sqrt{a^2\sin^2\theta\cos^2\phi + a^2\sin^2\theta\sin^2\phi + (r-a\cos\theta)^2} \\ &= \sqrt{a^2+r^2-2ar\cos\theta} \end{aligned} \tag{A.6}$$

Equation A.5 then becomes

$$\int_V dr' \left|r-r'\right|^{-N} = \int_0^R daa^2 \int_0^\pi d\theta\sin\theta \int_0^{2\pi} d\phi \left|r-r'\right|^{-N} \tag{A.7}$$

$$= 2\pi \int_0^R daa^2 \int_0^\pi d\theta\sin\theta \left[a^2+r^2-2ar\cos\theta\right]^{-N/2} \tag{A.8}$$

which may be evaluated analytically. For the specific interaction potentials (Eqns A.1) we need to evaluate eqn. A.8 with N =4, 6, 9, and 12, which are:

$N = 4$

$$2\pi \int_0^R daa^2 \int_0^\pi d\theta\sin\theta \left[a^2+r^2-2ar\right]^{-2} = 2\pi \left[\frac{R}{r^2-R^2} + \frac{1}{2r}\ln\left(\frac{r-R}{r+R}\right)\right] \tag{A.9}$$

$N = 6$

$$2\pi \int_0^R daa^2 \int_0^\pi d\theta\sin\theta \left[a^2+r^2-2ar\right]^{-3} = \frac{4\pi}{3}\frac{R^3}{(r^2-R^2)^3} \tag{A.10}$$

$N = 9$

$$2\pi \int_0^R daa^2 \int_0^\pi d\theta\sin\theta \left[a^2+r^2-2ar\right]^{-9/2} = \frac{4\pi}{105}\frac{R^3(3R^4+42R^2r^2+35r^4)}{r(r^2-R^2)^6} \tag{A.11}$$

$N = 12$

$$2\pi \int_0^R daa^2 \int_0^\pi d\theta\sin\theta \left[a^2+r^2-2ar\right]^{-6} = \frac{4\pi}{45}\frac{R^3(5R^6+45R^4r^2+63R^2r^4+15r^6)}{(r+R)^9(r-R)^9} \tag{A.12}$$

The integrated 12-4 potential is then given by

$$\begin{aligned} U_{NP}^{12-4}(r,R) &= \int_V dr\rho \frac{3\sqrt{3}\varepsilon}{2}\left[\left(\frac{\sigma}{r}\right)^{12} - \left(\frac{\sigma}{r}\right)^{4}\right] \\ &= \frac{3\sqrt{3}\rho\varepsilon\sigma^{12}}{2}\int_V dr\frac{1}{r^{12}} - \frac{3\sqrt{3}\rho\varepsilon\sigma^{4}}{2}\int_V dr\frac{1}{r^{4}} \\ &= \frac{2\sqrt{3}\pi\rho\varepsilon\sigma^{12}R^3}{15}\frac{5R^6+45R^4r^2+63R^2r^4+15r^6}{(r^2-R^2)^9} \\ &- \frac{3\pi\rho\varepsilon\sigma^4 R}{r^2-R^2} + \frac{3\sqrt{3}\pi\rho\varepsilon\sigma^4}{2r}\ln\left[\frac{r-R}{r+R}\right] \end{aligned} \tag{A.13}$$

while the intgrated 9-6 potential is

$$\begin{aligned} U_{NP}^{9-6}(r,R) &= \int_V dr\rho \frac{27\varepsilon}{4}\left[\left(\frac{\sigma}{r}\right)^{9} - \left(\frac{\sigma}{r}\right)^{6}\right] \\ &= \frac{27\rho\varepsilon\sigma^{9}}{4}\int_V dr\frac{1}{r^{9}} - \frac{27\rho\varepsilon\sigma^{6}}{4}\int_V dr\frac{1}{r^{6}} \\ &= \frac{9\pi\rho\varepsilon\sigma^9}{35}\frac{R^3(3R^4+42R^2r^2+35r^4)}{r(r^2-R^2)^6} - \frac{9\pi\rho\varepsilon\sigma^6R^3}{(r^2-R^2)^3} \end{aligned} \tag{A.14}$$

Nanoparticle Interaction Potentials

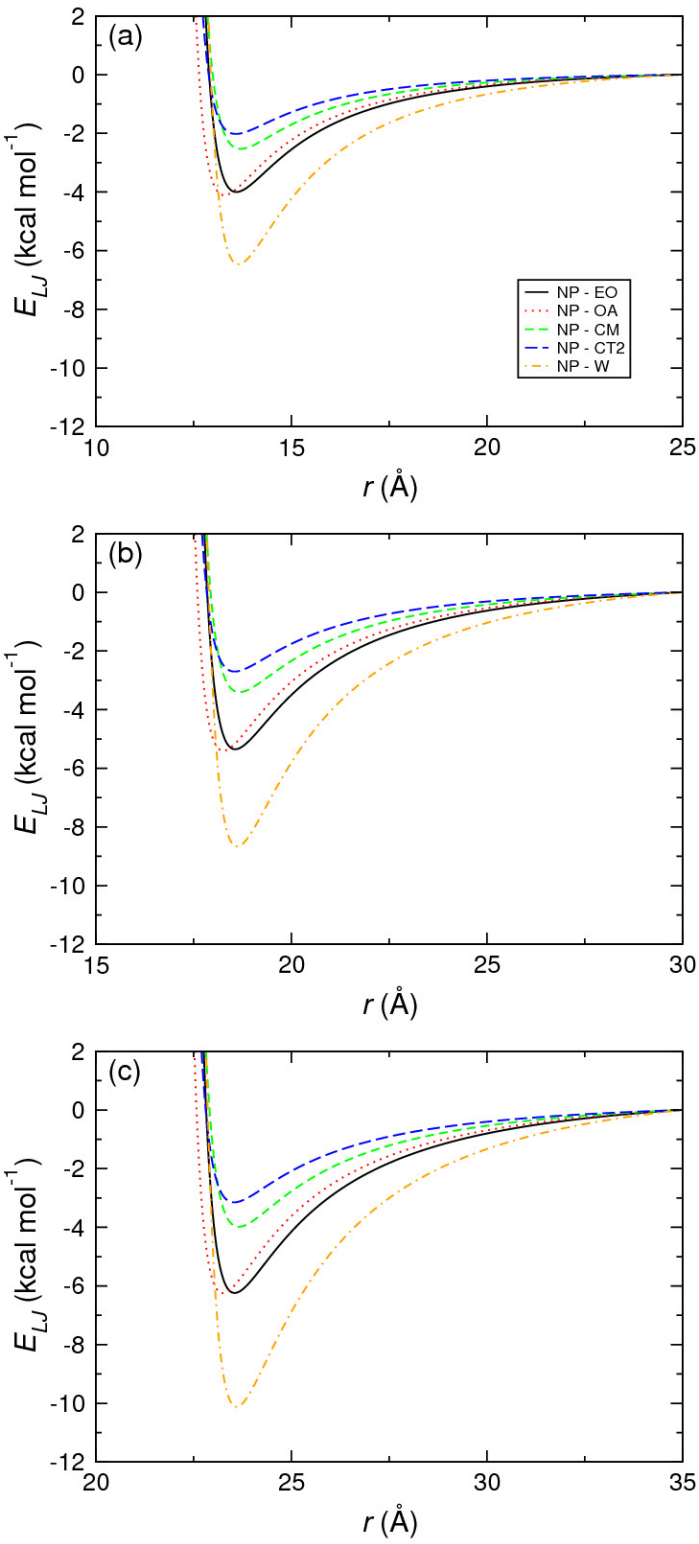

Fig. A.1 Interaction potentials of the CG polymer beads with the (a) 1.0, (b) 1.5, and (c) 2.0 nm hydrophilic nanoparticle.

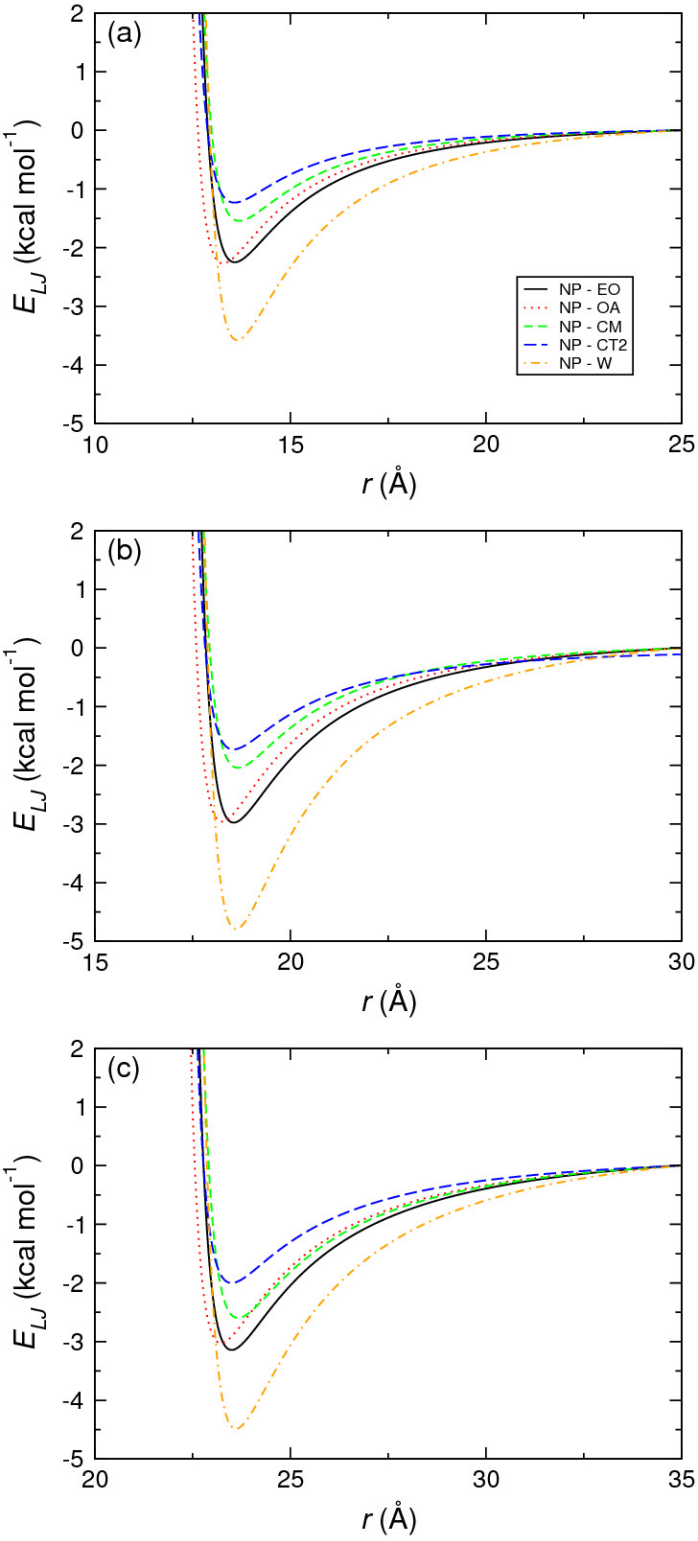

Fig. A.2 Interaction potentials of the CG polymer beads with the (a) 1.0, (b) 1.5, and (c) 2.0 nm intermediate nanoparticle.

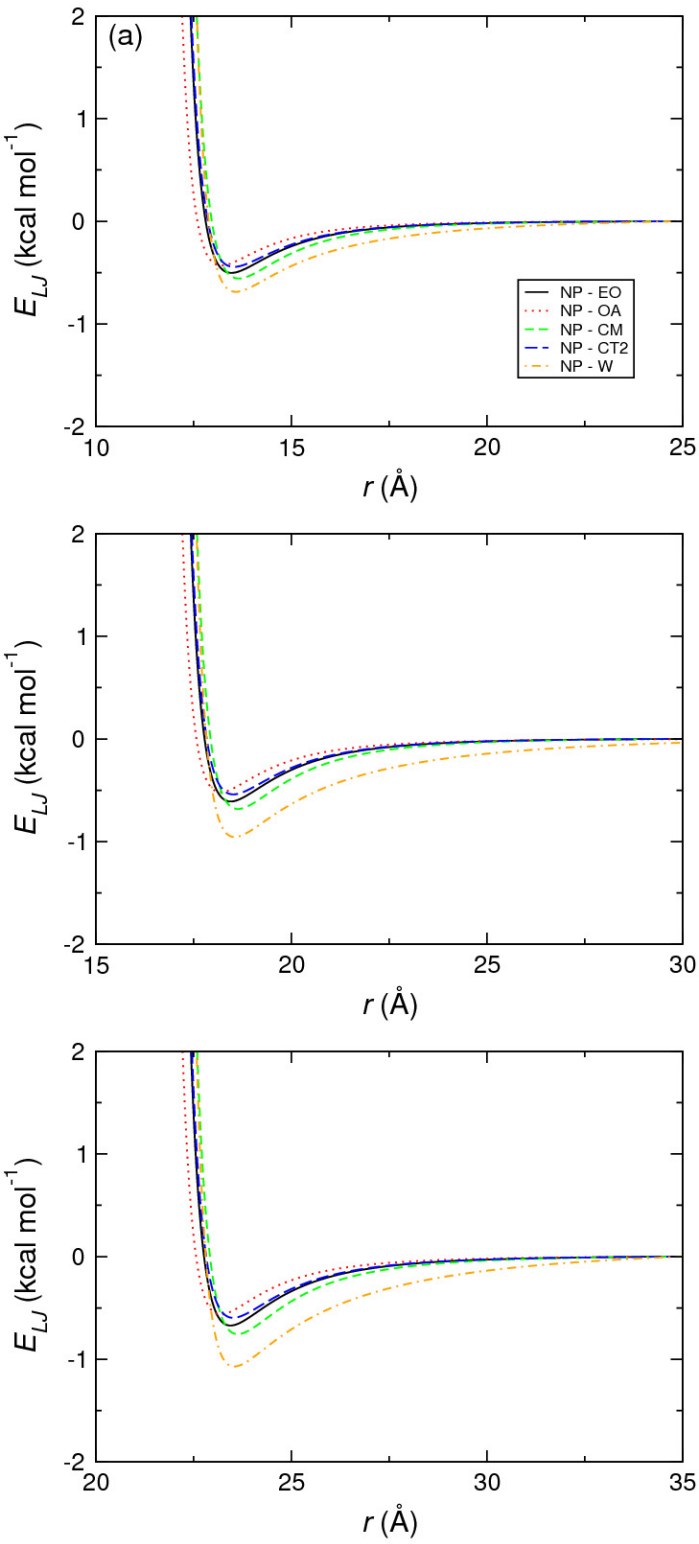

Fig. A.3 Interaction potentials of the CG polymer beads with the (a) 1.0, (b) 1.5, and (c) 2.0 nm hydrophobic nanoparticle.

APPENDIX B

MIXED BILAYER SYSTEMS

Potential Parameters for Systems 1-3

Non-bonded interaction parameters (Tables B.1 - B.3 (for systems 1-3)). The NP-bilayer interaction for the $C_{12}E_2$ is identical to the $R = 1.0$ nm size hydrophilic/hydrophobic NP. Here, we show the additional tabulated non-bonding parameters used for $C_{12}E_2$-M in the 1:1 mixed bilayer. The $C_{12}E_2$-M beads non-bonding potentials with other M beads are equivalent to the $C_{12}E_2$ case.

Table B.1 Nonbonded interaction parameters - System 1

Bead		Function	ε (kcal/mol)	σ (Å)
OA-M	OA	LJ9-6	0.375	3.7130
OA-M	EO	LJ9-6	0.4100	3.8900
EO-M	OA	LJ9-6	0.4150	4.2500
EO-M	EO	LJ9-6	0.4190	4.2740
CM-M	CM	LJ9-4	0.3300	4.5060
CM-M	CT2	LJ9-6	0.3620	4.3635
CT2-M	CM	LJ9-6	0.3320	4.2210
CT2-M	CT2	LJ9-6	0.2820	4.2210

Table B.2 Nonbonded interaction parameters - System 2

Bead		Function	ε (kcal/mol)	σ (Å)
OA-M	OA	LJ9-6	0.4001	3.7130
OA-M	EO	LJ9-6	0.4090	3.8900
EO-M	OA	LJ9-6	0.3650	4.2500
EO-M	EO	LJ9-6	0.4200	4.2740
CM-M	CM	LJ9-4	0.4200	4.5060
CM-M	CT2	LJ9-6	0.3650	4.3635
CT2-M	CM	LJ9-6	0.3220	4.2210
CT2-M	CT2	LJ9-6	0.272	4.2210

Table B.3 Nonbonded interaction parameters - System 3

Bead		Function	ε (kcal/mol)	σ (Å)
OA-M	OA	LJ9-6	0.4491	3.7130
OA-M	EO	LJ9-6	0.4400	3.8900
EO-M	OA	LJ9-6	0.4050	4.2500
EO-M	EO	LJ9-6	0.3770	4.2740
CM-M	CM	LJ9-4	0.4200	4.5060
CM-M	CT2	LJ9-6	0.3620	4.3635
CT2-M	CM	LJ9-6	0.3120	4.2210
CT2-M	CT2	LJ9-6	0.3120	4.2210